NASA Technical Paper 1143

# Configuration Heating for a Hypersonic Research Airplane Concept Having a 70° Swept Double-Delta Wing

Pierce L. Lawing

MAY 1978

NASA

# Configuration Heating for a Hypersonic Research Airplane Concept Having a 70° Swept Double-Delta Wing

Pierce L. Lawing
Langley Research Center
Hampton, Virginia

NASA

# SUMMARY

There have been a number of configurations proposed for a hypersonic research airplane. The configuration examined in this report is the initial one to have extensive wind-tunnel testing, including the present heat-transfer investigation. The format of this paper has been arranged to present the data so that it may be examined casually, on a qualitative basis, as well as more rigorously on a quantitative basis.

The data include heat transfer on a conical fuselage, double-delta wing, tip-fin effects, deflected elevons, lee-side phenomena, and Reynolds number changes sufficient to indicate the type of boundary layers to be expected. An analysis section also allows comparison of portions of the data with accepted theories. Configuration heat-transfer data not available herein include canopy heating and its effects, effect of ratio of adiabatic temperature to wall temperature, roughness, yaw, protuberances, leading-edge bluntness, engine case or engine flow interaction, and negative angle of attack.

# INTRODUCTION

Since the termination of the X-15 program, there has been an effort underway at Langley Research Center to define a new research airplane. This effort has resulted in a number of different configurations as the program has been modified in response to new knowledge and/or responded to constraints such as launch vehicle, acceleration mode, and cost. Some of the resulting configurations, including the one investigated in this report, are discussed in reference 1.

When the physical constraints on a vehicle have been satisfied, and the configuration has been exercised analytically for acceptable aerodynamic performance, wind-tunnel testing is undertaken to define aerodynamic characteristics across the speed range and to investigate hypersonic heat-transfer characteristics. The aerodynamic characteristics of this configuration are given in references 2 and 3 for low speeds and in reference 4 for hypersonic speeds. Information on propulsion integration aspects is contained in references 5 and 6 and descent analysis and associated heat loads over the speed range are presented in reference 7. The present report presents experimental heat-transfer data and analysis for this configuration at Mach 6.

The heating data were obtained by use of the phase-change-paint technique described in reference 8. The model was tested over an angle-of-attack range from $0°$ to $24°$ and model length Reynolds numbers from $4 \times 10^6$ to $15 \times 10^6$. All tests were conducted in the Langley 20-inch Mach 6 tunnel.

# SYMBOLS

When more than one symbol for a concept is given, the second symbol is the computer program symbol.

$C_p$      pressure coefficient, $(p - p_\infty)/q_\infty$

$c_r$      reference chord length, 29.55 cm (see fig. 2(b))

$D$      maximum fuselage diameter, 6.83 cm

$h,H$      heat-transfer coefficient

$\bar{h}$      area-averaged heat-transfer coefficient

$h_s,HS$      reference heat-transfer coefficient (stagnation condition on a scaled 30.48-cm radius sphere)

$l$      model length, 50.8 cm

$M$      Mach number

$N$      coordinate normal to wing leading edge

$p$      pressure

$q$      dynamic pressure

$R_l$      Reynolds number based on free-stream conditions and model length

$R_w$      Reynolds number based on local conditions and local fuselage width

$R_x$      Reynolds number based on local conditions and distance from leading edge or virtual origin

$S$      surface coordinate normal to model top center line

$T_o,TO$      total temperature

$T_{aw},TAW$      adiabatic wall temperature

$T_{pc}$      phase-change-paint melt temperature

$x$      axial coordinate referenced to model nose

$\alpha$      angle of attack

$\delta$      surface inclination angle (see fig. 2(b))

$\delta_e$      elevon deflection angle

Subscripts:

aw       adiabatic

∞        free-stream conditions


## MODELS AND TEST FACILITY

### Models

A photograph of the configuration tested is shown with the scramjet engine attached in figure 1. It has a high volume fuselage to contain the low-density liquid hydrogen fuel and the fuselage forebody is shaped to provide a uniformly compressed flow to the research scramjet. The expansion surface behind the engine serves as the engine exhaust nozzle. Elevons provide pitch control whereas the tip fins provide directional stability and yaw control. The three-view drawing and selected cross sections in figure 2(a) show the scramjet location, flat bottom wing, and other configuration details. The engine was not included on the models used in this test. Note the increased incidence of the strake, or forward delta, as compared with the main wing. (See fig. 2(b).)

The 0.021-scale test models were cast by using a mold patterned directly from a stainless-steel force model described in reference 2. The material used to cast the models was a high-temperature epoxy plastic which has a low thermal diffusivity, good homogeneity, and good resistance to thermal shock. A sample block of the material was cast simultaneously with each model and thermal conductivity; heat capacity and density were determined by standard laboratory methods over the expected operating temperature range. To provide additional strength, the model was cast with integral steel sting, and a silicone rubber buffer was included between the sting and the plastic model for isolation from thermal stress.

Since the models have a limited testing life because of thermal cycling, four models were cast from the mold in order to provide spares. To fully utilize these models, some were fitted with elevons, deflected into the flow on the wing top and bottom as shown in figure 2(b). Also, one model was fitted with a center vertical tail in addition to the tip fins, but was used only for oil-flow tests.


### Test Facility

The test program was conducted in the Langley 20-inch Mach 6 tunnel which is of the blowdown type and exhausts to a vacuum sphere through a variable-area second minimum. The test section has a square cross section and the test air is delivered by a two-dimensional contoured nozzle block. A vacuum-tight chamber under the test section houses a hydraulically operated model injection system which allows the model to be injected into the test chamber after stable operating conditions are obtained. Windows on each side and the top permit simultaneous motion-picture photography of the model top (or bottom if rolled

180°) and side during a run.  A more detailed description of the tunnel can be found in reference 7.

## TEST CONDITIONS AND DATA REDUCTION

Phase-change-paint heat-transfer data and a limited number of oil-flow patterns were obtained in these tests.  All data were taken in the Langley 20-inch Mach 6 tunnel on the models previously described.  Nominal test conditions were Mach 6, 533 K stagnation temperature, and Reynolds number of $14 \times 10^6$ based on model length.  Reynolds number was as low as $4 \times 10^6$ for a few tests and represented a range in total pressure from 35 to 11 atmospheres. (1 atmosphere = 101.3 kPa.)  Angle-of-attack range was from 0° to 24°.

### Heat Transfer

The phase-change-paint method (refs. 8 and 9) employs a series of paints which melt at a known temperature.  They are opaque when unmelted and become transparent when melted.  Typically, white paint is sprayed in a thin coat on a black model.  When the model is injected into the test airstream, the paint on the high heating areas melts first and allows the black model to show through.  These areas then enlarge as the paint melts and the later melt time indicates successively lower heating rates.  Knowledge of the time at which the melt occurs, the paint melt temperature, and the density, specific heat, and thermal conductivity of the model provides sufficient information to determine the heat-transfer coefficient.  The melt time is measured from the time of model injection.  This is a straightforward procedure utilizing the transient one-dimensional heat conduction equation for a semi-infinite slab.  Further details of this method and a discussion of the necessary assumptions are presented in reference 8.

Figure 3 is a sequence of photographs taken from motion pictures of the model lee side showing a typical melt pattern as it progresses with time.  In the first photograph, only the paint at the leading edge, tip fin-wing junction, and the strake-wing juncture have melted.  The area of melted paint in these regions has increased in the second photograph and details of the strake interference heating on the wing top are visible in the third photograph.  The fourth photograph gives the first indication of lee-side fuselage heating, and the fifth photograph clearly indicates the top of the wing area influenced by tip fins.  The final photograph shows areas where the paint has not melted and indicates low heating rates.  Data reduction is accomplished by drawing each of the five contours superimposed on the model outline drawing.  The heat-transfer coefficient for each contour is calculated and the results are nondimensionalized by the theoretical laminar stagnation-point heat-transfer coefficient to a 30.8-cm-radius hemisphere scaled the same as the model (0.021-scale).  A table on each of the contour-line drawings in the following figures presents contour-line number, nondimensional heat-transfer coefficient, and ratio of adiabatic wall to total temperature $T_{aw}/T_o$.  Turbulent values of $T_{aw}/T_o$ were used in reducing the data and were calculated, based on local conditions, by using the cube root of the Prandtl number for the recovery factor.  Variation of the

Prandtl number with local temperature was considered, and a typical turbulent value was assumed for the model lee side.

## Oil-Flow Patterns

Oil-flow data were obtained by spraying random patterns of white oil droplets on flat black models. The white oil was made by mixing oleic acid, silicone oil, and titanium dioxide. The model was injected into the tunnel airstream after flow stabilization and the flow of oil was observed by means of closed-circuit television. When the desired amount of oil flow was observed, the model was withdrawn from the airstream and subsequently removed from the injection box and photographed.

## DISCUSSION OF RESULTS

### Model Lee Side

Figure 4(a) shows the heat-transfer coefficient contours on the model top at $\alpha = 6.2^{o}$ and $R_l = 15 \times 10^6$. A metal-tipped nose precludes obtaining heating data in the nose region $\left(0 < \dfrac{x}{l} < 0.2\right)$. Highest heating is indicated by the number 1 contour and occurs at the wing and strake leading edges, wing-body juncture, and just inboard of the tip fins. Increased heating due to impinging flow from the strake may be seen at the wing-strake juncture. The fuselage top has relatively low heating rates. An increase in $\alpha$ to $11.9^{o}$ (fig. 4(b)) indicates maximum heating still at the wing and strake leading edges but no longer at the wing-fuselage juncture or inboard of the tip fins. A region of high heating has developed on the fuselage just above the strake on the left side. Increases in heating are still evident at the wing-strake juncture and inboard of the tip fins. The fuselage top pattern has become complicated with streaks representing the heating from the flow expansion, separation, and associated vortices.

Lee-side oil flows at $R_l = 15 \times 10^6$ are shown in figure 5 for angles of attack of $6.2^{o}$ and $11.9^{o}$. The model used for $\alpha = 6.2^{o}$ has deflected elevons and a center vertical tail in addition to the tip fins. In figure 5(a) at $\alpha = 11.9^{o}$, the flow is attached on the forebody for about one-third the fuselage length where it separates and forms lee-side vortices. There is also separation on the inboard portion of the wing, but the flow remains attached near the fuselage and corresponds to the high heating region as discussed for figure 4(a). As the angle of attack is increased (fig. 5(b)), separation occurs earlier on both the fuselage and the wing. The entire inboard section of the wing, including the region near the fuselage, is now separated and corresponds to the low heating region of the wing (fig. 4(b)). Note that this model has deflected elevons but no vertical tail.

Figure 6 presents results at a lower length Reynolds number of $R_l = 4 \times 10^6$. Data at $\alpha = 0.6^{o}$ are shown in figure 6(a) and show the regions of highest heating to occur on the wing leading edges and inboard of

the tip fin. Influence of the strake flow is again seen on the wing near the wing-strake juncture. The heating pattern changes from simple on the forward portion of the fuselage to more complex on the aft portion. An increase in $\alpha$ from 0.6° to 11.9° (fig. 6(b)) brings marked changes in patterns; the leading edges of both fin and strake have high heating but lack influence on the wing heating from the strake flow and lack definition of effects inboard of the tip fins. A complex heating pattern now extends the full length of the fuselage.

A further increase in $\alpha$ to 24° (fig. 6(c)) shows maximum heating still on the wing and strake leading edges and also extending into the region inboard of the tip fins. In addition, high heating streaks have developed at the fuselage-strake juncture. The fuselage top heating is very low when compared with the levels of the $\alpha$ = 11.9° case (fig. 6(b)).

Figure 7 presents data at $\alpha$ = 11.9° and at five values of Reynolds numbers from $4.7 \times 10^6$ to $15.6 \times 10^6$, based on model length. At the lower value of Reynolds number (fig. 7(a)) the discernible heating effects, other than those expected from simple well-developed boundary layers, are the leeward center-line vortex heating and the strake interference heating at the wing-fuselage juncture. As the Reynolds number increases (fig. 7(b)), the center-line vortex heating pattern becomes broken and more complicated, the fuselage-wing juncture heating extends further to the rear, and the effect of the strake flow is seen at the strake-wing juncture and on a previously undisturbed part of the wing, shown by the closed contour loop number 4. This model had deflected elevons and the strake flow is possibly responsible for the number 3 contour region near the inboard end of the 12° deflected elevon. Note the region of high heating (contour no. 1) on the 12° elevon due to tip-fin interference. Also, there is no apparent elevon hinge-line separation phenomena.

As the Reynolds number is further increased (fig. 7(c)), an additional region of high heating appears on the fuselage midway between the center line and the wing juncture. The distortion in wing heating contours is more evident at the strake-wing junction and the strake flow impingement on the 12° elevon is more extensive. Figure 7(d) presents data at the next higher step in Reynolds number. The results are much the same as those of figure 6(c) except the midwing interference heating, present in figures 7(b) and 7(c), is no longer evident, although the impingement effect is still present on the 12° deflected elevon. The highest Reynolds number tested is shown in figure 7(e) and it also lacks the midwing interference heating. Note that the heating on the fuselage side and fuselage-wing juncture in particular has increased in complexity, extent, and severity (when compared with the leading-edge heating) as the Reynolds number has increased through these five steps. The complexity of these patterns makes a more detailed or qualitative discussion impractical, but the data are compared for one fuselage station in "Analysis of Results."

## Model Windward Side

Figure 8 shows heat-transfer contours at a nominal model length Reynolds number of $15 \times 10^6$ and five values of angle of attack. Data at $\alpha$ = 0.6° are shown in figure 8(a). The most severe heating occurs on the wing and strake leading edges. Interference heating from the tip fin produces patterns on the

wing bottom that are similar to those on the wing top at this angle of attack. The feature that is different from the model top and dominates the windward-side patterns is the forebody and wing transition phenomena. The end of transition generally produces a sharp peak in heating and is easily recognized by use of the phase-change-paint technique, since this region will melt early. The end of transition on the forebody center line occurs at about one-fourth of the model length and is swept from the center line roughly parallel to the fuselage outline. On the wing, the presence of an early melt is indicated by contour lines roughly parallel to the leading edge; thus, the presence of transition is shown. (This transition location is also shown in "Analysis of Results.") As the angle of attack increases (figs. 8(b) and 8(c)), the forebody transition pattern loses its "V" shape and the wing transition moves toward the leading edge and disappears at the higher angles of attack. Also, the tip-fin interference becomes more severe until, at angles of attack of $17.6^o$ and $24^o$, it is the most severe heating on the windward side.

The lower Reynolds number ($R_l \approx 5 \times 10^6$) patterns on the windward side are presented in figure 9 at angles of attack of $0.6^o$, $11.9^o$, and $24^o$. At this reduced Reynolds number, transition location has moved back from the nose as would be expected, but the tip-fin interference heating on the wing is as severe as at the leading edges. As angle of attack increases, transition moves further from the nose, whereas on the wing the transition location becomes more definite at $\alpha = 11.9^o$. At $\alpha = 24^o$, there are large areas on the inboard portion of the wing subject to high heating from either a transition effect and/or interference heating from the strake.

Windward-side oil flows at the higher Reynolds number ($R_l = 15 \times 10^6$) are presented in figure 10 for angles of attack of $6.2^o$, $11.9^o$, and $17.6^o$. The fuselage is divided into four sections of roughly the same length in order to facilitate discussion of the oil-flow patterns on the fuselage. These four sections are the nose, forward fuselage, compression ramp, and exhaust ramp. At the lower angle of attack (fig. 10(a)), the oil flow near the nose shows evidence of highly divergent surface flow; however, upon moving aft to the forward fuselage, where the forward delta-wing limits flow around the body to the lee side, the divergence is less noticeable. On the compression ramp, the flow is more free to expand sideways because of a change in both incidence of the local wing surface, $4.2^o$ for the forward delta to $0^o$ for the main wing, and an increasing vertical height in profile from the forebody surface to the wing surface (fig. 2). This cross flow near the surface causes highly curved oil-flow lines near the compression ramp edges. Near the compression ramp center line, there is a longitudinal pressure gradient due to the presence of the exhaust ramp, and the surface flow in this region shows less tendency to diverge. After expanding onto the exhaust ramp, the flow appears to separate at approximately 20 percent of the ramp length. The oil flow at the rear of the exhaust is dominated by the vortex patterns formed by the expansion of the wing flow into this region. The very narrow forward delta wing, or strake, exhibits oil-flow patterns that diverge from the center of the wing surface, and indicate a complex flow in this region possibly because of the transverse flow component from the forward forebody. The impingement of the transverse flow component from the compression ramp onto the main wing is more evident and causes an oil accumulation line on the wing similar to a separation line, which indicates the fuselage has induced a separated region on the wing. The wing oil

flow near the leading edge also indicates inflow from the leading edges and a subsequent turning parallel to the main flow direction. Near the rear of the wing, the flow is influenced by the tip-fin interference, flow compression due to elevon deflection, and transverse flow due to the low pressure region of the exhaust ramp. The elevons essentially mirror the wing patterns except for a region near the hinge line on the 12° deflected elevon (top half of the photograph), which may indicate local separation. As the angle of attack is increased to 11.9°, the influence on the wing from the compression ramp is decreased and the separation line on the exhaust ramp is more definite. At $\alpha = 17.6°$, surface flow divergence is more severe on the entire fuselage, excluding the exhaust ramp, which now appears to separate immediately, reattach, and separate again, except the center line which remains attached. There is no strong interaction of the fuselage on the main wing, and there is no inflow from the wing leading edges.

## Windward Elevons

Figure 11 presents heating data for positive elevon deflections of 6° and 12° measured with respect to the model reference line. (The 6° deflection is on the right wing.) Figures 11(a) to 11(e) cover data for these two elevon deflections at five vehicle angles of attack all at a nominal value of Reynolds number ($R_l = 15 \times 10^6$). In general, the heating patterns are complex and are influenced by the tip-fin interference at the elevon outboard, the expanding flow into the exhaust region on the elevon inboard, separation at the hinge line, distance from the wing leading edge, and location of transition on the wing.

The contour-line drawing in figure 11(a) ($\alpha = 0.6°$) is presented at twice the size of the subsequent figures in order to better show the details of the elevon heating patterns. The 6° deflection on the right wing (bottom of figure) shows the highest value of heating in the hinge-line region and possibly indicates a pocket of separated turbulent flow, even though separated flow would not usually be expected at this low deflection angle. (See ref. 10.) Several longitudinal spikes define the extent of the tip-fin interference at the outboard end of the elevon. Further inboard the heating appears first to be influenced by the wing flow, that is, the contour lines run chordwise, and still further inboard the contours are spanwise since they are influenced by flow originating at the hinge line, as would be the case for separated flow. The inboard end of the elevon is relatively cool and reflects the effects of increased boundary-layer thickness due to high local Reynolds number from the inboard wing flow. The 12° deflected elevon on the left wing (top of figure) indicates that phenomena at the hinge line, possibly separation, dominate the elevon local flow field with an overlay of effects due to the tip fin and expansion into the exhaust region. There are no oil-flow data for $\alpha = 0.6°$ corresponding to figure 11(a).

Figure 11(b) at $\alpha = 6.2°$ shows less effect from the hinge-line flow than at $\alpha = 0.6°$ for both the 6° and 12° deflected elevons. The elevon flow field appears to be influenced primarily by the wing flow field. Figure 10(a) is a picture of the oil flow for $\alpha = 6.2°$ and substantiates the existence of the

tip-fin interference. Also, no separated region can be seen in the vicinity of the elevon hinge lines.

Figures 11(c) and 10(b) present heating and oil-flow data for $\alpha = 11.9^{\circ}$ and show no detectable separation at the hinge line. For the $6^{\circ}$ deflection, this allows the heating contours to transfer from the wing to the elevon with a jump at the hinge line, except near the tip fin. The $12^{\circ}$ elevon also shows a more regular flow field with heating contours aligned more with the wing flow field than with the hinge line.

At $\alpha = 17.6^{\circ}$ (fig. 11(d)), the elevon heating again changes character and exhibits contours aligned more with the hinge line than with wing contour lines. Oil flow for this case (fig. 10(c)) does not provide any additional information to explain this change. (Note the missing tip fin adjacent to the $12^{\circ}$ elevon.) An increase in angle of attack to $24^{\circ}$ (fig. 11(e)) now shows patterns strongly influenced by the hinge line. There is no oil flow for this angle of attack. Note that the elevon heating is now the most severe on the vehicle.

## Fuselage Side

Heating at a nominal $R_l$ of $15 \times 10^6$ and angles of attack of $0.6^{\circ}$, $6.2^{\circ}$, and $11.9^{\circ}$ on the fuselage side is shown in figure 12 primarily to show the interference heating on the fuselage side from the strake-wing juncture and the wing. Figure 12(a) shows heating at the strake-fuselage juncture, the areas of highest heating occurring just forward and just aft of the strake-wing juncture. The heating on the fuselage at the wing-strake juncture is low and is difficult to interpret since there are no oil-flow data for $\alpha = 0.6^{\circ}$. However, for $\alpha = 6.2^{\circ}$ (fig. 12(b)), there is an accompanying oil-flow picture (fig. 13(a)) which indicates flow separation at the strake-fuselage and the wing-fuselage junctures. However, this separation is small, or nonexistent, at the wing-strake-fuselage juncture.

As $\alpha$ increases to $11.9^{\circ}$ (fig. 12(c)), the effect at the wing-strake juncture disappears and the fuselage heating mechanism becomes a fully developed vortex as shown by the appropriate oil-flow patterns (fig. 13(b)). The lower length Reynolds number ($R_l = 5 \times 10^6$) produces quite different results and shows patterns emanating from the strake vertex but little effect from the rest of the strake or wing (fig. 14). As $\alpha$ increases, less of the fuselage is affected. There are no oil-flow pictures at $R_l = 4 \times 10^6$.

## ANALYSIS OF RESULTS

Several regions of the vehicle were chosen for analysis to represent sizable portions of the thermal protection system. The forebody center line is representative of the windward fuselage, and the line normal to the wing leading edge is representative of the windward wing surface. Windward surfaces were analyzed as a function of angle of attack at the maximum Reynolds number capability of the facility, since windward thermal protection systems may be designed by high-angle-of-attack requirements. The aircraft lee-side analysis

was conducted spanwise along the $x/l = 0.8$ station to represent the bulk heating of the wing and fuselage top. Of particular concern in this case was the extrapolation of the wind-tunnel heating results to the higher Reynolds number in flight. Thus, this investigation was conducted at constant angle of attack and as a function of Reynolds number. Laminar theories were calculated by Monaghan's T-prime method (ref. 11) and turbulent theory by the Spalding-Chi method modified for heat transfer as in reference 12. Boundary-layer edge conditions were calculated by using the tangent cone assumption for the fuselage and tangent wedge for the wings and the computer code described in reference 13.

## Forebody Lower Center Line

Figure 15 presents data, data fairing, and theory for a model length Reynolds number of approximately $15 \times 10^6$ and at angles of attack of $0.6°$, $6.2°$, $11.9°$, $17.6°$, and $24°$. Figure 15(a) shows the results of four separate tunnel runs at the lower angle. The location of the end of transition is seen to vary from $x/l = 0.16$ to $x/l = 0.26$ and there is scatter in the heating level from run to run. The variation in transition location is at least partially due to the different surface textures of the phase-change paints (ref. 14); whereas the scatter in heating level is a function of transition location, dimensional accuracy of the models, repeatability of angle of attack, and tunnel conditions, as well as the inaccuracies inherent in the phase-change technique as discussed in reference 8. To facilitate discussion of trends and to simplify subsequent presentation of these data as a function of angle of attack, the data are approximated by a fairing line. The turbulent strip theory presented for comparison was calculated assuming a virtual origin to exist at $x/l = 0.2$. Also, turbulent theory is presented using Reynolds number based on body width. Reynolds number based on body width is equivalent in concept to basing the Reynolds number on cylinder diameter in swept cylinder theory as applied to forebody heating in reference 15. In this case, however, the equivalent sweep angle is out of the range of applicability of the theory used in reference 15 and the turbulent strip theory for conical flow is used instead (ref. 12).

Figures 15(b), 15(c), 15(d), and 15(e) are treated in a manner similar to figure 15(a). Figure 15(b) exhibits less scatter in heating level for the four runs at $6.2°$ deflection angle and shows a divergence between data and theory based on length Reynolds number as $x/l$ increases. At $x/l > 0.4$, when the flow is fully turbulent, the theory gives better agreement when based on body width than when based on length from transition location. Figure 15(c) has data scatter and the data and theory show reasonable agreement within the limits of the scatter. Figure 15(d) shows more variation in transition location than the lower angles of attack as well as divergence between the data line and theory based on $R_x$. Theory based on $R_w$ underpredicts the data but exhibits a similar trend. Figure 15(e) has much the same character as figure 15(d) with variation in transition location but more confidence in data level. Figure 16 is a summary plot of figures 15(a) to 15(e) comparing the data fairing line with the turbulent theory based on $R_x$ and theory based on $R_w$ for the body width at a constant longitudinal station $x/l = 0.5$. Heating level is presented as a function of vehicle angle of attack plus local deflection angle. The turbulent theory based on $R_x$ is shown to consistently underpredict the data at all flow

10

deflection angles but gives good agreement in trend up to $\alpha + \delta = 18^\circ$. Theory based on $R_w$ gives better overall agreement with the heating level but still does not match either the trend or the level at $\alpha + \delta > 18^\circ$. Reference 16 presents center-line heating data (fig. 52-9 in ref. 16) on a $75^\circ$ swept delta wing at $M = 9.6$ which shows good agreement with laminar strip theory up to the flow-deflection angle approaching $20^\circ$. The slope of the data first increases and then resumes its original trend as the flow angle reaches $30^\circ$, much as the data fairing line of figure 16. The data of reference 16 are predicted reasonably well by streamline divergence theory at deflection angles of $30^\circ$, and cross-flow theory as deflection angles approach $60^\circ$. Thus, it would appear that theory based on width Reynolds number $R_w$ is appropriate for this narrow, slightly (spanwise) convex, highly swept forebody (fig. 2), until the surface inclination to the flow $(\alpha + \delta)$ approaches $18^\circ$. At greater angles, account must be taken of the additional boundary-layer thinning due to three-dimensional effects such as streamline divergence.

## Wing Bottom

In order to compare data and theory on the wing bottom, a line normal to the wing leading edge and emanating from the intersection of the wing leading edge and the $x/l = 0.8$ station was chosen for analysis. This location is between wing-body junction and tip-fin disturbances and should be representative of the nominal delta-wing heating. In a manner similar to the forebody analysis, dimensionless heating rate is presented as a function of distance from the leading edge, followed by a summary plot of heating as a function of angle of attack.

Figure 17(a) presents data at $\alpha = 0.6$ from four tunnel runs, laminar theory, and turbulent theory based on a virtual origin location at $N/c_F$ of 0.1. Additionally, the turbulent data are represented by a data fairing for use in the summary plot. For this low angle of attack, there is data scatter from run to run and transition location is nebulous. In the laminar region, turbulent values of the ratio of adiabatic to total temperature were used in the data reduction which will raise the value of the heat-transfer coefficient above the true laminar level on the order of 30 percent. Nevertheless, the laminar theory is still shown for reference purposes. The turbulent theory predicts the data trend and is in reasonable agreement with the data level. As the angle of attack increases to $6.2^\circ$, in figure 17(b), the transition location becomes better defined and the data scatter decreases. Turbulent theory is seen to predict the trend and somewhat underpredict the level of the data, based on a virtual origin location at $N/c_F = 0.037$.

A further increase to an angle of attack of $11.9^\circ$ (fig. 17(c)) results in data which show no discernible peak heating at the end of transition, and thus indicate that transition is very near the leading edge. The usual data scatter from run to run has decreased, and possibly indicates a boundary-layer disturbance more severe than the normal mechanisms which influence transition location. The turbulent theory based on distance from the leading edge gives reasonable agreement with the data level, but provides a less satisfactory prediction of the trend than was the case at the lower angles of attack. The data are seen to be above the turbulent theory line at small values of $N/c_F$, and as

11

the leading edge is approached, the disparity increases. The data point nearest the leading edge, $N/c_p = 0.003$, is near the region of intersecting laminar and turbulent theory, or $N/c_p = 0.002$. The local Reynolds number at $N/c_p = 0.003$ has a value of $0.034 \times 10^6$ which is much less than normally expected for transition. A possible explanation for this early transition is boundary-layer contamination from the strake upstream of the delta wing (fig. 2).

Only two runs were available to provide data for the $\alpha = 17.6°$ case shown in figure 17(d), but the trend of data is similar to that of figure 17(c) and the turbulent theory now markedly underpredicts the data level. This trend might be expected as the angle of attack increases and the character of the flow tends to become three dimensional (ref. 16). Note once again the flow is turbulent very close to the leading edge. Figure 17(e) at an angle of attack of $24°$ also shows turbulent flow close to the leading edge. Turbulent theory predicts the trend but underpredicts the heating level. The bump in the data in the region $0.12 < N/c_p < 0.18$ is suspected to be heating caused by interference emanating from the upstream strake. This region is evident in figure 8(e) as the area enclosed by contour line number 5 on the wing bottom.

The wing-bottom data are summarized in figure 18 by presenting heating as a function of angle of attack at $N/c_p = 0.12$. At angles of attack of $12°$ and below, the theory predicts the trend and somewhat underpredicts the data. At angles of attack greater than $12°$, the prediction of the trend is poor and the theory increasingly underpredicts the data with increasing angle of attack. This is an expected result since as the angle of attack increases, three-dimensional effects become more prominent. The data curve has points of inflection and is similar to the fuselage data of figure 16 as well as the data of reference 16 which were discussed earlier.

## Fuselage and Wing Lee Side

Figure 19 presents spanwise heat-transfer coefficient ratio data at a longitudinal station $x/l = 0.8$ for a nominal angle of attack of $11.9°$. The data are presented as a function of $S/D$ with the lee-side center line serving as the zero point on the figure and $S/D = 1.55$ representing the wing leading edge. The fuselage-wing junction at $x/l = 0.8$ is at $S/D = 0.74$. Both right and left sides of the model are presented in the figures. Since the wing-top leading-edge cross section is a circular arc becoming tangent to a flat top, the heat-transfer coefficient is seen to decrease rapidly with increasing distance from the leading edge (decreasing values of $S/D$), that is, the normal rapid decrease expected near a leading edge is further enhanced by a rapid decrease in flow-deflection angle. The data are compared with turbulent theory, and as the flow begins to expand, local flow properties are calculated by assuming a Prandtl-Meyer expansion until the pressure coefficient decreases to the $-1/M^2$ value $(p/p_\infty = 0.3)$, which is recommended as a limit value in reference 17. At this point the flow on the wing is assumed to expand no further and the change in the heat-transfer coefficient becomes a function of length Reynolds number only. The theory is calculated in the same manner for the fuselage top $(S/D < 0.74)$ but $R_x$ is a constant and $h/h_s$ becomes con-

stant when $C_p$ becomes equal to $-1/M^2$. An additional calculation at $C_p = 0$ ($p/p_\infty = 1$) is shown for reference purposes.

From figure 7, it may be seen that the lee-side heat-transfer patterns are complex and change with Reynolds number. In order to investigate the changes with Reynolds number, figure 19 presents data and theory comparison over a 5 to 1 range in Reynolds number at an angle of attack of $10^o$, which is estimated to be a typical flight angle of attack for this vehicle. The changes in pattern make direct comparison of the results difficult; therefore, the heat-transfer coefficient over the fuselage (S/D < 0.74) was integrated to remove the effects of pattern and indicate the area-averaged level. These average heating rates are presented in figure 20 as a function of Reynolds number with the Prandtl-Meyer expansion plus $C_p = -1/M^2$ limit and $C_p = 0$ limit included for comparison purposes. Note that the results fall between the $C_p = 0$ and the Prandtl-Meyer expansion with $C_p = -1/M^2$ limits and are best predicted by the Prandtl-Meyer expansion with $C_p = -1/M^2$ limit.

## CONCLUSIONS

Examination of a complete research airplane configuration with the phase-change-paint technique has shown the heating patterns to be very complex. Specific conclusions are as follows:

(1) At values of angle of attack plus local flow-deflection angle less than $18^o$, turbulent theory adjusted for transition location and using tangent cone local conditions gave reasonable agreement with the windward fuselage center-line heat-transfer coefficient data fairings. At values greater than $18^o$, these simple theories become inadequate.

(2) At angles of attack less than $12^o$, turbulent theory adjusted for transition location and using tangent wedge local conditions gave reasonable agreement with the windward surface data fairings at a turbulent, undisturbed location on the wing.

(3) Transition Reynolds numbers recorded on the wing bottom, at angles of attack of $11.9^o$ and greater, are much lower than normally expected and have a value no higher than 34 000 based on length normal to the leading edge and tangent wedge edge conditions.

(4) The lee-side area-averaged heat-transfer coefficient across the fuselage (at the station investigated) is bracketed by turbulent theory based on an expansion limited to free-stream pressure, pressure coefficient $C_p$ equal to zero, and expansion limited to a pressure coefficient equal to $-1/M^2$. The data level is better predicted by a Prandtl-Meyer expansion where the pressure is allowed to drop no lower than $C_p = -1/M^2$.


Langley Research Center
National Aeronautics and Space Administration
Hampton, VA 23665
January 24, 1978

## REFERENCES

1. Kirkham, F. S.; Jones, R. A.; Buck, M. L.; and Zima, W. P.: Joint USAF/NASA Hypersonic Research Aircraft Study. AIAA Paper No. 75-1039, Aug. 1975.

2. Penland, Jim A.; Fournier, Roger H.; and Marcum, Don C., Jr.: Aerodynamic Characteristics of a Hypersonic Research Airplane Concept Having a 70° Swept Double-Delta Wing at Mach Numbers From 1.50 to 2.86. NASA TN D-8065, 1975.

3. Creel, Theodore R., Jr.; and Penland, Jim A.: Low-Speed Aerodynamic Characteristics of a Hypersonic Research Airplane Concept Having a 70° Swept Delta Wing. NASA TM X-71974, 1974.

4. Clark, Louis E.; and Richie, Christine B.: Aerodynamic Characteristics at Mach 6 of a Hypersonic Research Airplane Concept Having a 70° Swept Delta Wing. NASA TM X-3475, 1977.

5. Small, William J.; Weidner, John P.; and Johnston, P. J.: Scramjet Nozzle Design and Analysis as Applied to a Highly Integrated Hypersonic Research Airplane. NASA TM X-71972, 1974.

6. Edwards, C. L. W.; Small, W. J.; Weidner, J. P.; and Johnston, P. J.: Studies of Scramjet/Airframe Integration Techniques for Hypersonic Aircraft. AIAA Paper No. 75-58, Jan. 1975.

7. Lawing, Pierce L.: Analysis of Various Descent Trajectories for a Hypersonic-Cruise, Cold-Wall Research Airplane. NASA TN D-7860, 1975.

8. Jones, Robert A.; and Hunt, James L.: Use of Fusible Temperature Indicators for Obtaining Quantitative Aerodynamic Heat-Transfer Data. NASA TR R-230, 1966.

9. Schultz, D. L.; and Jones, T. V.: Heat-Transfer Measurements in Short-Duration Hypersonic Facilities. AGARD-AG-165, Feb. 1973.

10. Popinski, Z.; and Ehrlich, C. F.: Development Design Methods for Predicting Hypersonic Aerodynamic Control Characteristics. AFFDL TR-66-85, U.S. Air Force, Sept. 1966. (Available from DDC as AD 644 251.)

11. Monaghan, R. J.: An Approximate Solution of the Compressible Laminar Boundary Layer on a Flat Plate. R.&M. No. 2760, Brit. A.R.C., 1953.

12. Neal, Luther, Jr.; and Bertram, Mitchel H.: Turbulent-Skin-Friction and Heat-Transfer Charts Adapted From the Spalding and Chi Method. NASA TN D-3969, 1967.

13. Gentry, Arvel E.; and Smyth, Douglas N.: Hypersonic Arbitrary-Body Aerodynamic Computer Program (Mark III Version). Vol. II - Program Formulation and Listings. Rep. DAC 61552, Vol. II (Air Force Contract Nos. F33615 67 C 1008 and F33615 67 C 1602), McDonnell Douglas Corp., Apr. 1968. (Available from DDC as AD 851 812.)
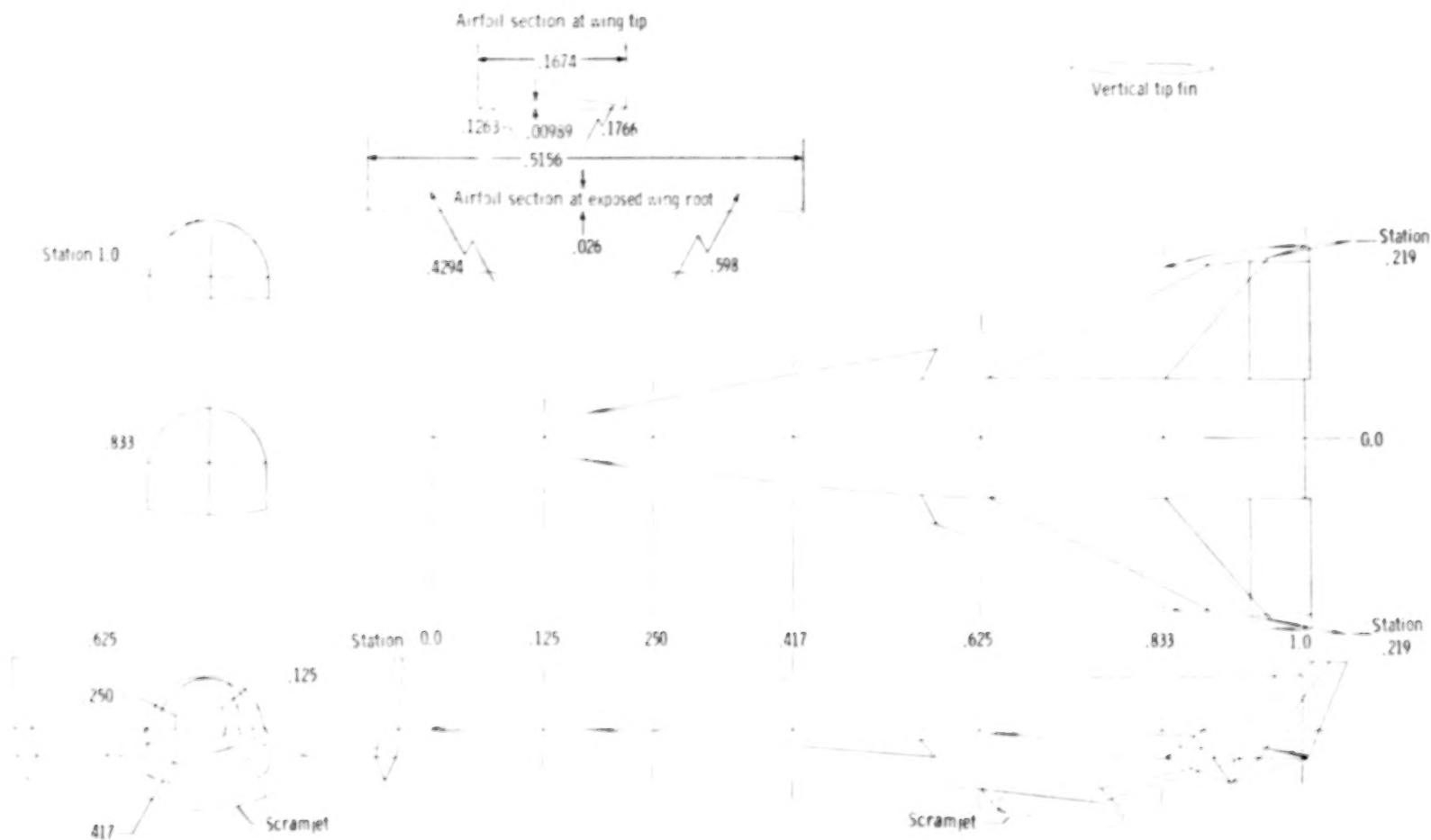
14. Johnson, Charles B.:  High Reynolds Number Turbulent Heating to Two Simpli-
    fied Shuttle Configurations.  Space Shuttle Aerothermodynamics Technology
    Conference, Volume II - Heating, NASA TM X-2507, 1972, pp. 347-373.

15. Mendelsohn, A. R.; Bourbin, M.; Jew, M.; and Osonitsch, C. W.:  A Review of
    the Grumman Orbiter Wind Tunnel Heat Transfer Tests.  Space Shuttle Aero-
    thermodynamics Technology Conference, Volume II - Heating, NASA TM X-2507,
    1972, pp. 297-345.

16. Bertram, Mitchel H.; Fetterman, David E., Jr.; and Henry, John R.:  The
    Aerodynamics of Hypersonic Cruising and Boost Vehicles.  Proceedings of
    the NASA-University Conference on the Science and Technology of Space
    Exploration, Vol. 2, NASA SP-11, 1962, pp. 215-234.  (Also available as
    NASA SP-23.)

17. Mayer, John P.:  A Limit Pressure Coefficient and an Estimation of Limit
    Forces on Airfoils at Supersonic Speeds.  NACA RM L8F23, 1948.

L-72-9142

Figure 1.- Photograph of research airplane concept with scramjet engine attached.

Airfoil section at wing tip

Vertical tip fin

Station 1.0

.833

.625

.417  Scramjet

Station 0.0    .125    .250    .417    .625    .833    1.0    Station .219

(a) Three-view drawing of model.

Figure 2.- Model details.   All dimensions have been normalized by body length ($\iota$ = 50.8 cm).

Reference chord sections

$6^0$

Fixed elevon deflections, $\delta_e$

Right wing

$12^0$

Left wing

$6^0$

$70^0$

$80^0$

X

Reference chord, $c_r$

Forebody compression angle, $\delta$

$6^0$

$4.2^0$
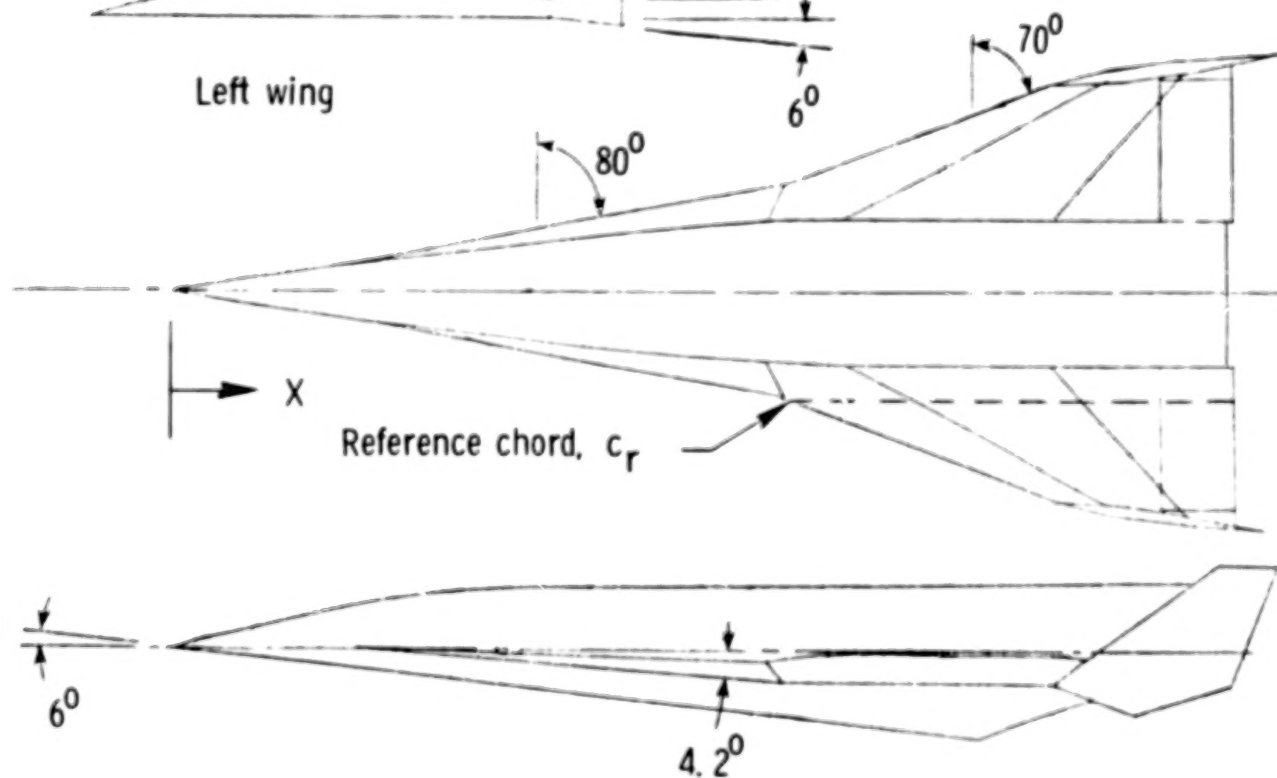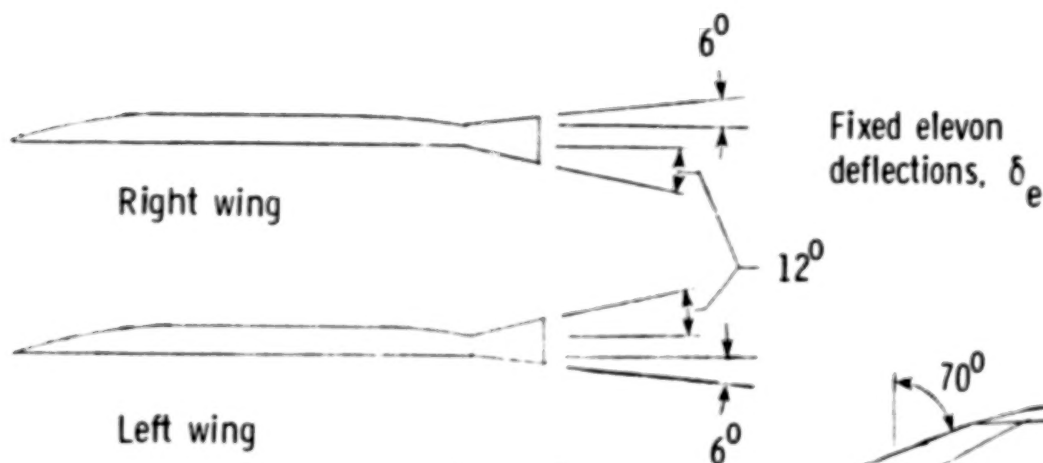
(b) Sketch showing wing reference chord, fixed elevon deflections, sweep angles, forebody compression angles, and forward delta or strake incidence.

Figure 2.- Concluded.
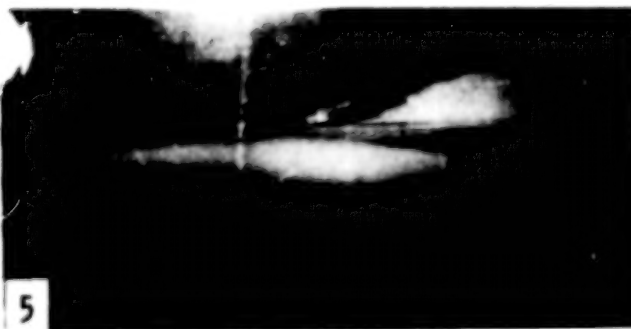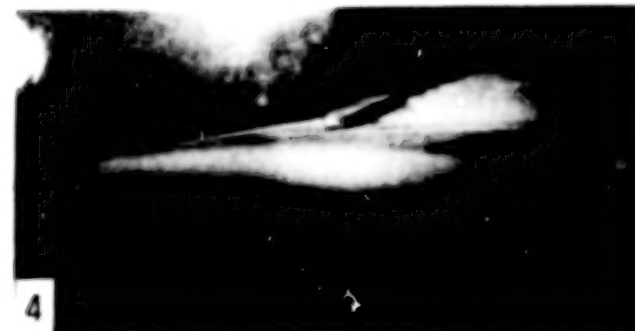
L-78-6

Figure 3.- Selected frames from motion-picture film for one run showing
paint melt-line progression with time.   View is from top.

HS= 1.24031E+03 WATTS/METER(SQ)-DEG-K

| CONTOUR | H/HS | TAW/TO |
|---|---|---|
| 1 | 2.17310E-01 | 9.33950E-01 |
| 2 | 1.37439E-01 | 9.33950E-01 |
| 3 | 7.93504E-02 | 9.33950E-01 |
| 4 | 6.87195E-02 | 9.33950E-01 |
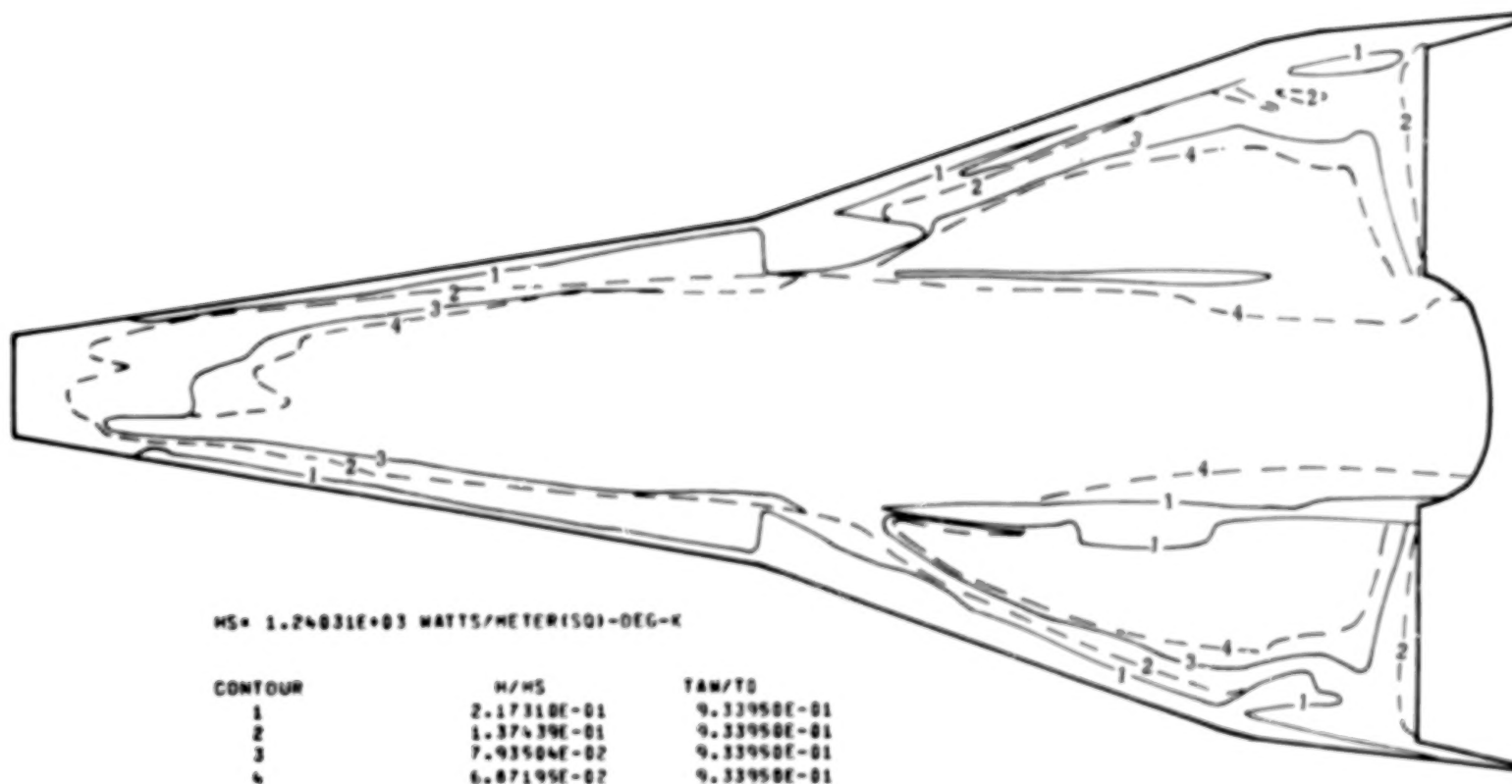
(a)  $\alpha = 6.2^{\circ}$;  $T_{pc} = 339$ K.

Figure 4.- Contour-line drawing of model lee side at  $R_l = 15 \times 10^6$.

20

HS= 1.23146E+03 WATTS/METER(SQ)-DEG-K.

| CONTOUR | H/+S | TAW/TC |
|---------|------|--------|
| 1 | 7.38633E-02 | 9.36700E-01 |
| 2 | 5.22299E-02 | 9.36700E-01 |
| 3 | 3.19434E-02 | 9.36700E-01 |
| 4 | 2.33576E-02 | 9.36700E-01 |
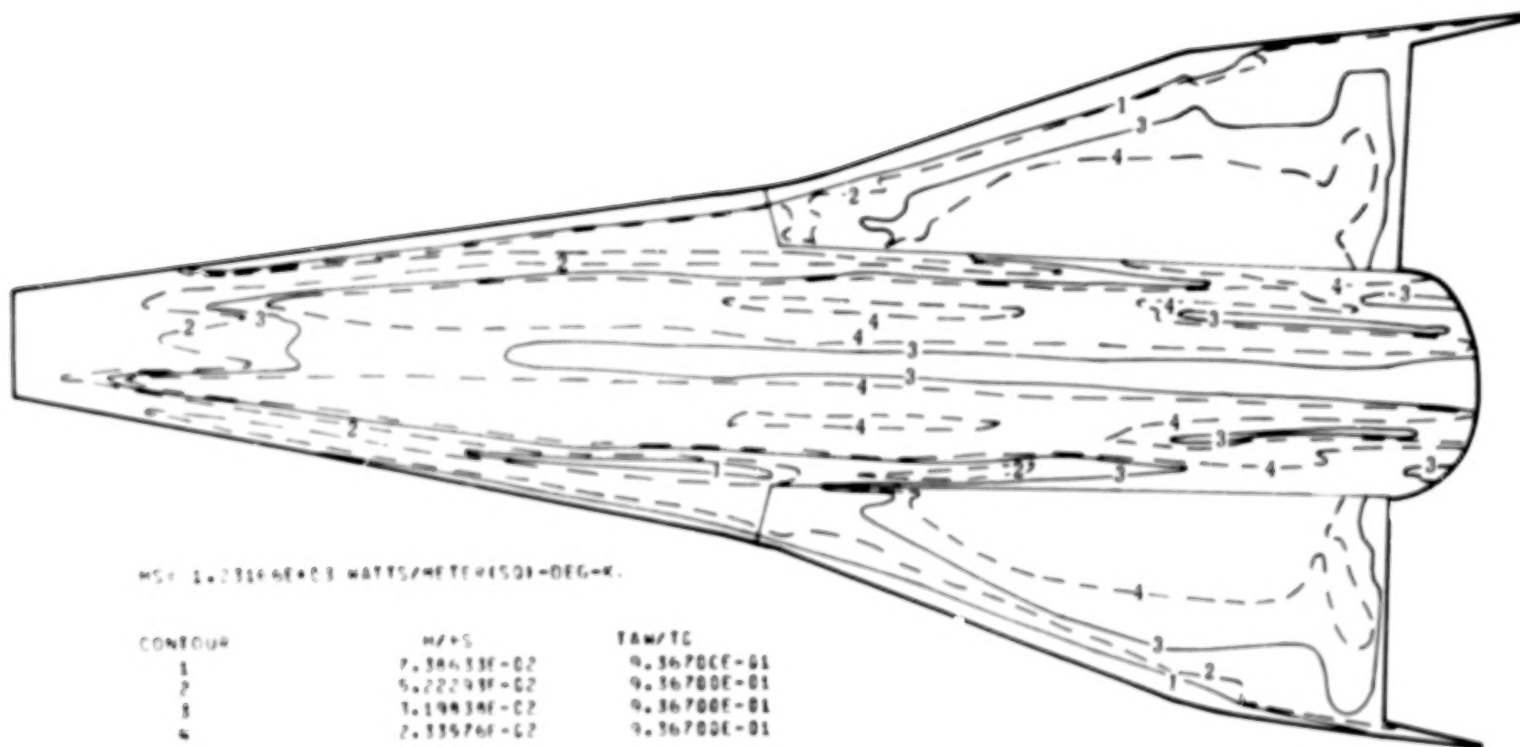
(b)   $\alpha = 11.9^{\circ}$;   $T_{pc} = 313$ K.

Figure 4.- Concluded.

$\delta_e = 12°$

$\delta_e = 6°$

L-78-7

(a) $\alpha = 6.2°$.

Figure 5.- Oil-flow photographs of model lee side.

$\delta_e = 12^o$

$\delta_e = 6^o$

Missing tip fin ⟶

(b) $\alpha = 11.9^o$.

Figure 5.- Concluded.

L-78-8

HS= 6.96663E+02 WATTS/METER(SQ)-DEG-K

| CONTOUR | H/HS | TAW/T0 |
|---------|-----------|-----------|
| 1 | 2.32467E-01 | 9.33160E-01 |
| 2 | 1.64662E-01 | 9.33160E-01 |
| 3 | 1.16434E-01 | 9.33160E-01 |
| 4 | 8.23310E-02 | 9.33160E-01 |
| 5 | 5.44873E-02 | 9.33160E-01 |
| 6 | 4.85562E-02 | 9.33160E-01 |
| 7 | 4.29155E-02 | 9.33160E-01 |
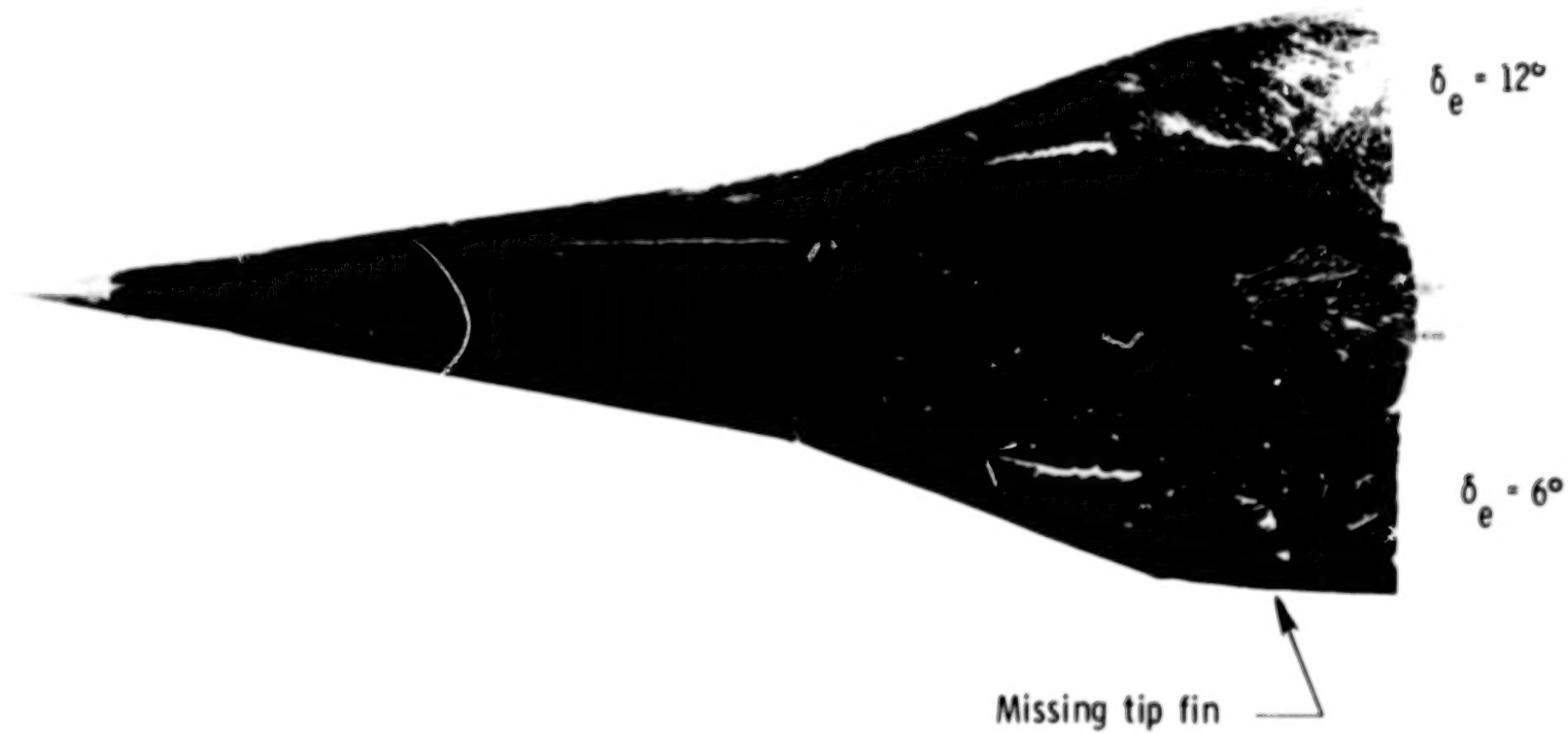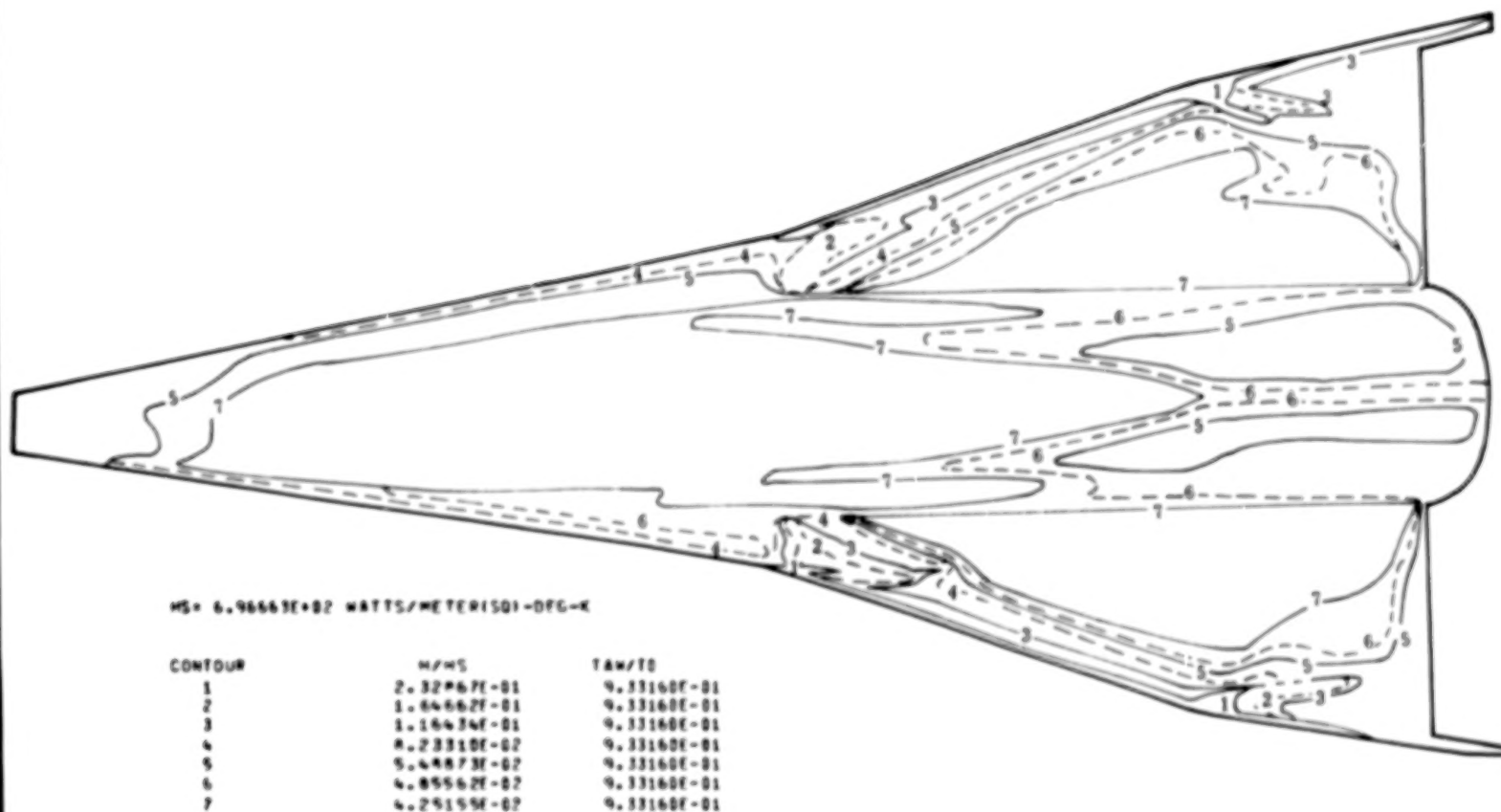
(a)  $\alpha = 0.6°$;  $T_{pc} = 313$ K.

Figure 6.- Contour-line drawing of model lee side at  $R_l = 4 \times 10^6$.

24

HS= 7.60493E+02 WATTS/METER(SQ)-DEG-K

| CONTOUR | H/HS | TAW/TO |
|---------|------|--------|
| 1 | 4.3924E-02 | 9.1668E-01 |
| 2 | 2.7702E-02 | 9.1668E-01 |
| 3 | 2.2642E-02 | 9.1668E-01 |
| 4 | 1.9643E-02 | 9.1668E-01 |
| 5 | 1.7569E-02 | 9.1668E-01 |
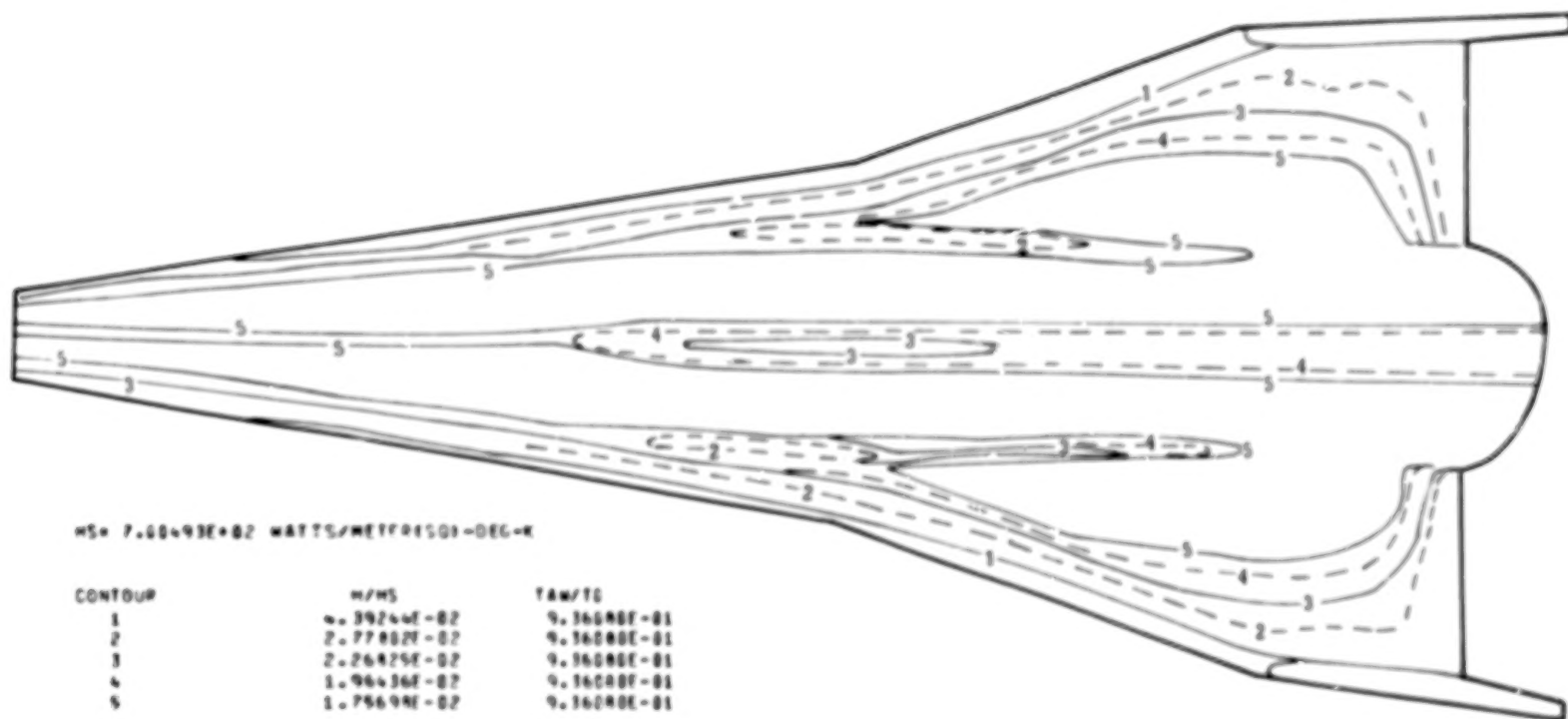
(b)  $\alpha = 11.9°$;  $T_{pc} = 313$ K.

Figure 6.- Continued.

25
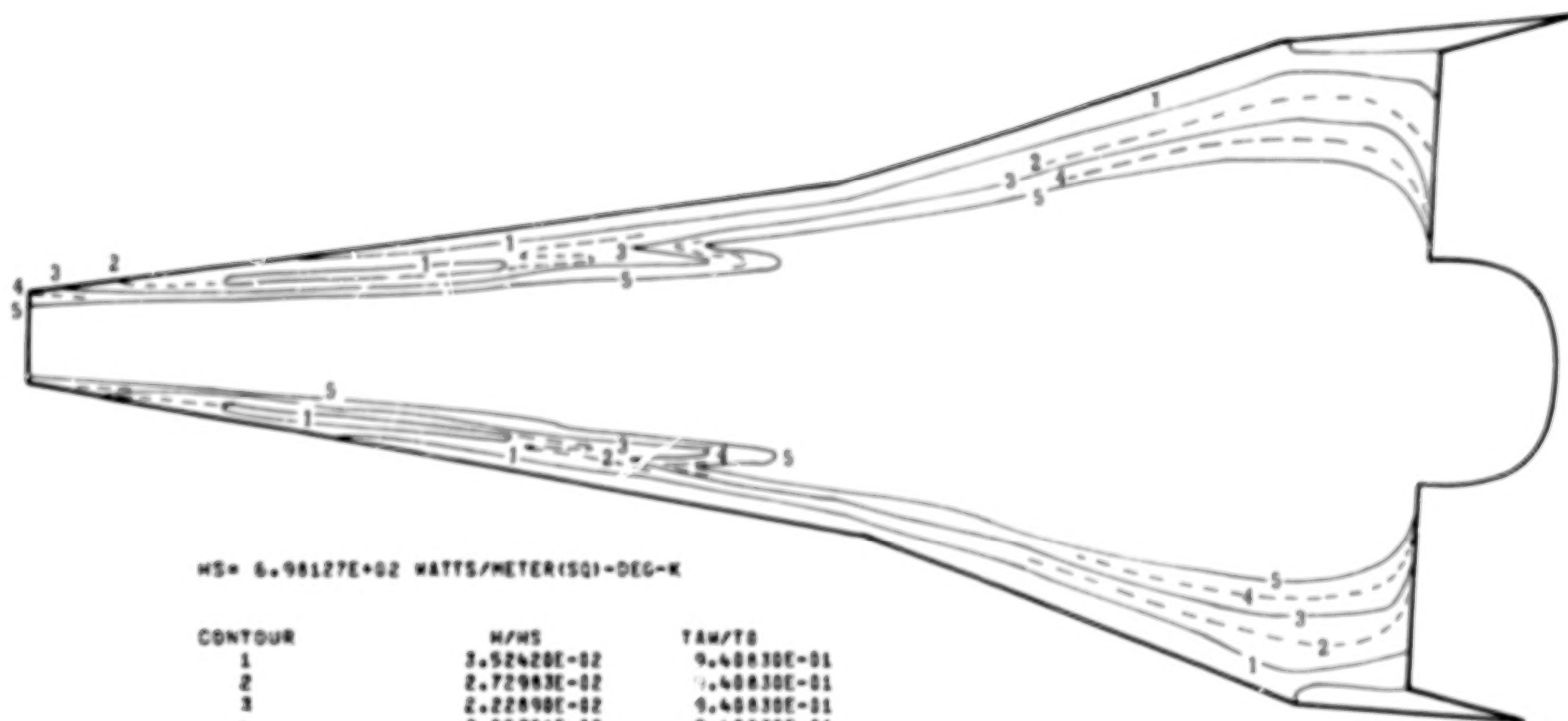
HS= 6.98127E+02 WATTS/METER(SQ)-DEG-K

| CONTOUR | H/HS | TAW/TS |
|---|---|---|
| 1 | 3.52428E-02 | 9.48830E-01 |
| 2 | 2.72963E-02 | 9.48830E-01 |
| 3 | 2.22898E-02 | 9.48830E-01 |
| 4 | 2.08701E-02 | 9.48830E-01 |
| 5 | 1.81989E-02 | 9.48830E-01 |

(c) $\alpha = 24°$; $T_{pc} = 313$ K.

Figure 6.- Concluded.

HS= 7.00493E+02 WATTS/METER(SQ)-DEG-K

| CONTOUR | H/HS | TAW/TO |
|---------|------|--------|
| 1 | 4.39244E-02 | 9.36080E-01 |
| 2 | 2.77802E-02 | 9.36080E-01 |
| 3 | 2.26825E-02 | 9.36080E-01 |
| 4 | 1.96436E-02 | 9.36080E-01 |
| 5 | 1.75698E-02 | 9.36080E-01 |
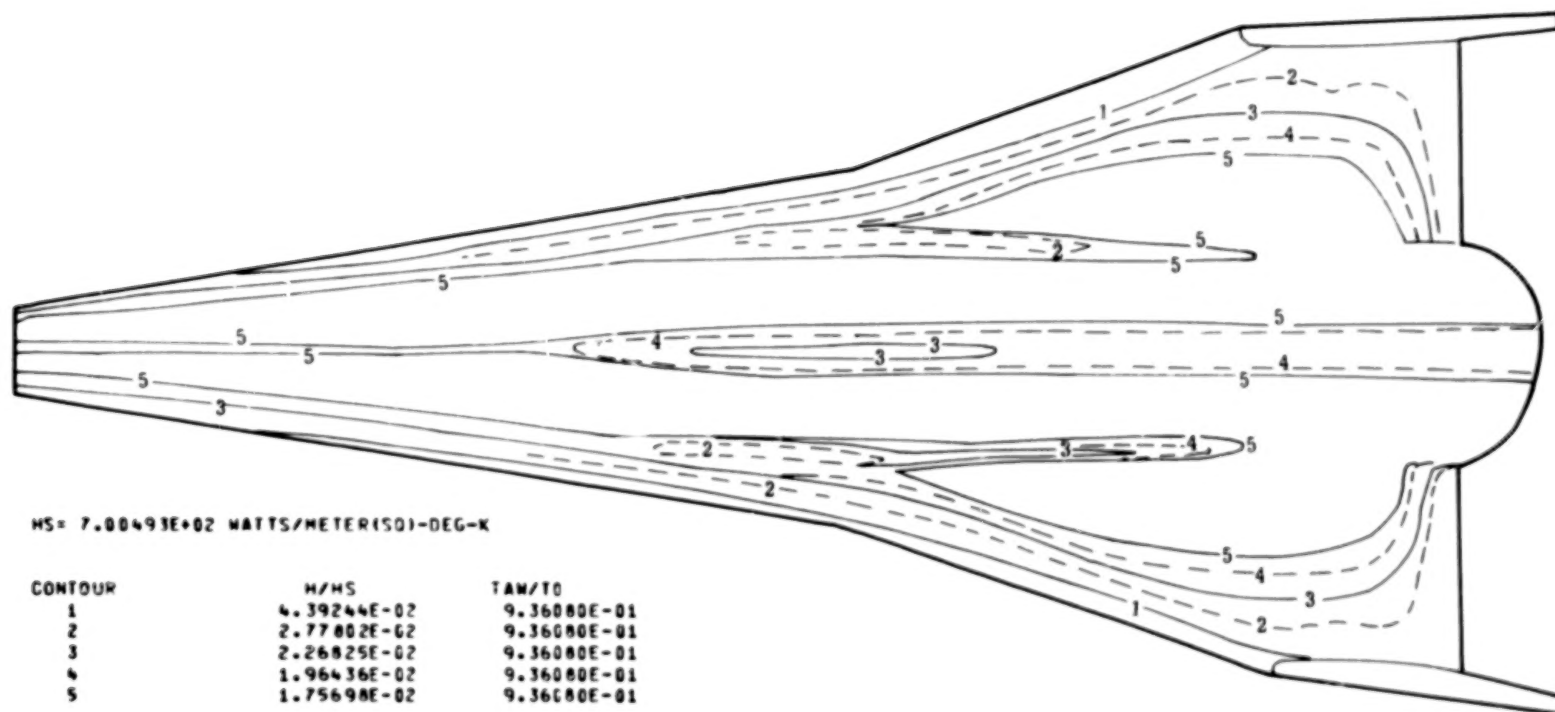
(a)   $R_l = 4.7 \times 10^6$;   $T_{pc} = 313$ K.

Figure 7.- Contour-line drawing of model lee side at   $\alpha = 11.9^o$.
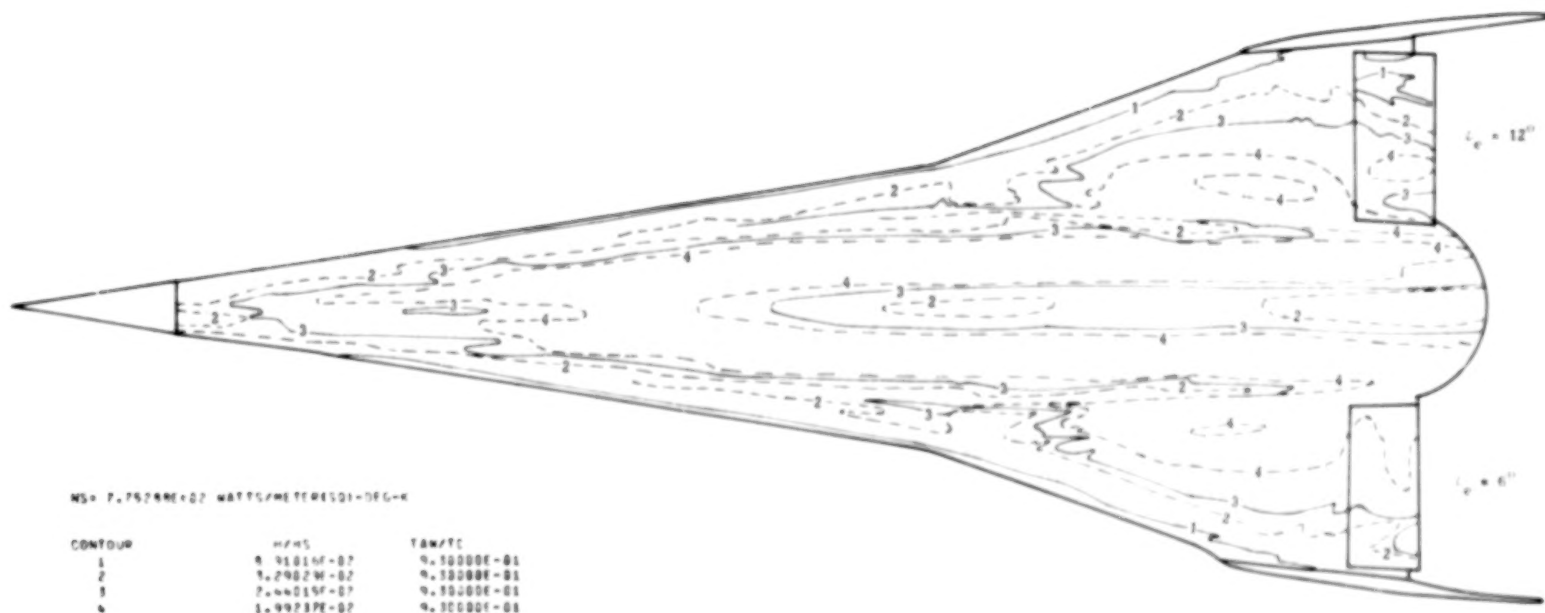
NS= 7.7529RE-02 WATTS/METERE(SQ)-DEG-K

| CONTOUR | H/HS | TAW/TC |
|---|---|---|
| 1 | 9.9101E-07 | 9.50000E-01 |
| 2 | 9.2902W-02 | 9.53000E-01 |
| 3 | 7.44019E-02 | 9.50000E-01 |
| 4 | 1.99739E-02 | 9.30000E-01 |

$\delta_e = 12°$

$\delta_e = 6°$

(b)  $R_1 = 5.3 \times 10^6$;  $T_{pc} = 313$ K.

Figure 7.- Continued.

25

| CONTOUR | H/HS | TAW/TO |
|---------|------|--------|
| 1 | 1.02666E-01 | 9.10000E-01 |
| 2 | 3.94627E-02 | 9.30000E-01 |
| 3 | 2.51478E-02 | 9.30000E-01 |
| 4 | 1.77922E-02 | 9.50000E-01 |

(c)  $R_l = 7.9 \times 10^6$;  $T_{pc} = 313$ K.

Figure 7.- Continued.

HS= 9.50001E+07 WATTS/METER(SQ)-DEG-K

| CONTOUR | H/HS | TAW/TS |
|---------|------|--------|
| 1 | 6.49159E-02 | 9.30000E-01 |
| 2 | 1.26659E-02 | 9.30000E-01 |
| 3 | 2.36509E-02 | 9.30000E-01 |
| 4 | 1.77922E-02 | 9.10000E-01 |

$\delta_e = 12^0$

$\delta_e = 6^0$
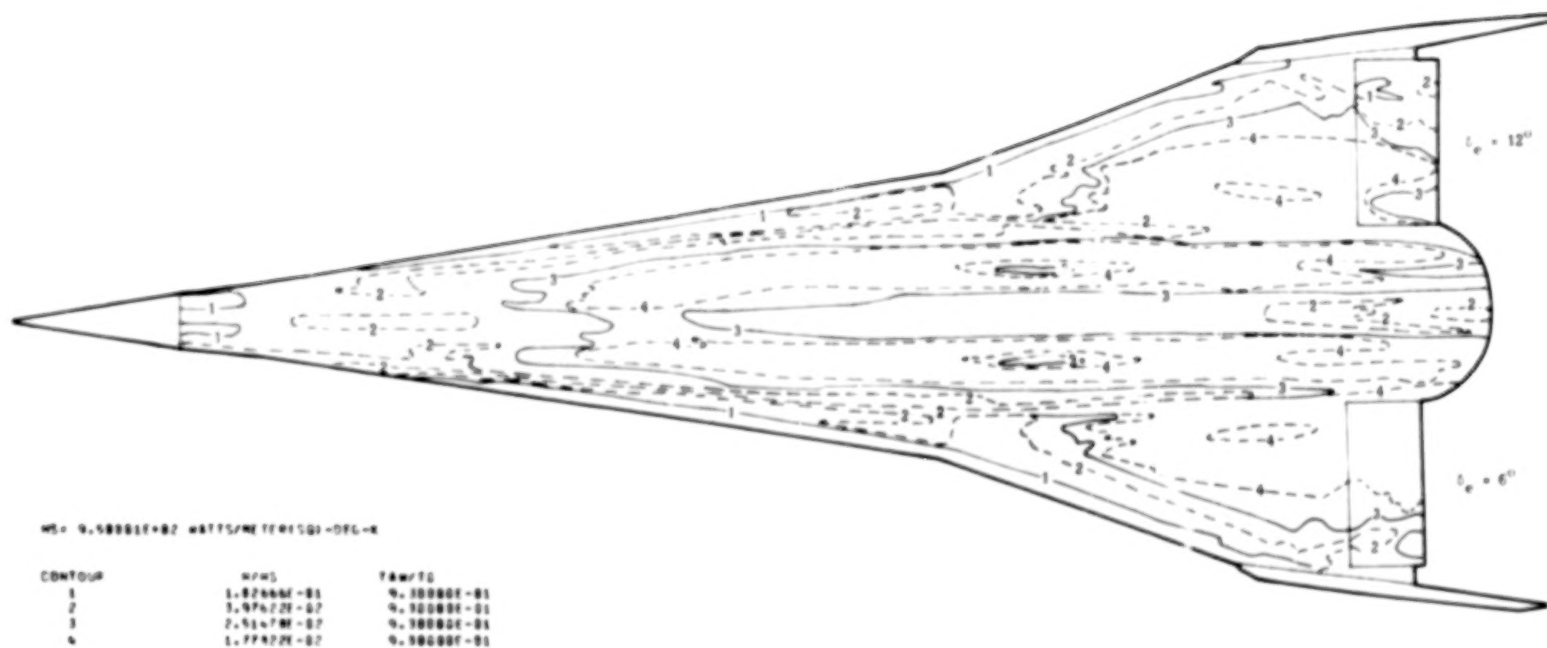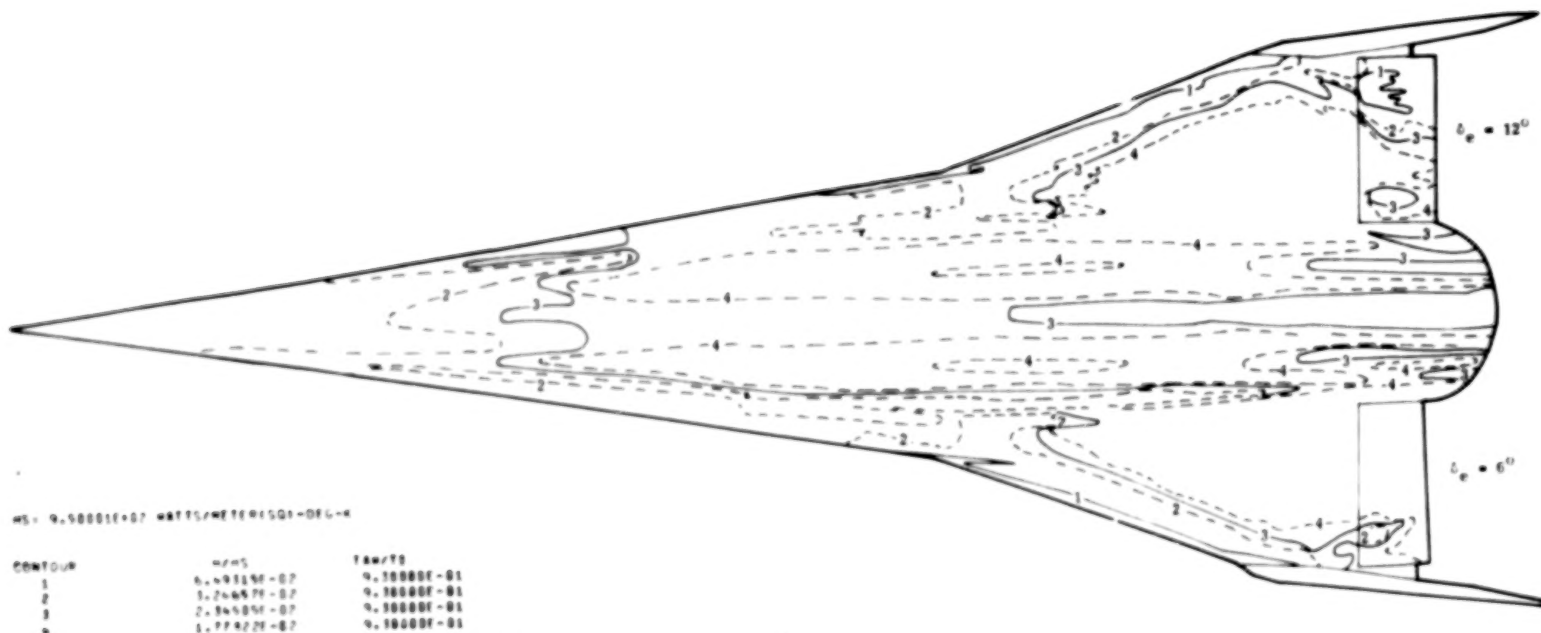
(d) $R_l = 13.6 \times 10^6$; $T_{pc} = 313$ K.
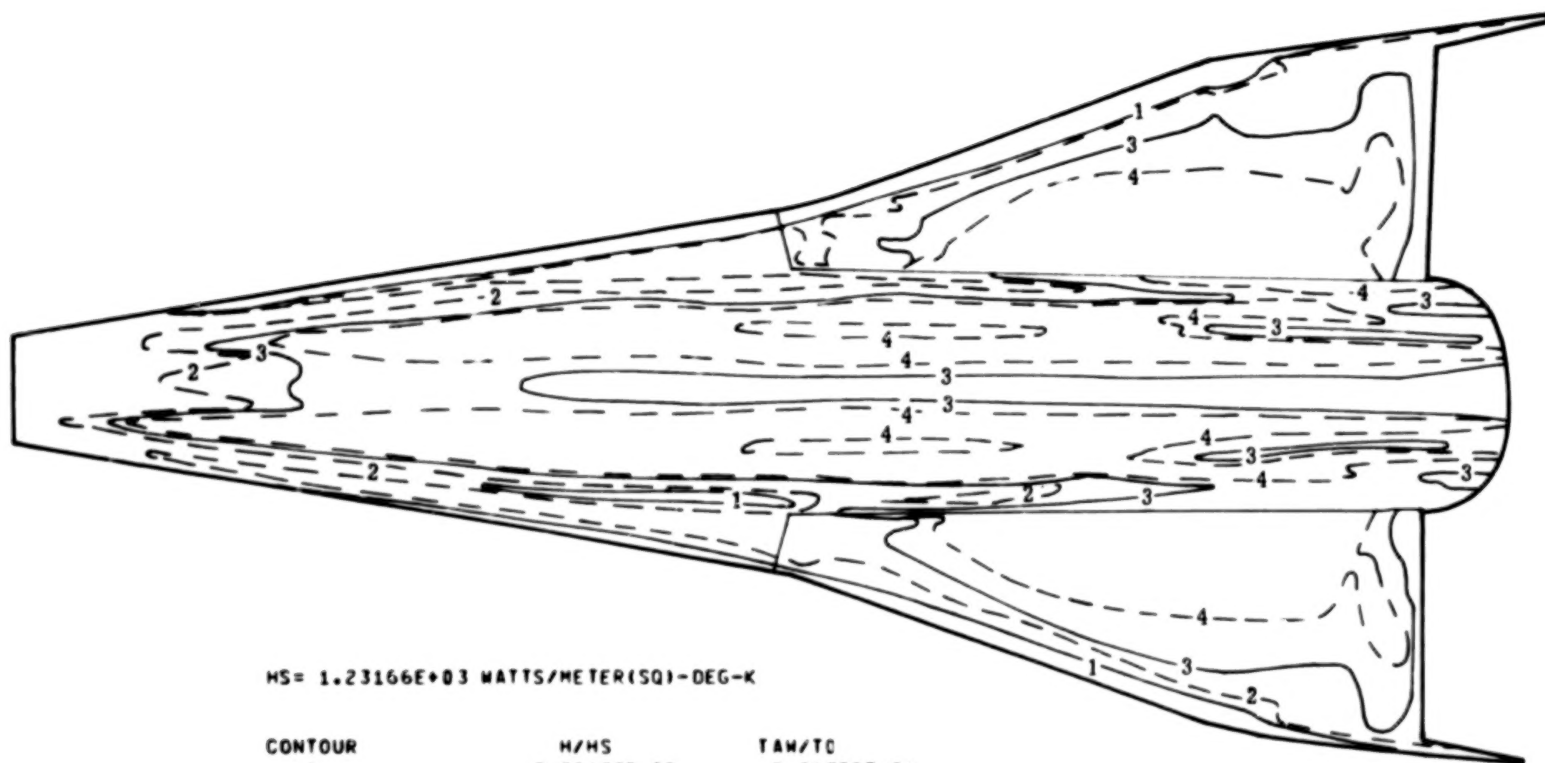
Figure 7.- Continued.

HS= 1.23166E+03 WATTS/METER(SQ)-DEG-K

| CONTOUR | H/HS | TAW/TO |
|---------|------|--------|
| 1 | 7.38633E-02 | 9.36700E-01 |
| 2 | 5.22293E-02 | 9.36700E-01 |
| 3 | 3.19438E-02 | 9.36700E-01 |
| 4 | 2.33576E-02 | 9.36700E-01 |

(e)  $R_l = 15.6 \times 10^6$;  $T_{pc} = 313$ K.

Figure 7.- Concluded.
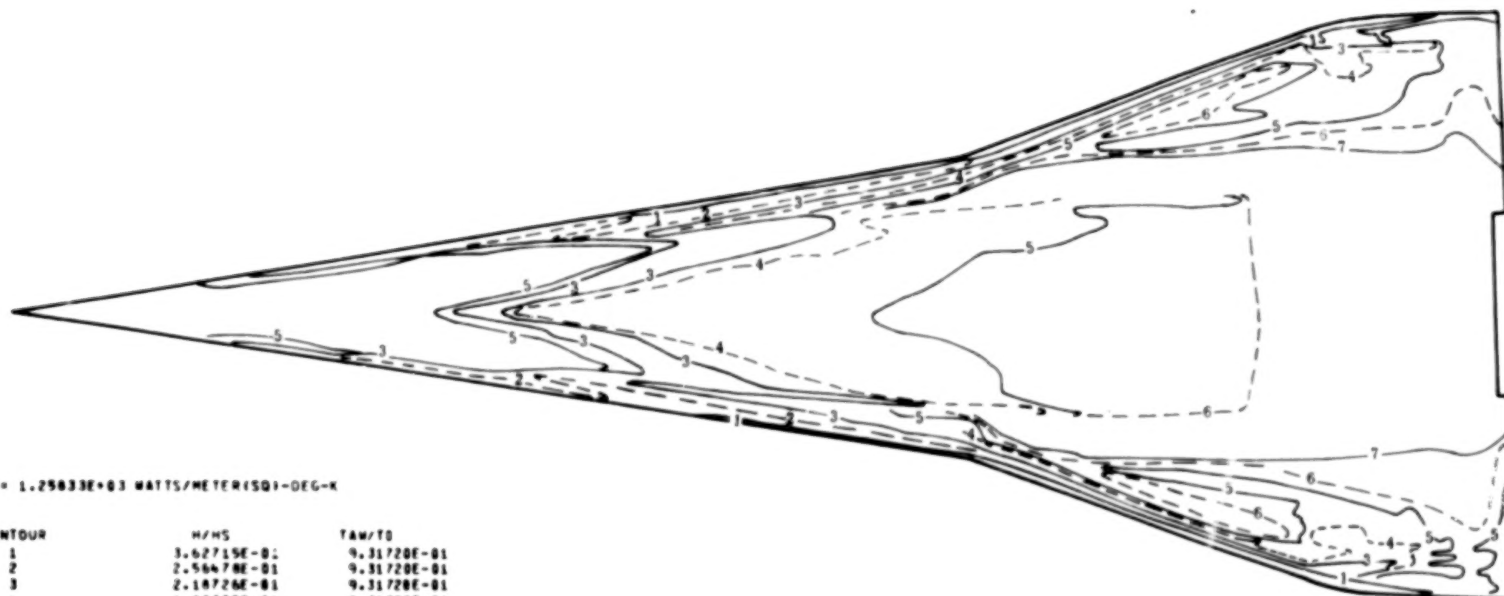
HS= 1.25633E+03 WATTS/METER(SQ)-DEG-K

| CONTOUR | H/HS | TAW/T0 |
|---------|------|--------|
| 1 | 3.62715E-01 | 9.31720E-01 |
| 2 | 2.56478E-01 | 9.31720E-01 |
| 3 | 2.18726E-01 | 9.31720E-01 |
| 4 | 1.87305E-01 | 9.31720E-01 |
| 5 | 1.66625E-01 | 9.31720E-01 |
| 6 | 1.45086E-01 | 9.31720E-01 |
| 7 | 1.35411E-01 | 9.31720E-01 |

(a)  $\alpha = 0.6^\circ$;  $T_{pc} = 381$ K.

Figure 8.- Contour-line drawings of model windward side at  $R_l = 15 \times 10^6$.

HS= 1.25712E+03 WATTS/METER(SQ)-DEG-K

| CONTOUR | H/HS | TAW/T8 |
|---|---|---|
| 1 | 4.6646E-01 | 9.33650E-01 |
| 2 | 3.5291E-01 | 9.33650E-01 |
| 3 | 5.04551E-01 | 9.33650E-01 |
| 4 | 2.6954E-01 | 9.33650E-01 |
| 5 | 2.2917E-01 | 9.33650E-01 |
| 6 | 2.0479E-01 | 9.33650E-01 |
| 7 | 1.8674E-01 | 9.33650E-01 |
| 8 | 1.4763E-01 | 9.33650E-01 |

(b)  $\alpha = 6.2°$;  $T_{pc} = 394$ K.

Figure 8.- Continued.

33

HS= 1.29519E+03 WATTS/METER-(SQ)-DEG-K

| CONTOUR | H/HS | TAW/TO |
|---|---|---|
| 1 | 7.9215E-01 | 9.3574E-01 |
| 2 | 5.6013E-01 | 9.3574E-01 |
| 3 | 3.9607E-01 | 9.3574E-01 |
| 4 | 3.2399E-01 | 9.3574E-01 |
| 5 | 2.8027E-01 | 9.3574E-01 |
| 6 | 2.6116E-01 | 9.3574E-01 |
| 7 | 2.2867E-01 | 9.3574E-01 |
| 8 | 1.9901E-01 | 9.3574E-01 |
| 9 | 1.6868E-01 | 9.3574E-01 |
| 10 | 1.4033E-01 | 9.3574E-01 |

(c)  $\alpha$ = 11.9°;  $T_{pc}$ = 367 K.

Figure 8.- Continued.

HS= 1.23532E+03 WATTS/METER(SQ)-DEG-K

| CONTOUR | H/HS | TAW/TO |
|---|---|---|
| 1 | 1.49253E+00 | 9.40100E-01 |
| 2 | 8.61710E-01 | 9.40100E-01 |
| 3 | 6.67478E-01 | 9.40100E-01 |
| 4 | 6.09321E-01 | 9.40100E-01 |
| 5 | 5.64122E-01 | 9.40100E-01 |
| 6 | 4.71978E-01 | 9.40100E-01 |
| 7 | 3.51792E-01 | 9.40100E-01 |
| 8 | 3.33739E-01 | 9.40100E-01 |

(d)  $\alpha = 17.6^{o}$;  $T_{pc} = 394$ K.

Figure 8.- Continued.

35
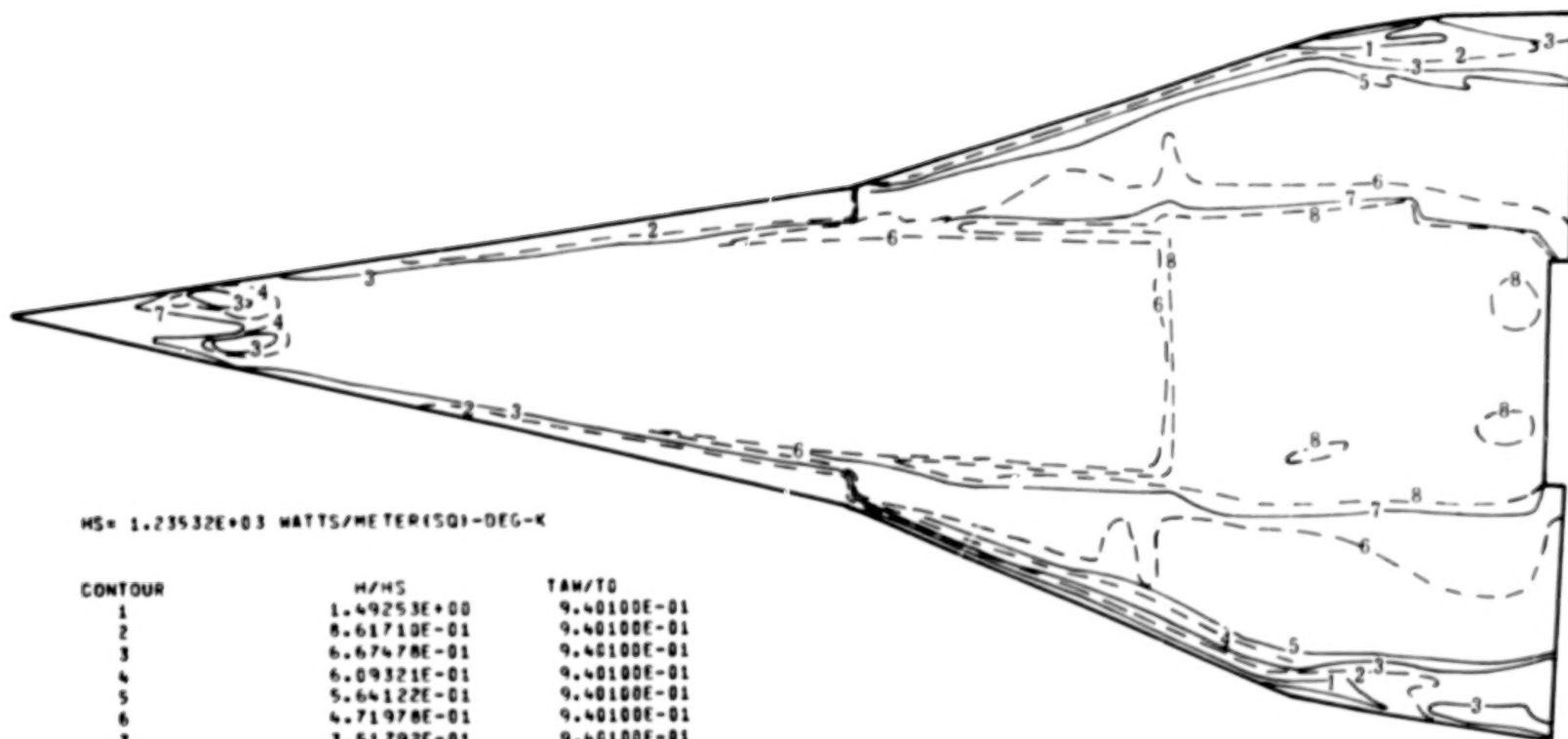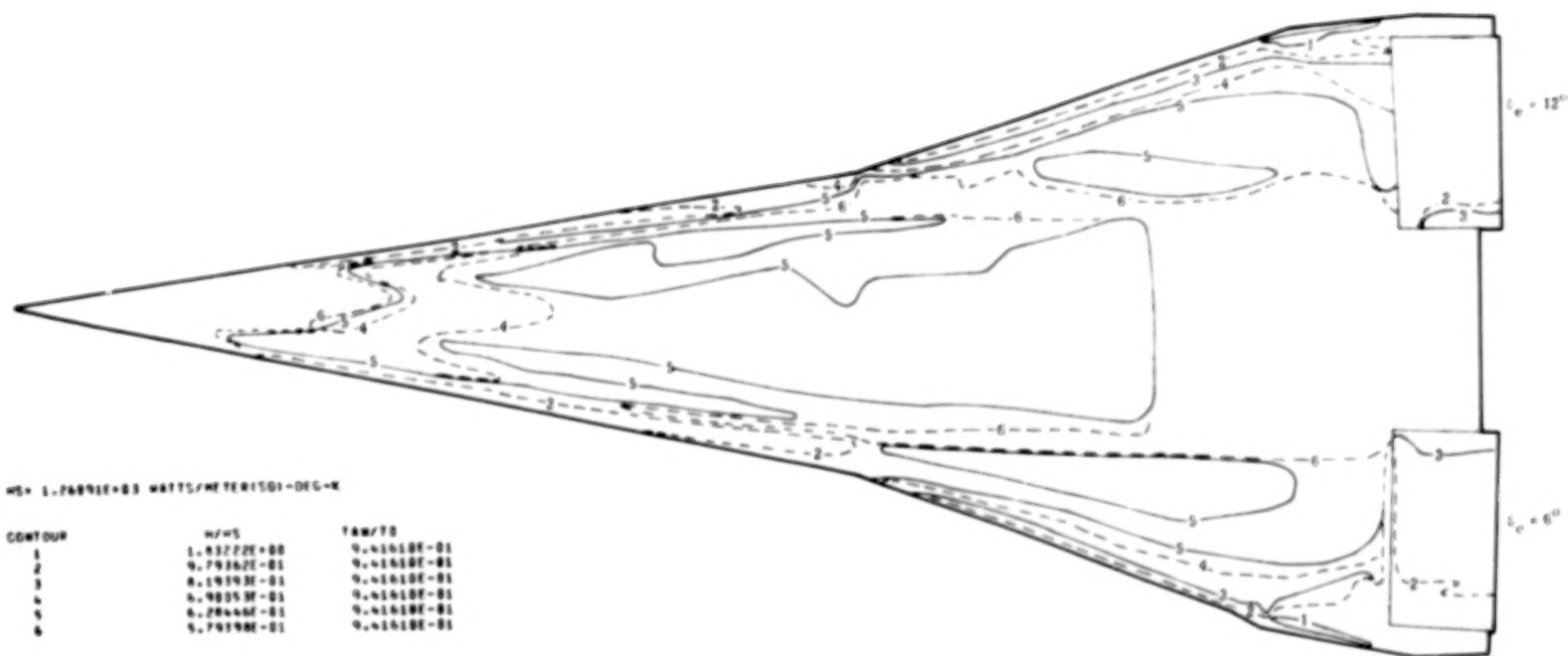
(e)  $\alpha = 24°$;  $T_{pc} = 450$ K.

Figure 8.- Concluded.

HS= 7.02468E+02 WATTS/METER(SQ)-DEG-K

| CONTOUR | H/HS | TAW/TO |
|---------|------|--------|
| 1 | 1.30544E-01 | 9.33520E-01 |
| 2 | 1.03204E-01 | 9.33520E-01 |
| 3 | 8.42656E-02 | 9.33520E-01 |
| 4 | 7.07972E-02 | 9.33520E-01 |
| 5 | 6.08663E-02 | 9.33520E-01 |
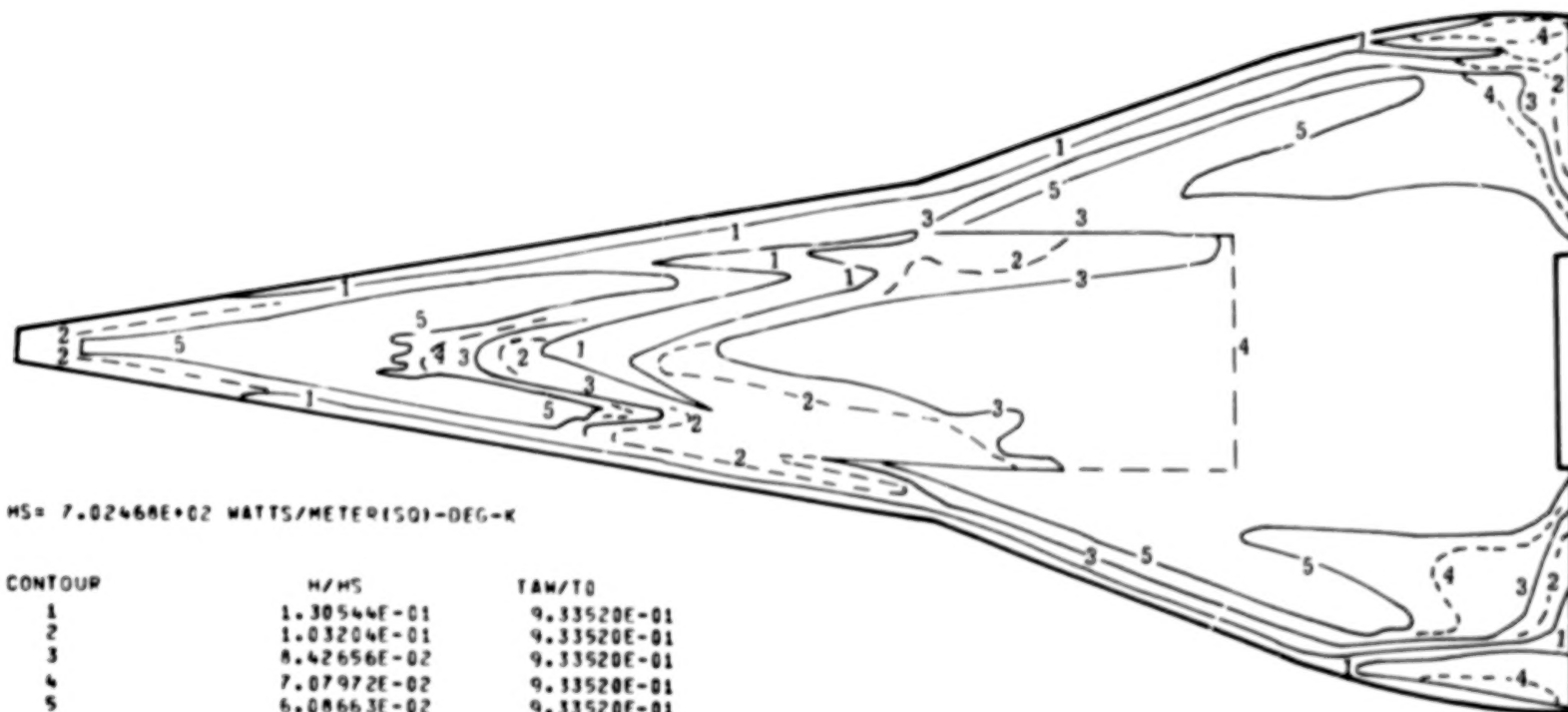
(a)  $\alpha = 0.6°$;  $T_{pc} = 313$ K.

Figure 9.- Contour-line drawings of model windward side at  $R_l = 5 \times 10^6$.
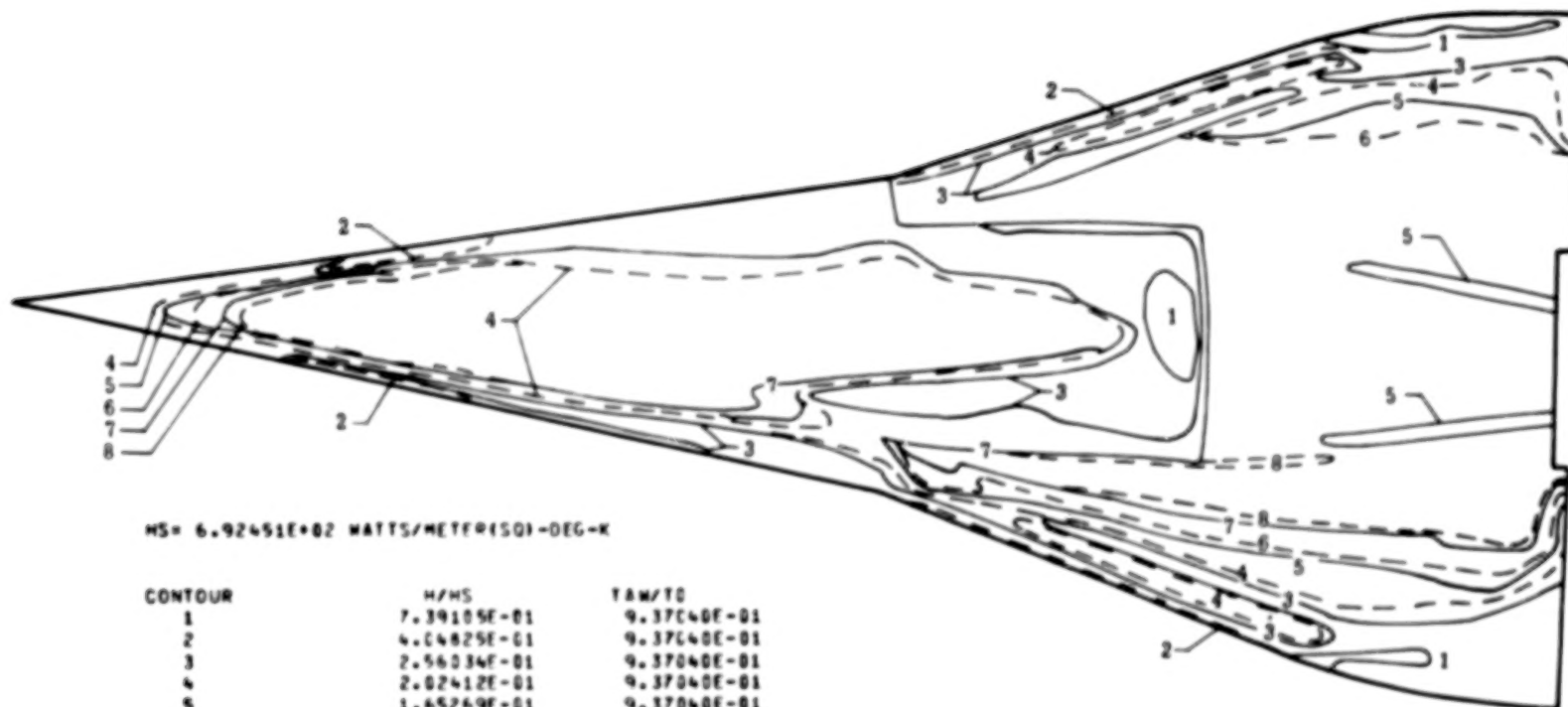
HS= 6.92451E+02 WATTS/METER(SQ)-DEG-K

| CONTOUR | H/HS | TAW/T0 |
|---------|------|--------|
| 1 | 7.39105E-01 | 9.37040E-01 |
| 2 | 4.04825E-01 | 9.37040E-01 |
| 3 | 2.56034E-01 | 9.37040E-01 |
| 4 | 2.02412E-01 | 9.37040E-01 |
| 5 | 1.65269E-01 | 9.37040E-01 |
| 6 | 1.47921E-01 | 9.37040E-01 |
| 7 | 1.28017E-01 | 9.37040E-01 |
| 8 | 1.22059E-01 | 9.37040E-01 |

(b)  $\alpha = 11.9°$;  $T_{pc} = 325$ K.

Figure 9.- Continued.
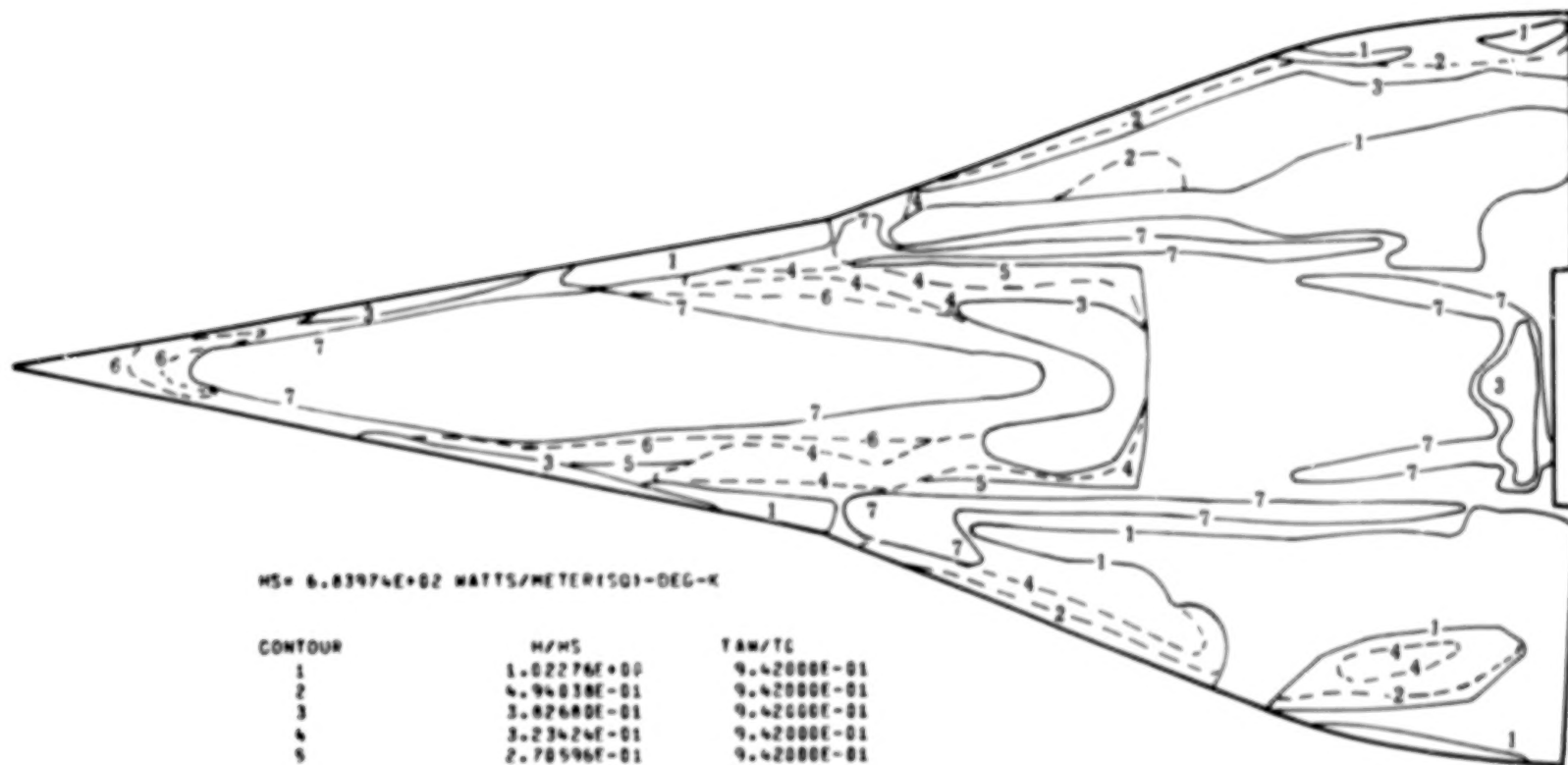
HS= 6.83974E+02 WATTS/METER(SQ)-DEG-K

| CONTOUR | H/HS | TAW/TC |
|---------|------|--------|
| 1 | 1.02276E+00 | 9.42000E-01 |
| 2 | 4.94038E-01 | 9.42000E-01 |
| 3 | 3.82680E-01 | 9.42000E-01 |
| 4 | 3.23424E-01 | 9.42000E-01 |
| 5 | 2.78596E-01 | 9.42000E-01 |
| 6 | 2.28940E-01 | 9.42000E-01 |
| 7 | 1.91340E-01 | 9.42000E-01 |

(c)  $\alpha = 24°$;  $T_{pc} = 339$ K.

Figure 9.- Concluded.

$\delta_e = 12°$

$\delta_e = 6°$

(a) $\alpha = 6.2°$.
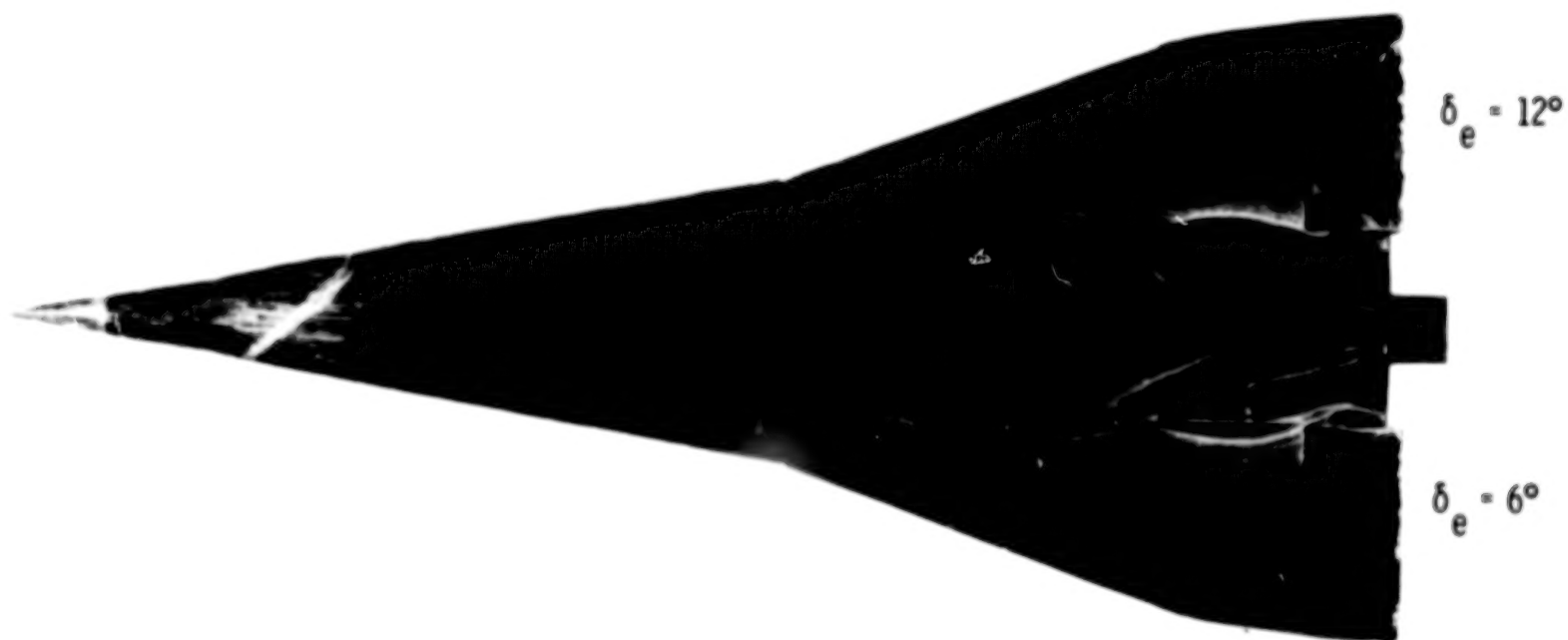
Figure 10.- Oil-flow photographs of model windward side. $R_l = 15 \times 10^6$.

$\delta_e = 12°$

$\delta_e = 6°$
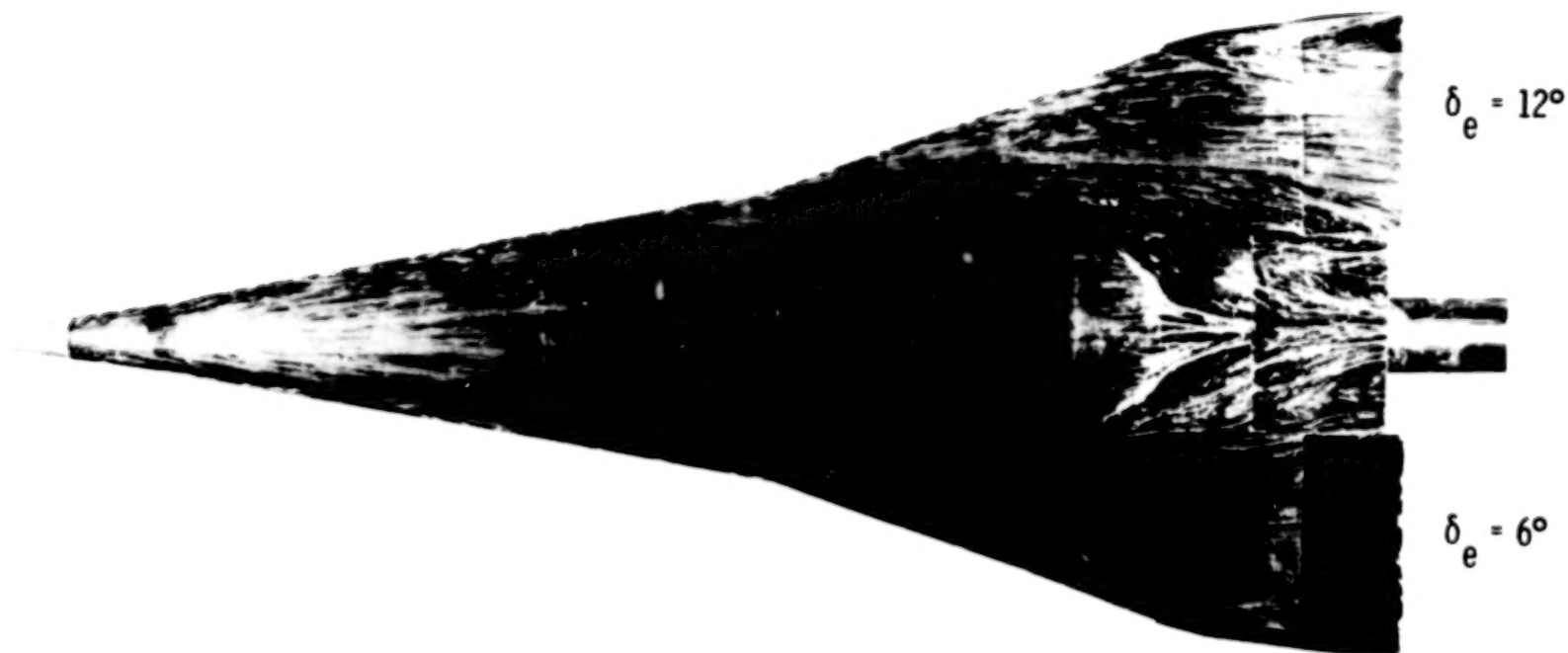
(b) $\alpha = 11.9°$.

L-78-10

Figure 10.- Continued.

Missing tip fin

$\delta_e = 12°$

$\delta_e = 6°$

(c)  $\alpha = 17.6°$.
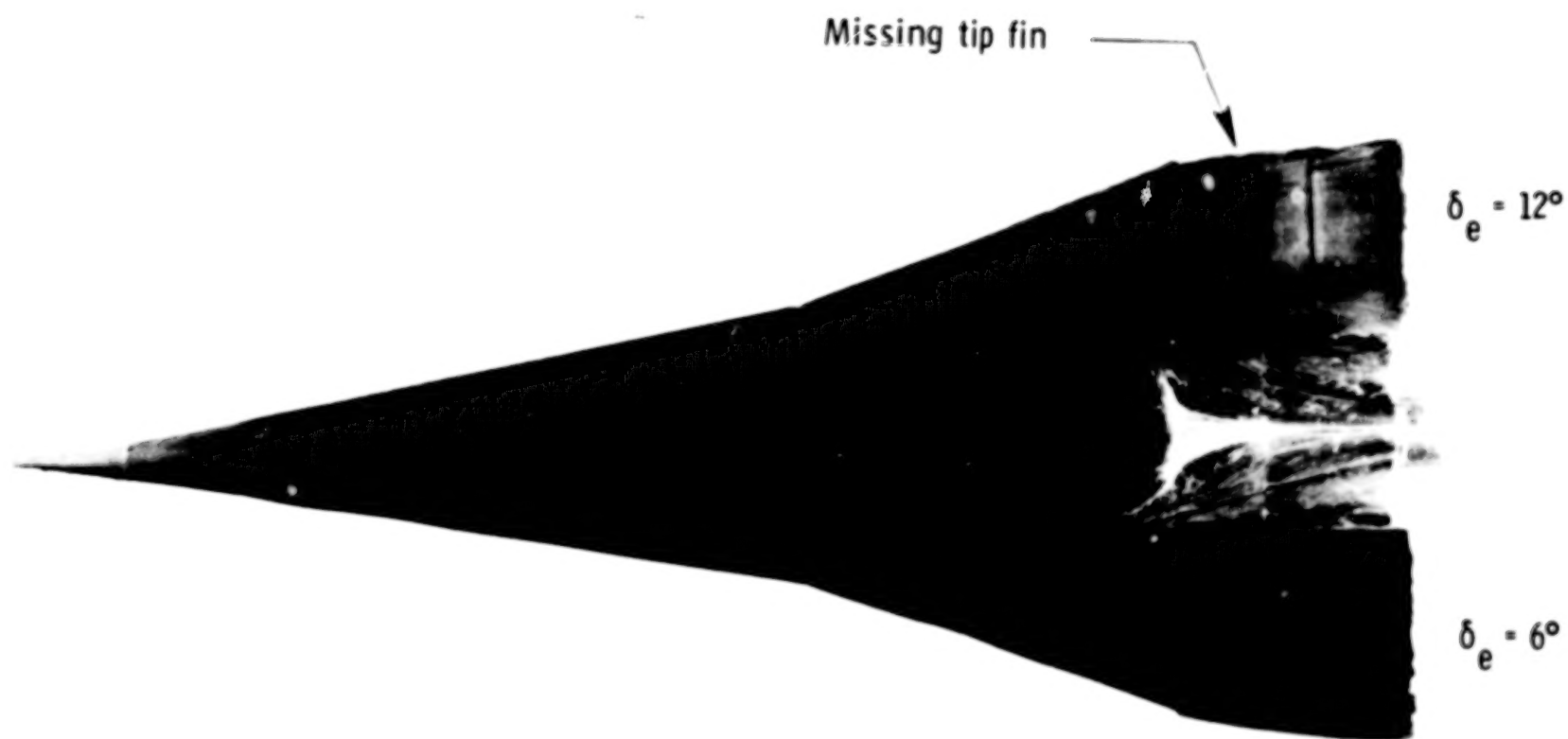
Figure 10.- Concluded.

L-78-11

$\delta_e = 12^o$

$\delta_e = 6^o$

HS= 1.29568E+03 WATTS/METER(SQ)-DEG-K

| CONTOUR | H/HS | TAW/TS |
|---|---|---|
| 1 | 6.4129E-01 | 9.3259E-01 |
| 2 | 3.6663E-01 | 9.3254E-01 |
| 3 | 2.7237E-01 | 9.3259E-01 |
| 4 | 1.9866E-01 | 9.3219E-01 |
| 5 | 1.7221E-01 | 9.3259E-01 |
| 6 | 1.4822E-01 | 9.3259E-01 |
| 7 | 1.3615E-01 | 9.3269E-01 |
| 8 | 1.2494E-01 | 9.3340E-01 |
| 9 | 1.1836E-01 | 9.3294E-01 |
| 10 | 1.1401E-01 | 9.3299E-01 |
| 11 | 1.1116E-01 | 9.3299E-01 |
| 12 | 1.0148E-01 | 9.3299E-01 |
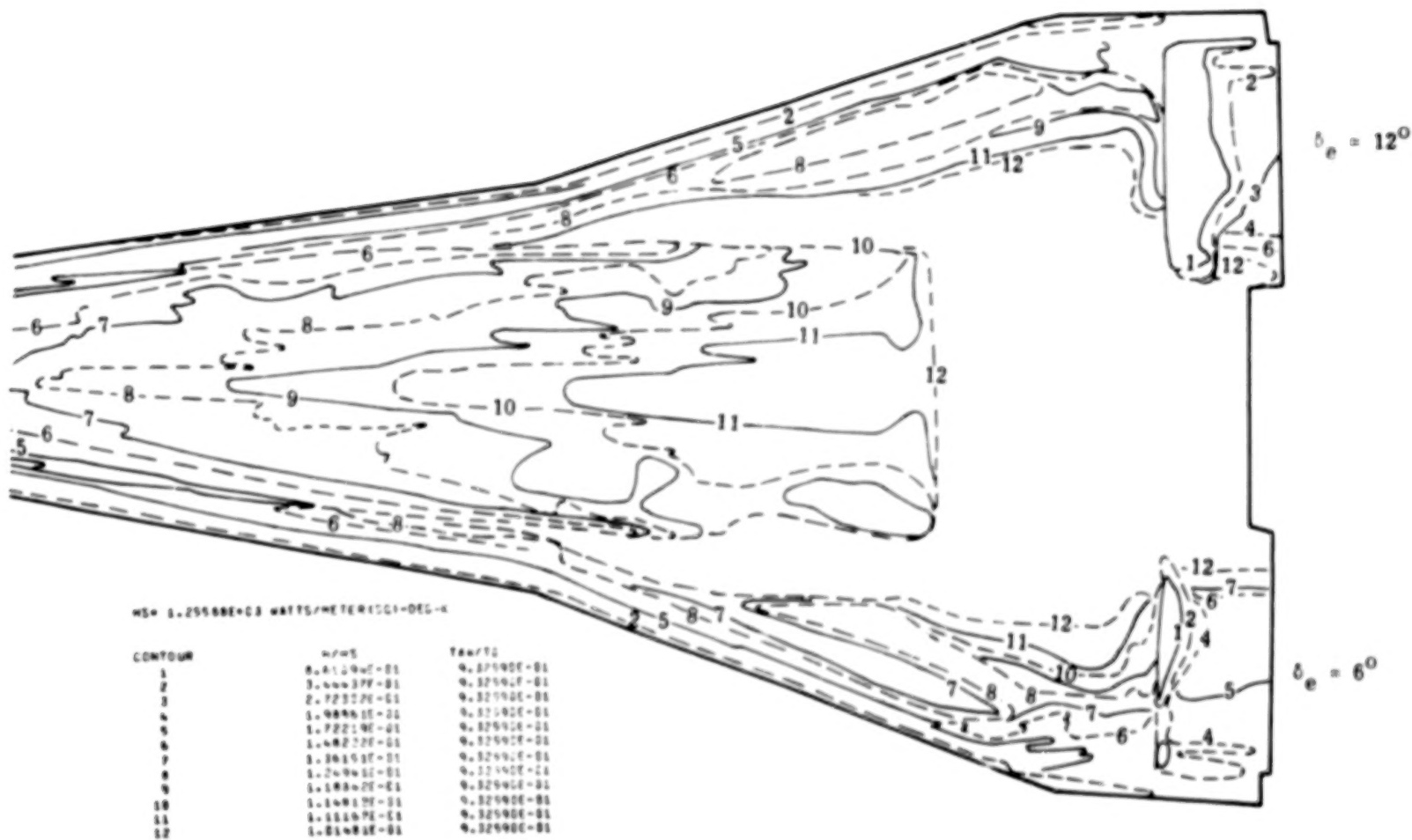
(a) $\alpha = 0.6^o$; $T_{pc} = 367$ K.

Figure 11.- Contour-line drawings of model windward side with $6^o$ and $12^o$ positively deflected elevons.

HS= 1.25712E+03 WATTS/METER(SQ)-DEG-K

| CONTOUR | H/HS | TAW/T0 |
|---------|------|--------|
| 1 | 4.66868E-01 | 9.33650E-01 |
| 2 | 3.52919E-01 | 9.33650E-01 |
| 3 | 3.04551E-01 | 9.33650E-01 |
| 4 | 2.69547E-01 | 9.33650E-01 |
| 5 | 2.29177E-01 | 9.33650E-01 |
| 6 | 2.08790E-01 | 9.33650E-01 |
| 7 | 1.86767E-01 | 9.33650E-01 |
| 8 | 1.47637E-01 | 9.33650E-01 |

$\delta_e = 12°$

$\delta_e = 6°$
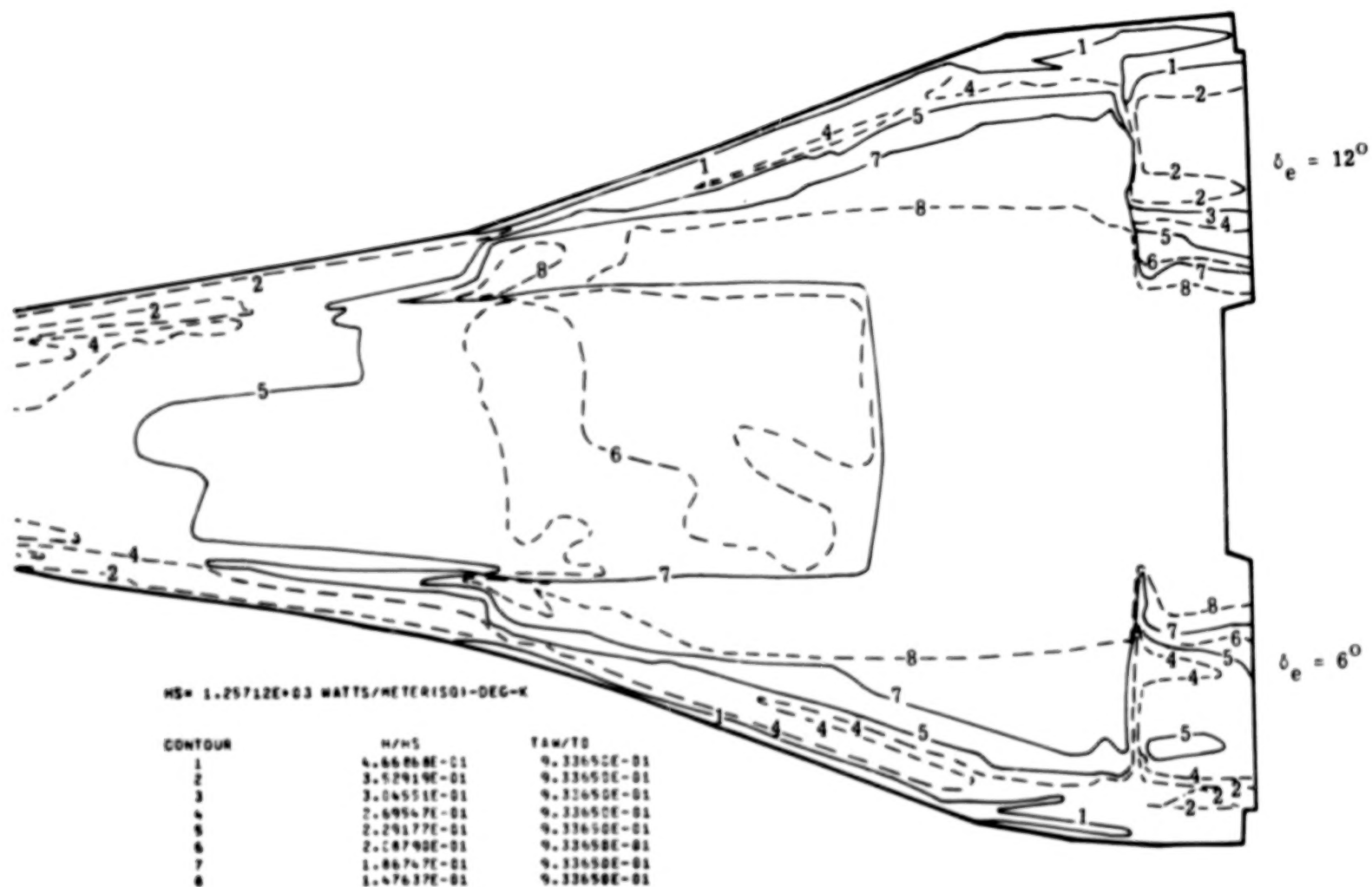
(b)  $\alpha = 6.2°$;  $T_{pc} = 394$ K.

Figure 11.- Continued.

47

$\delta_e = 12^O$

$\delta_e = 6^O$

HS= 1.25513E+03 WATTS/METER+(SQ)-DEG-K

| CONTOUR | H/-S | TAW/TO |
|---|---|---|
| 1 | 7.9215 7E-01 | 9.357=CE-01 |
| 2 | 5.69139E-01 | 9.357=2E-01 |
| 3 | 3.9637 8E-01 | 9.3574 3E-31 |
| 4 | 3.2394 7E-01 | 9.357=2E-01 |
| 5 | 2.803 7CE-01 | 9.3574 3E-01 |
| 6 | 2.61166F-01 | 9.3574 CE-C1 |
| 7 | 2.28676E-01 | 9.757=0E-01 |
| 8 | 1.99039F-01 | 9.357=0E-01 |
| 9 | 1.68998E-01 | 9.3574 0E-01 |
| 10 | 1.400 39E-01 | 9.3574 0E-01 |

(c) $\alpha = 11.9^O$; $T_{pc} = 367$ K.

Figure 11.- Continued.

HS= 1.26062E+03 WATTS/METER(SQ)-DEG-K

| CONTOUR | H/HS | TAW/TO |
|---|---|---|
| 1 | 1.12959E+00 | 9.38200E-01 |
| 2 | 7.98742E-01 | 9.38200E-01 |
| 3 | 7.00543E-01 | 9.38200E-01 |
| 4 | 5.95347E-01 | 9.38200E-01 |
| 5 | 5.05169E-01 | 9.38200E-01 |

$\delta_e = 12^0$

$\delta_e = 6^0$

(d)  $\alpha = 17.6^0$;  $T_{pc} = 450$ K.

Figure 11.- Continued.

$\delta_e = 12^O$

$\delta_e = 6^O$

HS= 1.25663E+03 WATTS/METER(SQ)-DEG-K

| CONTOUR | H/HS | TAW/TO |
|---------|------|--------|
| 1 | 1.20215E+00 | 9.41650E-01 |
| 2 | 8.96028E-01 | 9.41650E-01 |
| 3 | 7.24922E-01 | 9.41650E-01 |
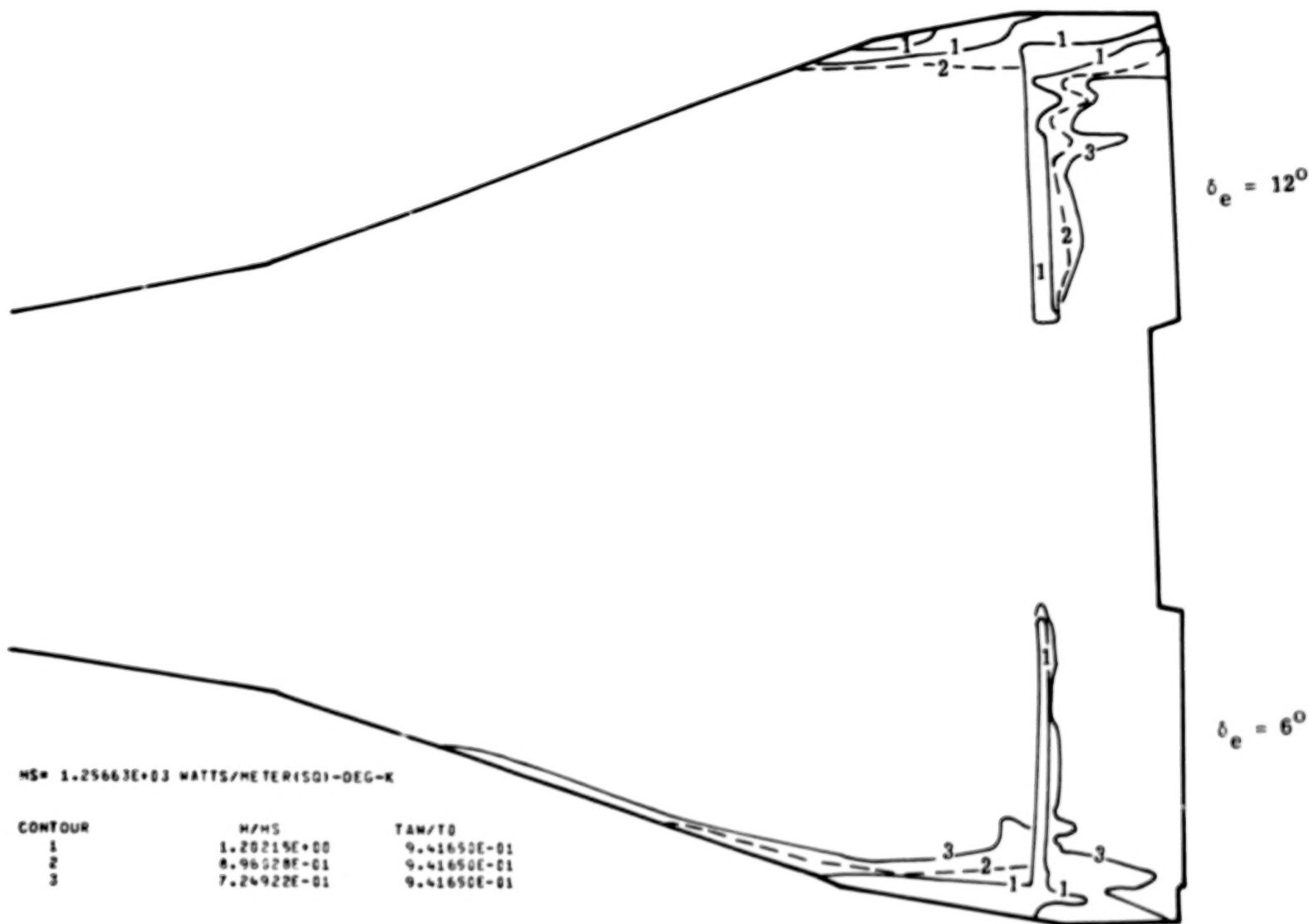
(e)  $\alpha = 24^O$;  $T_{pc} = 464$ K.

Figure 11.- Concluded.

Wing-strake juncture
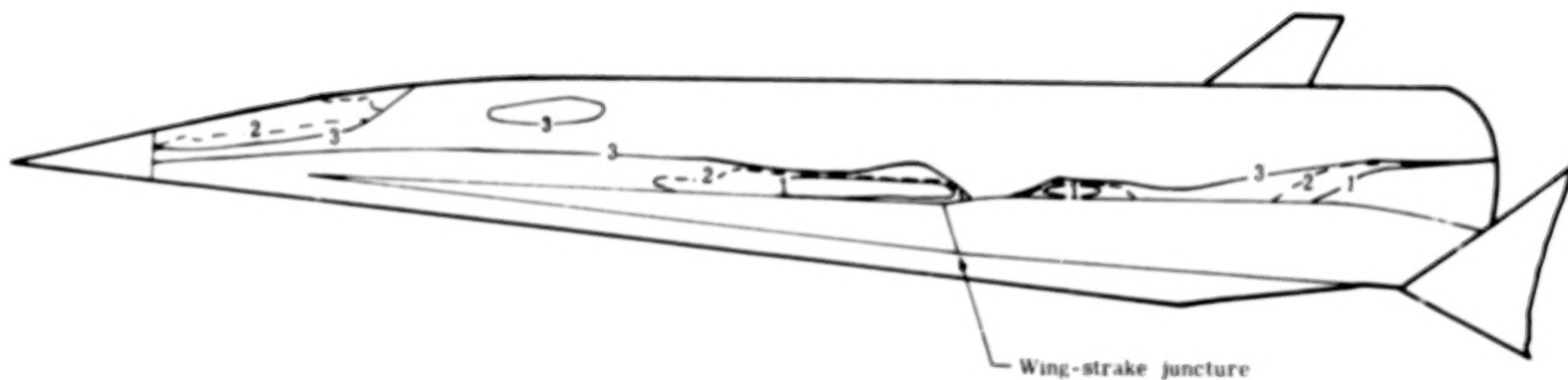
HS= 1.21725E+03 WATTS/METER(SQ)-DEG-K

| CONTOUR | H/HS | TAW/TC |
|---------|------|--------|
| 1 | 6.77505E-01 | 9.30000E-01 |
| 2 | 2.14246E-01 | 9.30000E-01 |
| 3 | 1.51443E-01 | 9.30000E-01 |

(a) $\alpha = 0.6^o$; $T_{pc} = 325$ K.

Figure 12.- Contour-line drawings of model side at $R_l = 15 \times 10^6$.

Wing-strake juncture
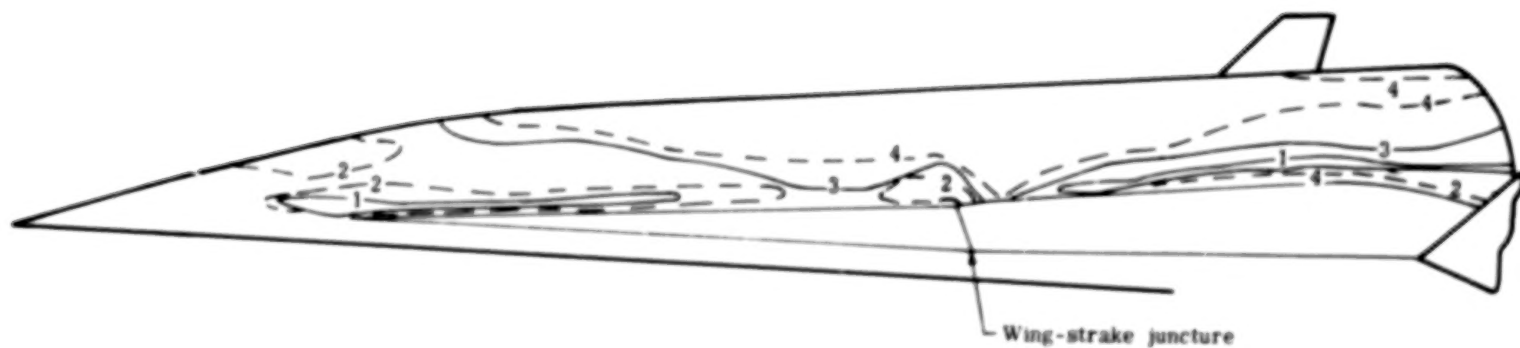
HS= 1.24031E+03 WATTS/METER(SQ)-DEG-K

| CONTOUR | H/HS | TAW/T0 |
|---------|-------------|-------------|
| 1 | 1.97423E-01 | 9.30000E-01 |
| 2 | 1.39599E-01 | 9.30000E-01 |
| 3 | 4.829C8E-02 | 9.30000E-01 |
| 4 | 6.97996E-02 | 9.30000E-01 |

(b)  $\alpha = 6.2°$;  $T_{pc} = 339$ K.

Figure 12.- Continued.
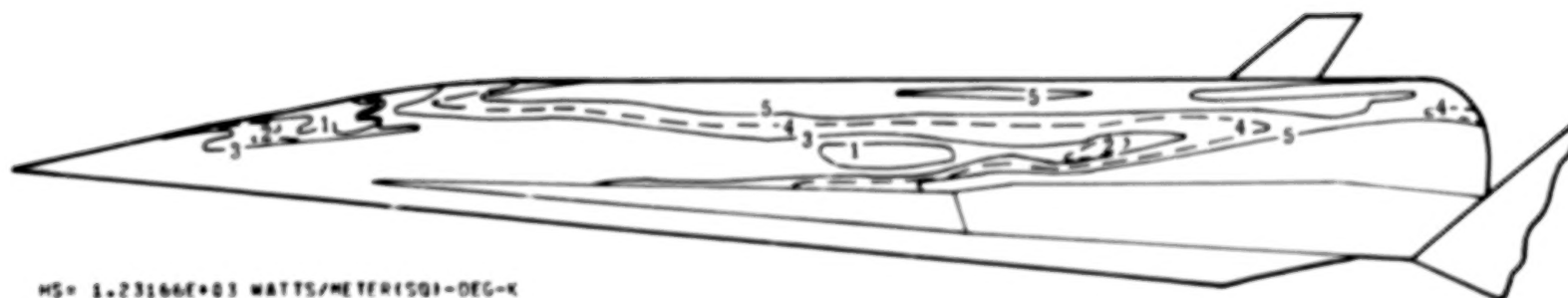
HS= 1.23166E+03 WATTS/METER(SQ)-DEG-K

| CONTOUR | H/HS | TAW/TJ |
|---------|------------|------------|
| 1 | 6.53950E-02 | 9.30000E-01 |
| 2 | 5.33948E-02 | 9.30000E-01 |
| 3 | 4.62412E-02 | 9.30000E-01 |
| 4 | 3.17212E-02 | 9.30000E-01 |
| 5 | 2.30789E-02 | 9.30000E-01 |

(c)   $\alpha = 11.9°$;   $T_{pc} = 313$ K.

Figure 12.- Concluded.

(a) $\alpha = 6.2^o$.
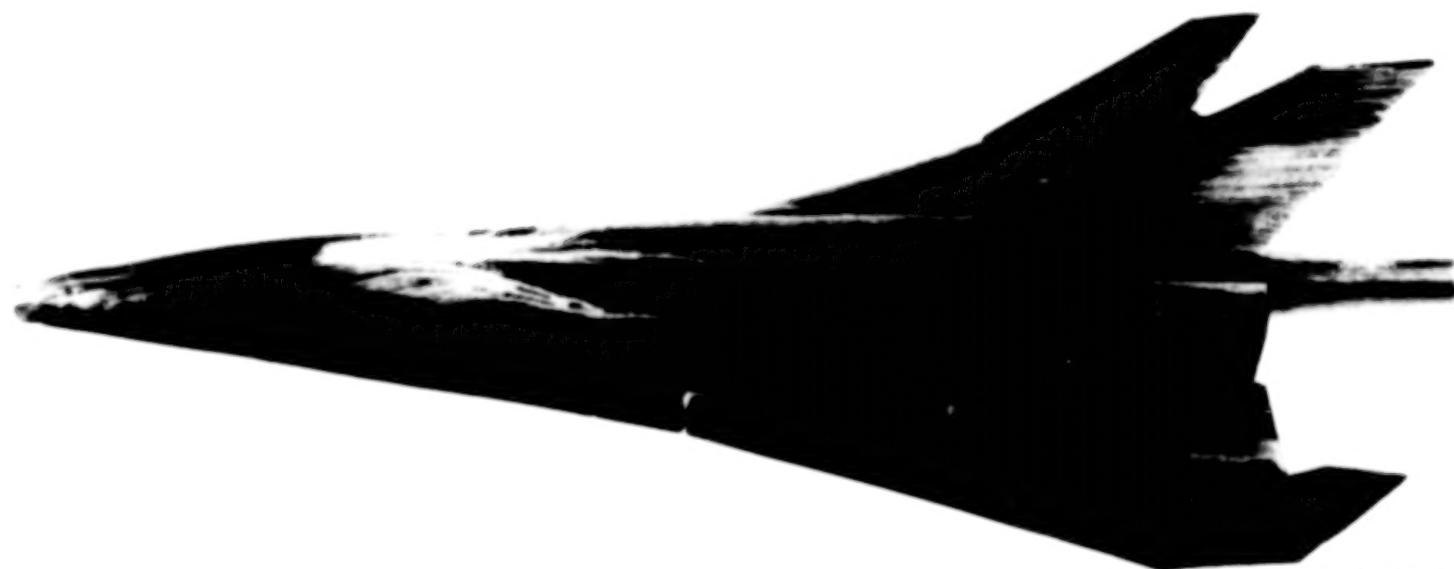
Figure 13.- Oil-flow photographs of model side. $R_l \approx 15 \times 10^6$.

(b) $\alpha = 11.9^{\circ}$.

Figure 13.- Concluded.
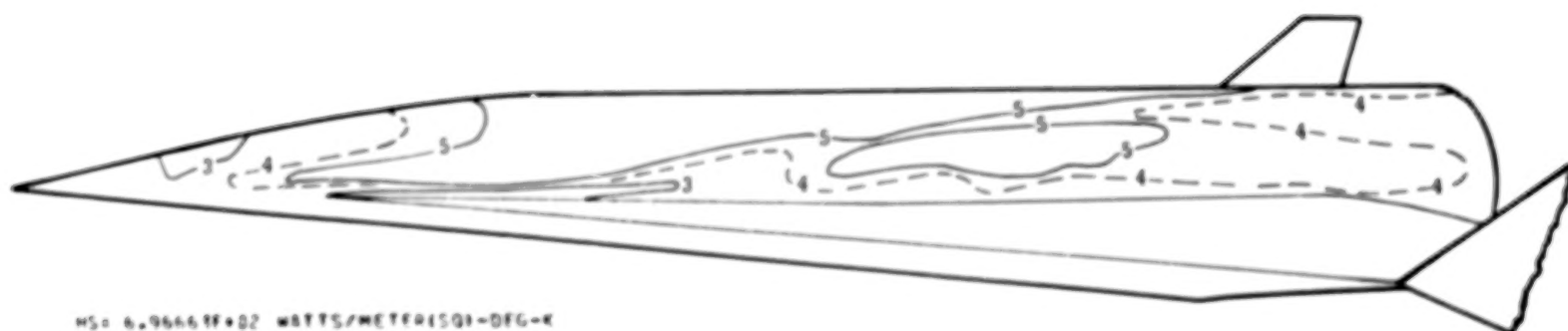
L-78-13

HS= 6.96669E+02 WATTS/METER(SQ)-DEG-K

(a)  $\alpha = 0.6°$;  $T_{pc} = 313$ K.

Figure 14.- Contour-line drawings of model side at  $R_l = 5 \times 10^6$.
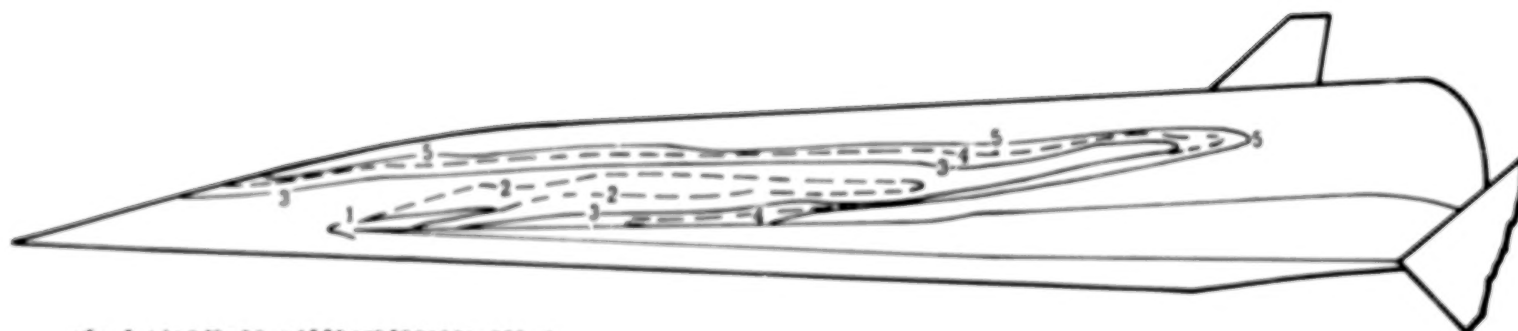
| CONTOUR | H/HS | TAW/TO |
|---|---|---|
| 1 | 8.95649E-02 | 9.30300E-01 |
| 2 | 4.60292E-02 | 9.30000E-01 |
| 3 | 2.31129E-02 | 9.30030E-01 |
| 4 | 2.13965E-02 | 9.30010E-01 |
| 5 | 1.79016E-02 | 9.30060E-01 |

(b) $\alpha = 11.9°$; $T_{pc} = 313$ K.

Figure 14.- Continued.
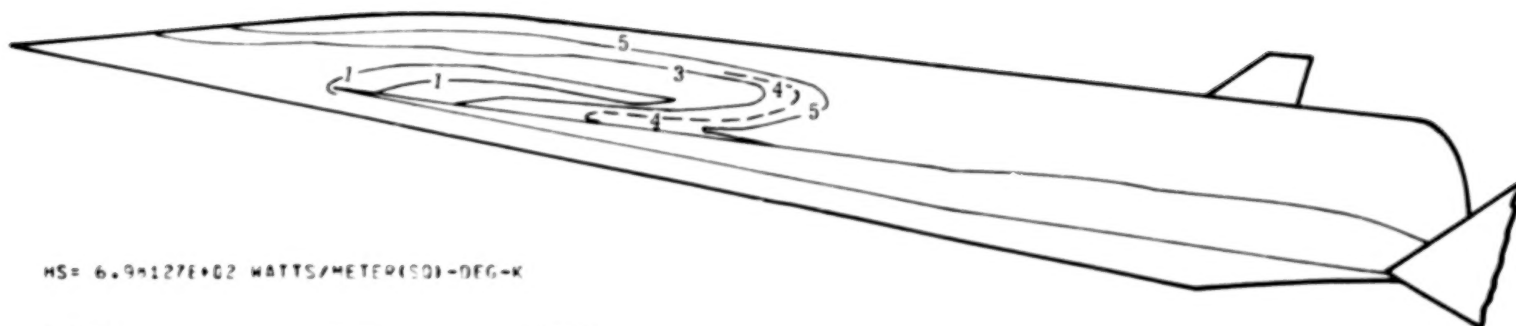
HS= 6.94127E+02 WATTS/METER(SQ)-DEG-K

| CONTOUR | H/HS | TAW/T0 |
|---|---|---|
| 1 | 8.1528lE-02 | 9.30000E-01 |
| 2 | 5.82113E-02 | 9.30000E-01 |
| 3 | 4.82327E-02 | 9.30000E-01 |
| 4 | 3.93918E-02 | 9.30000E-01 |
| 5 | 3.21551E-02 | 9.30000E-01 |

(c)  $\alpha = 24°$;  $T_{pc} = 313$ K.

Figure 14.- Concluded.

(a) $\alpha = 0.6^{\circ}$.
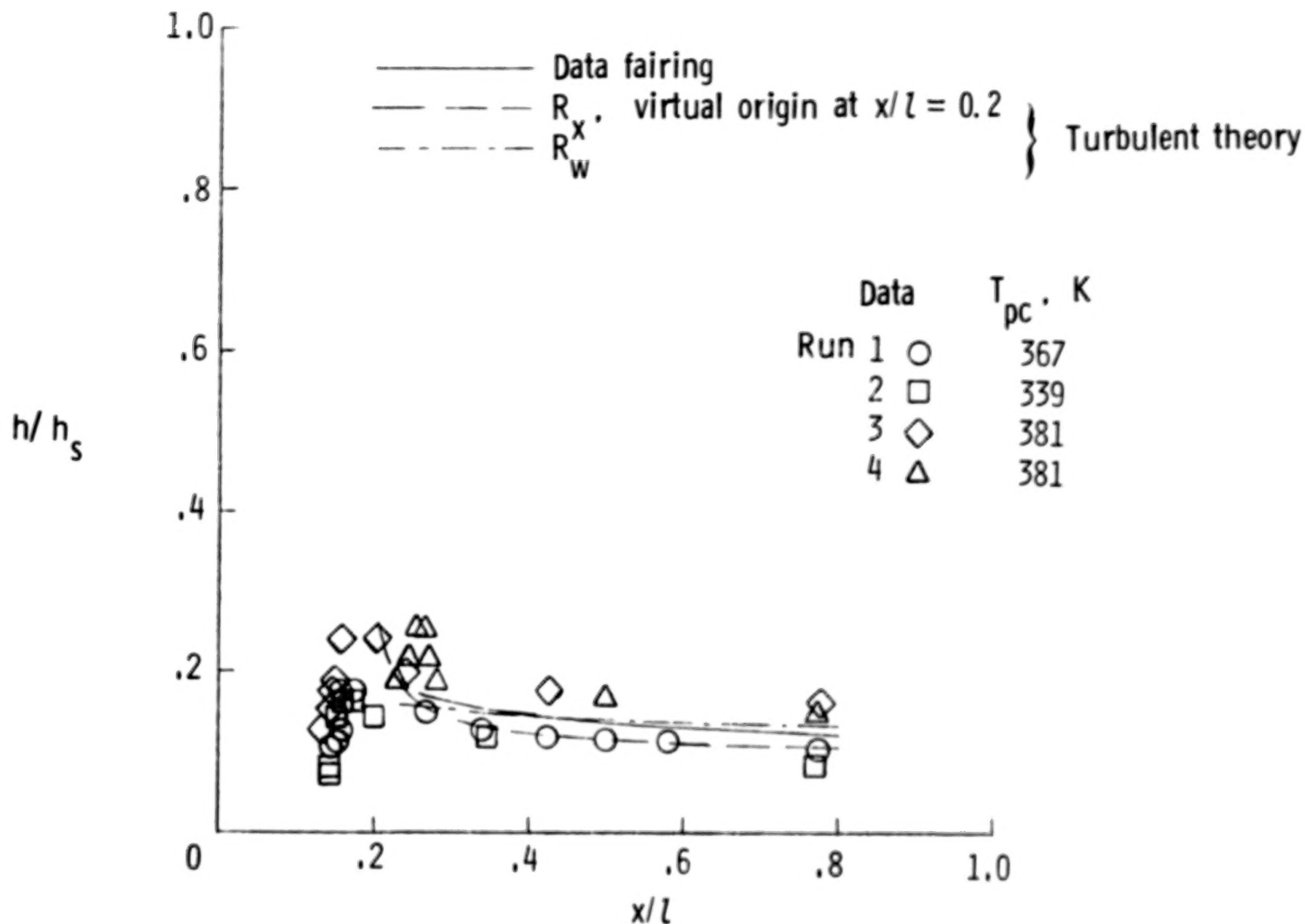
Figure 15.- Heat-transfer coefficient as a function of axial location on windward fuselage center line. $R_l \simeq 15 \times 10^6$; $\delta = 6^{\circ}$.
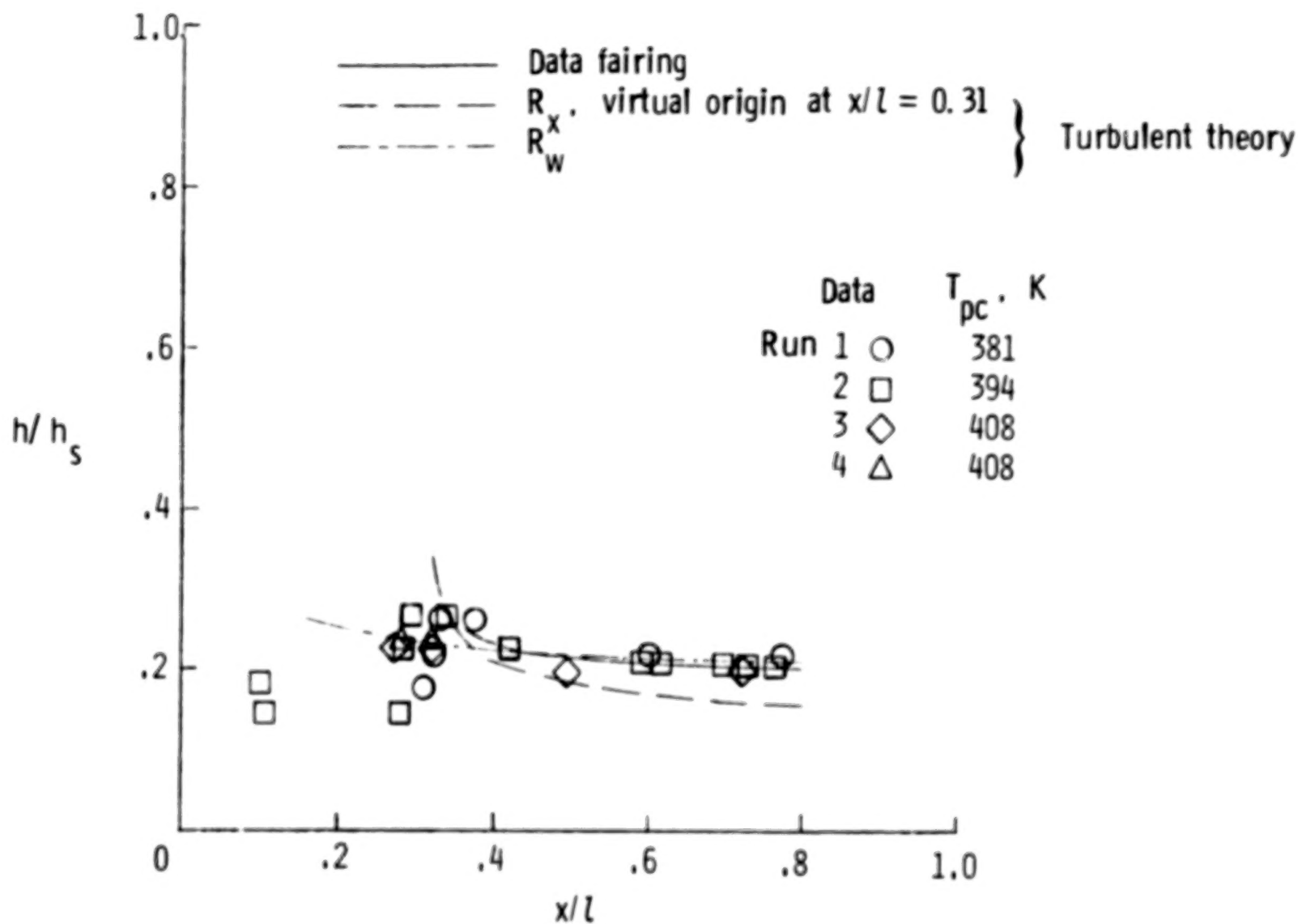
(b) $\alpha = 6.2°$.

Figure 15.- Continued.
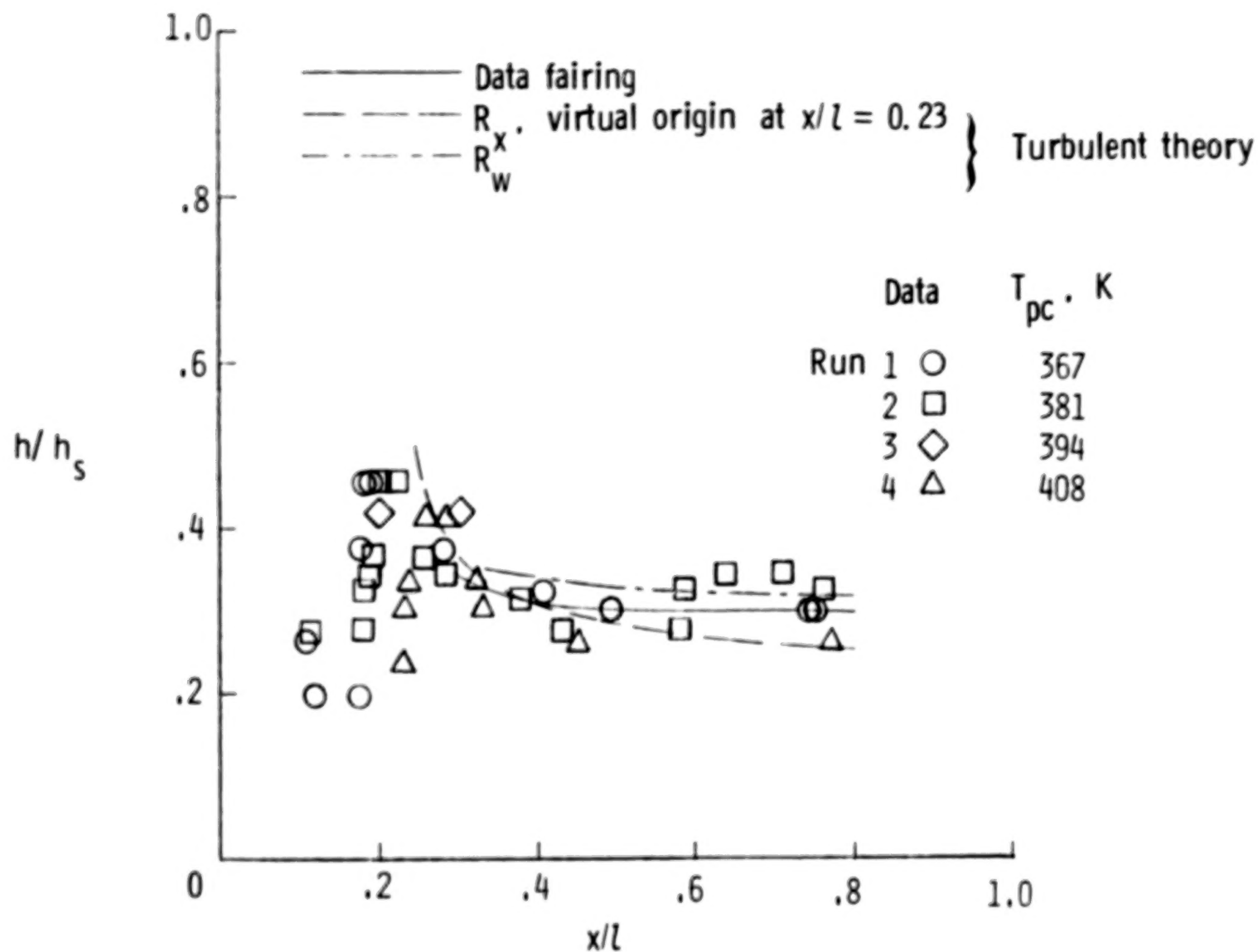
(c) $\alpha = 11.9°$.

Figure 15.- Continued.
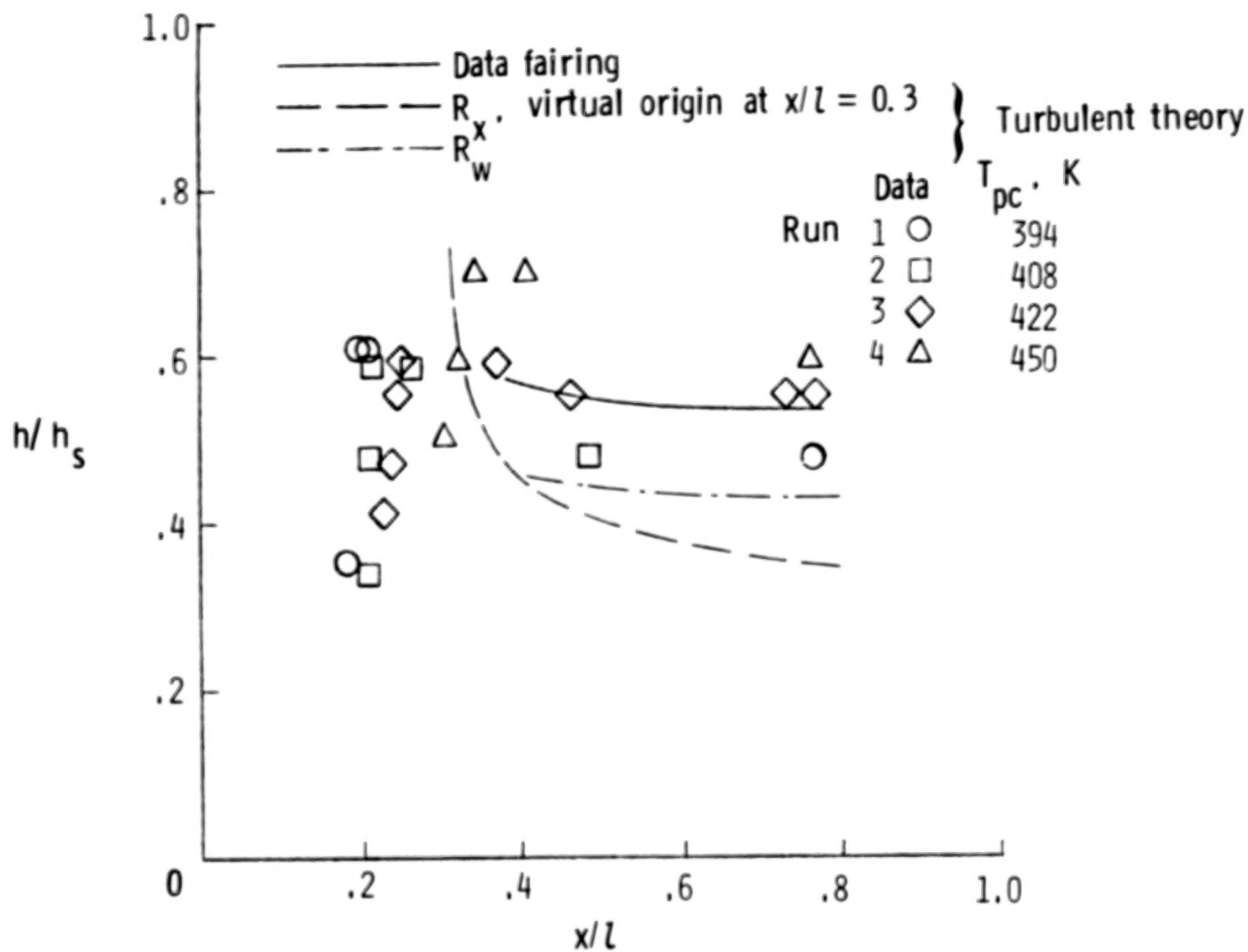
(d) $\alpha = 17.6°$.

Figure 15.- Continued.
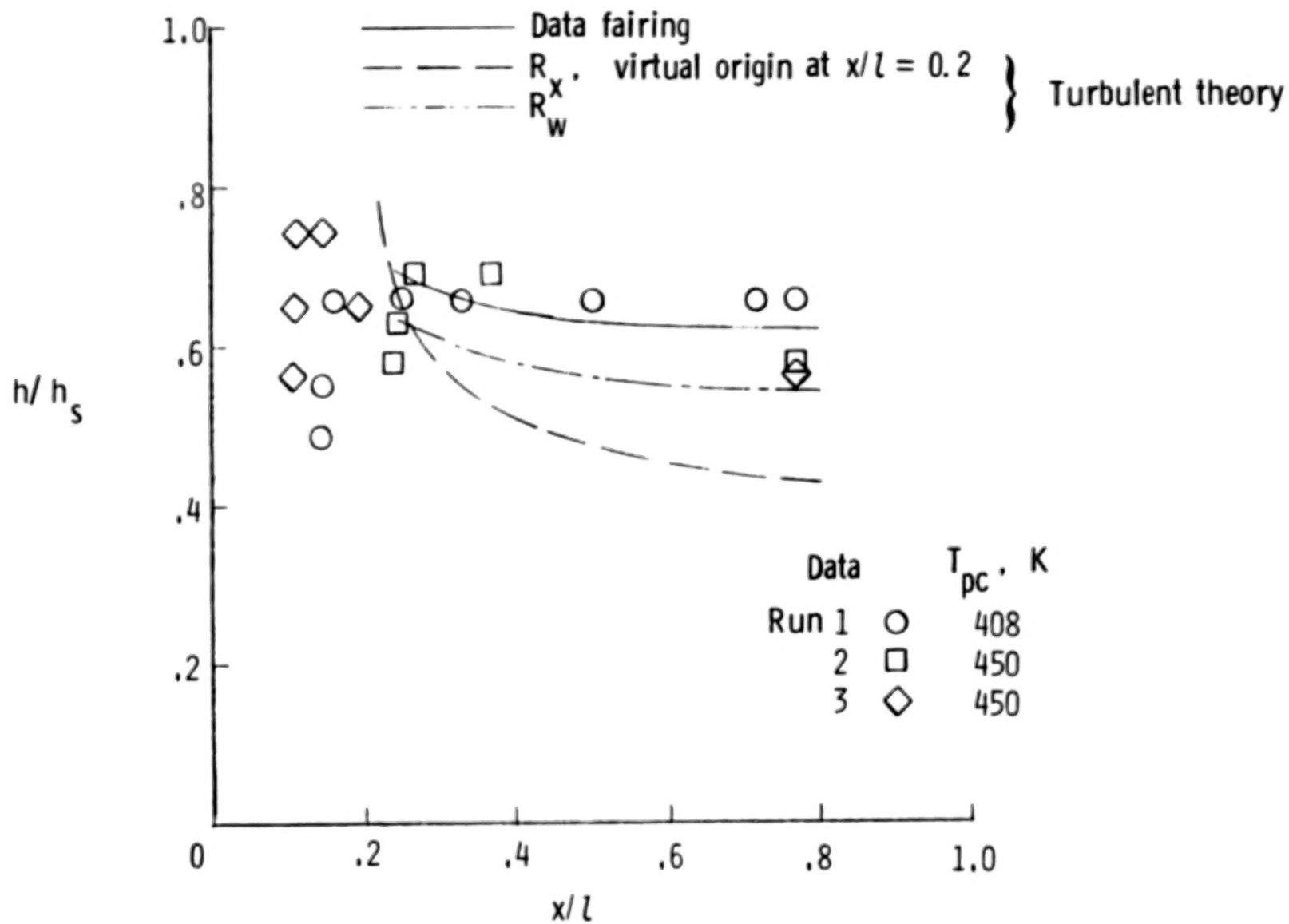
(e) $\alpha = 24°$.

Figure 15.- Concluded.
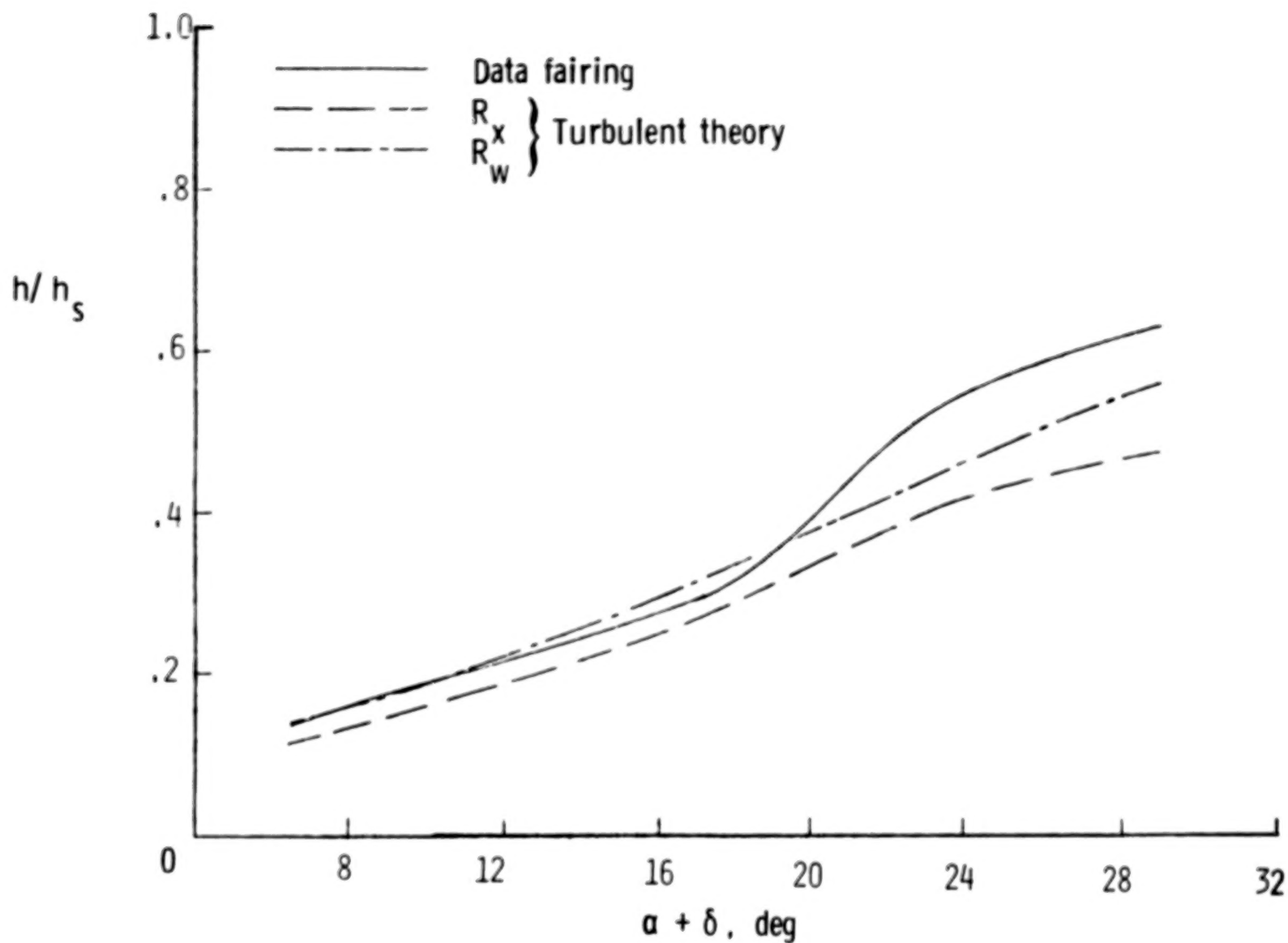
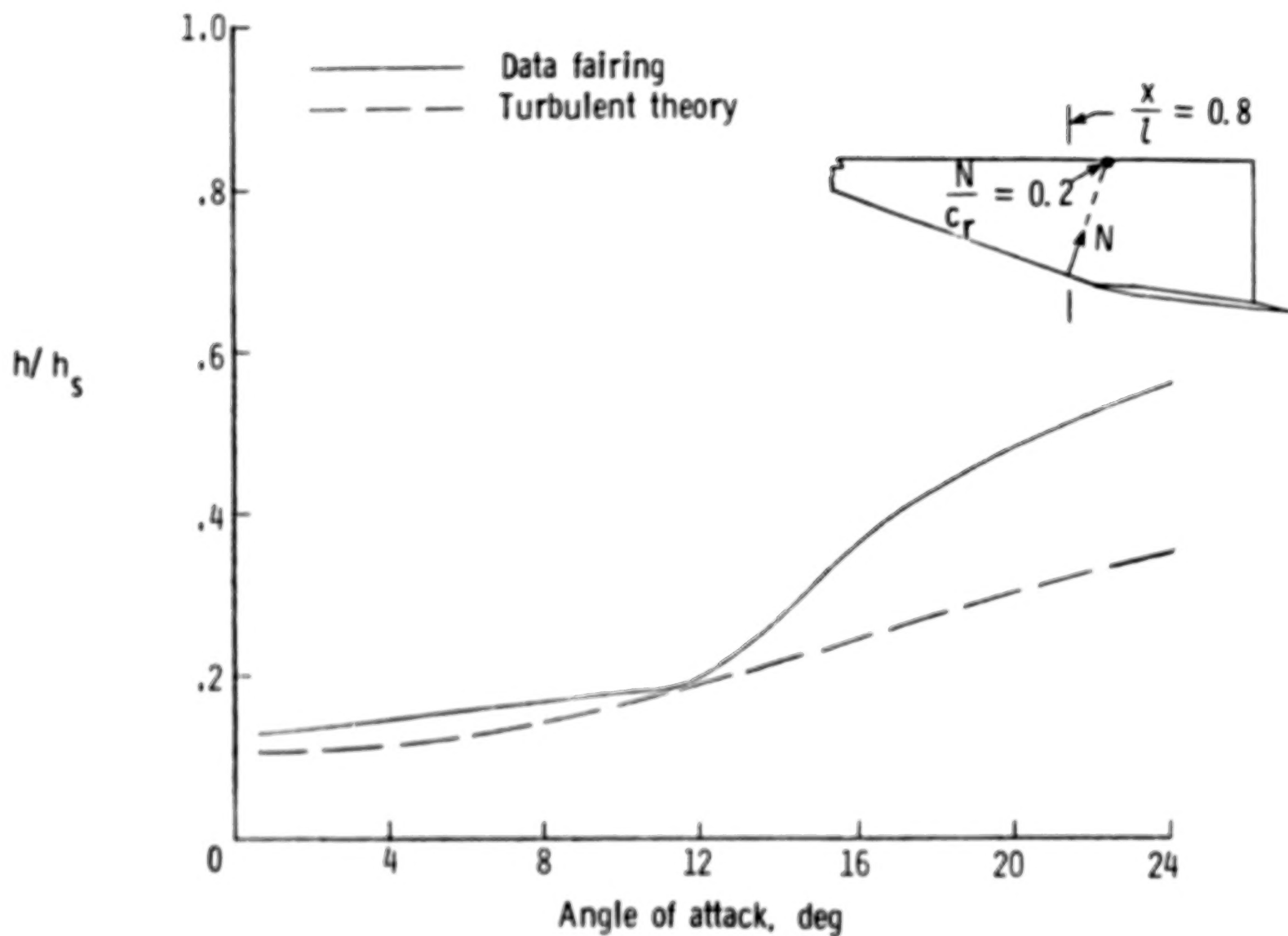Figure 16.- Summary of windward fuselage center-line heat-transfer coefficient as a function of local deflection angle at a constant value of $x/l = 0.5$. $R_l \approx 15 \times 10^6$.
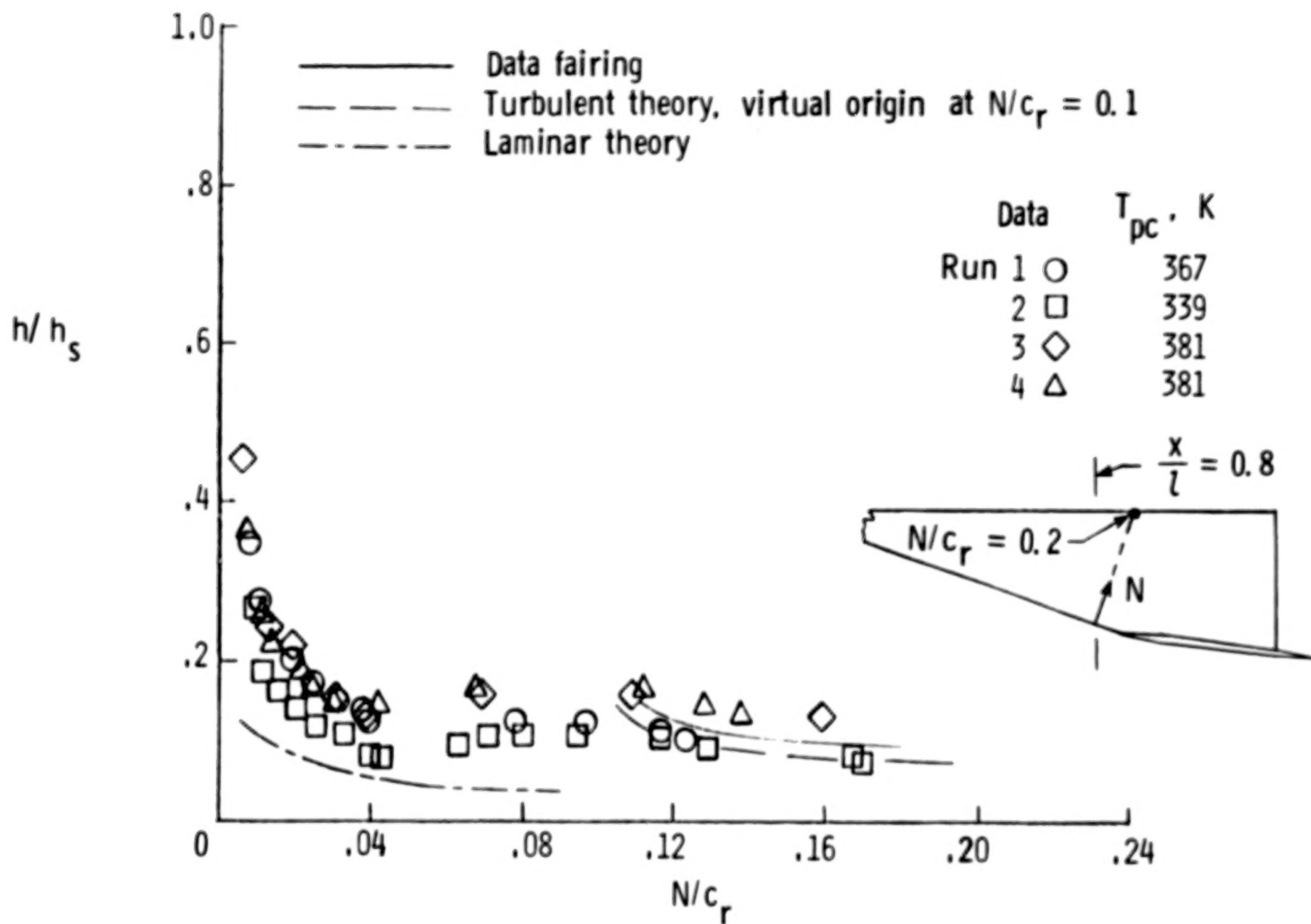
(a) $\alpha = 0.6°$.

Figure 17.- Heat-transfer coefficient as a function of distance normal to wing leading edge. $R_l \approx 15 \times 10^6$.
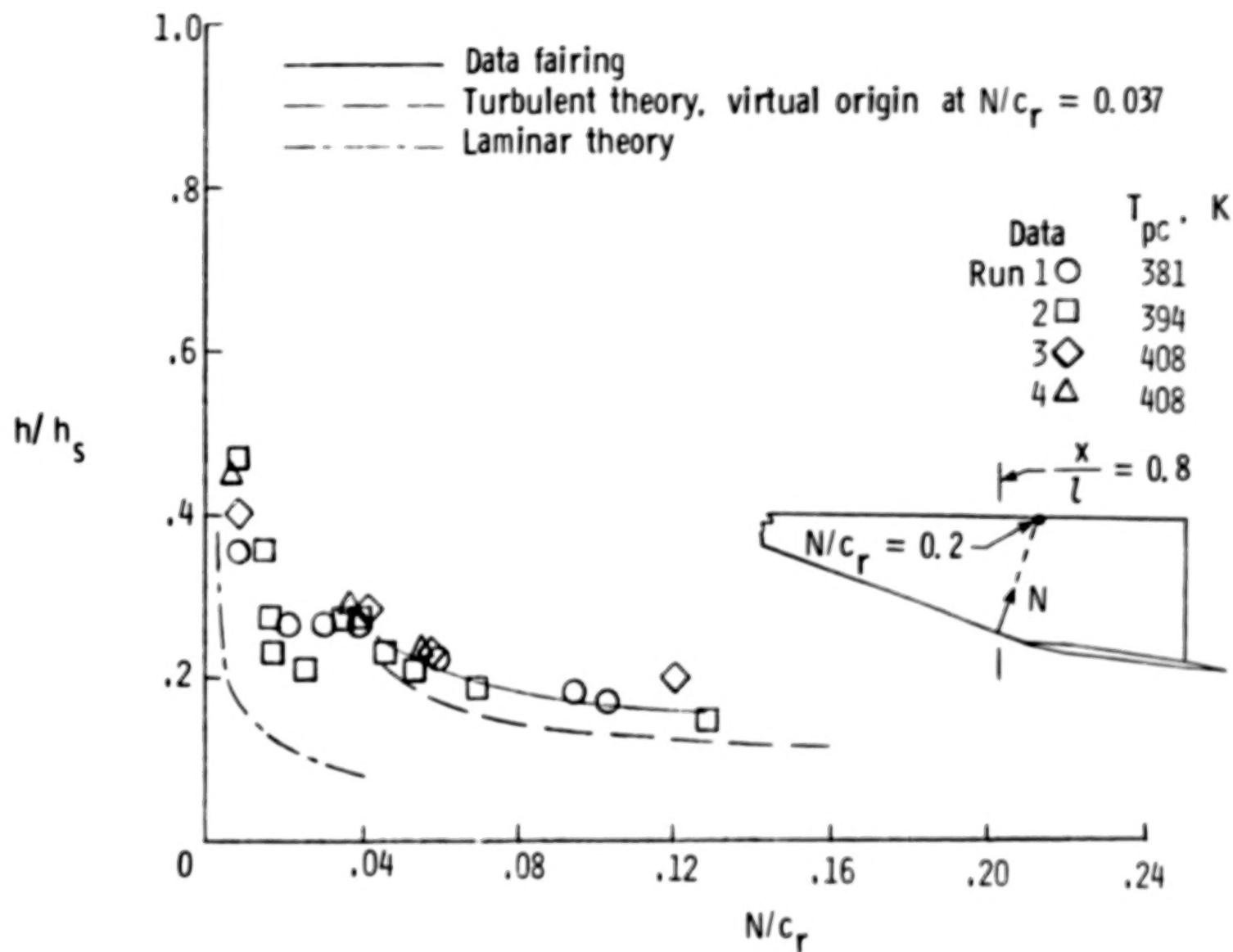
(b) $\alpha = 6.2°$.

Figure 17.- Continued.
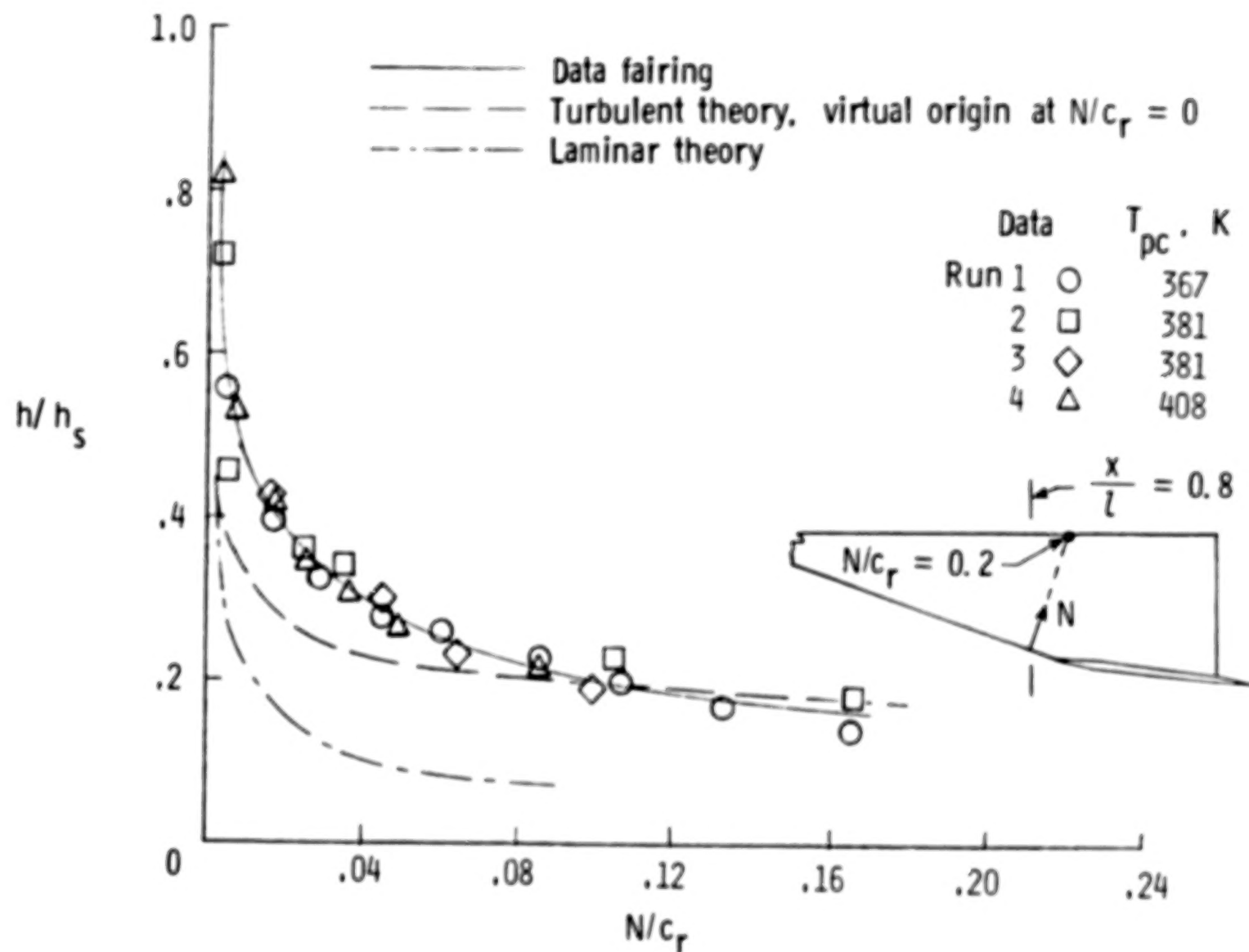
(c)  α ≈ 11.9°.

Figure 17.- Continued.
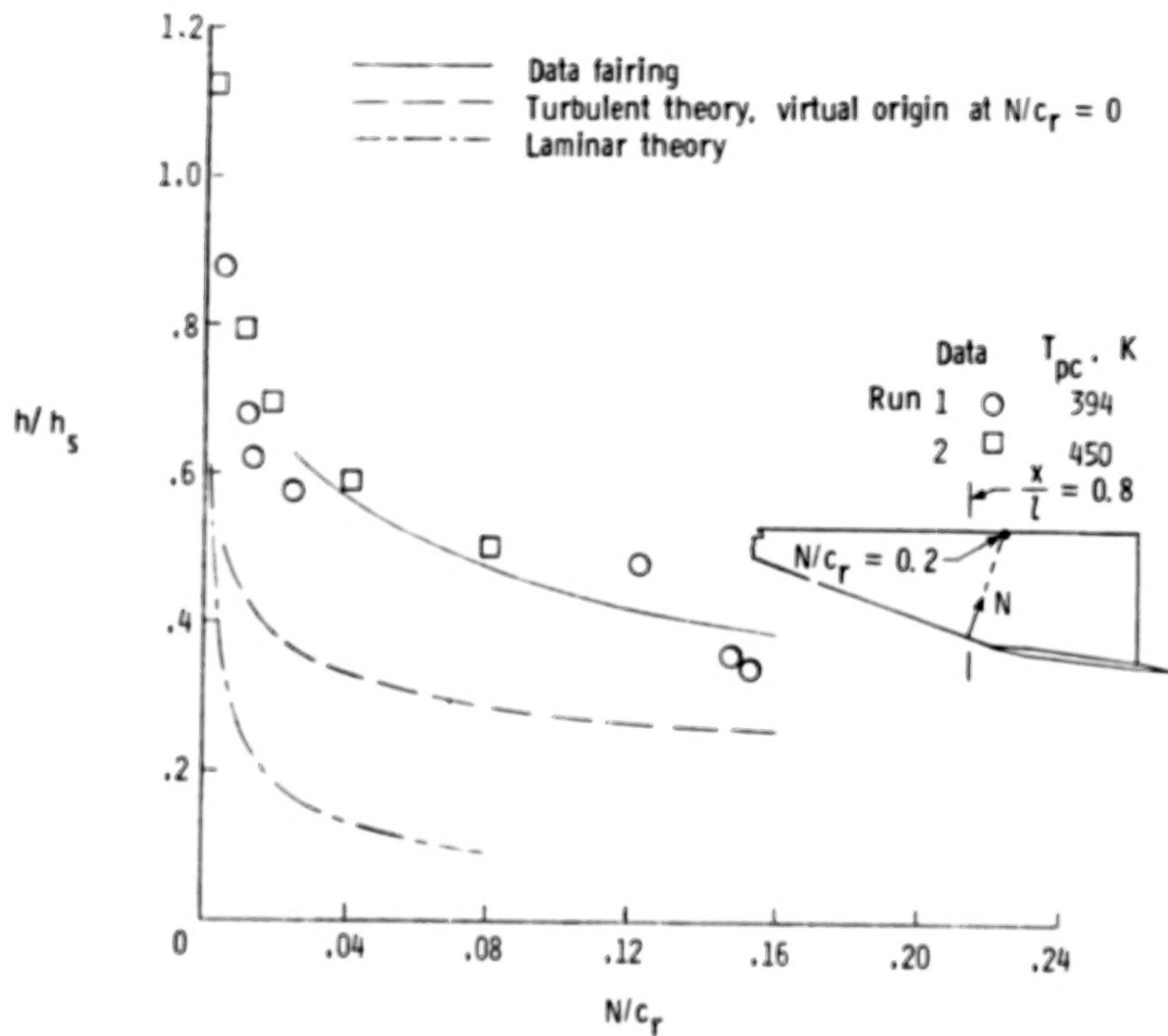
(d) $\alpha = 17.6^{\circ}$.

Figure 17.- Continued.
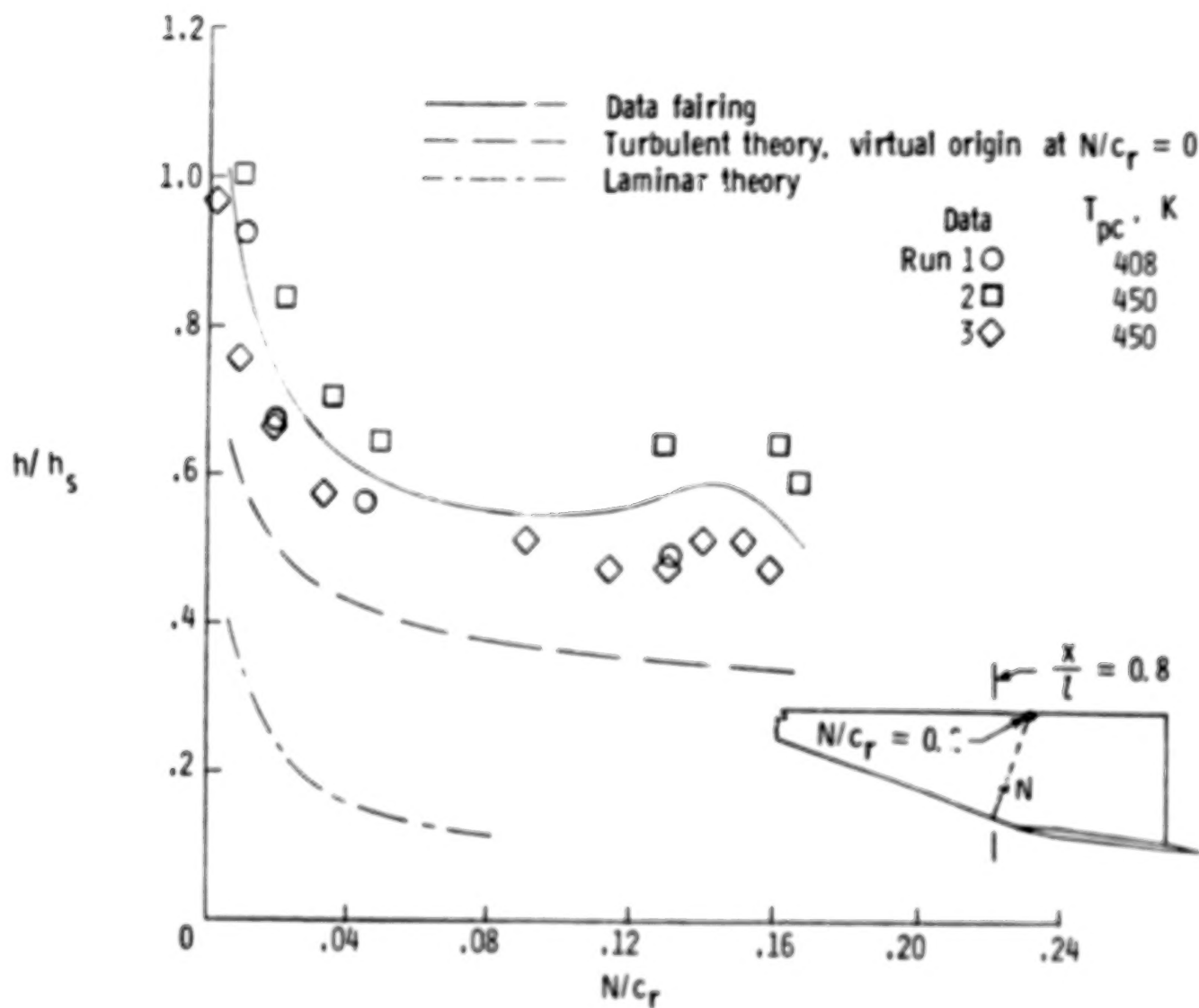
(e)   $\alpha = 24°$.

Figure 17.- Concluded.

Figure 18.- Summary of wing windward surface heat-transfer coefficient as a function of angle of attack at a constant value of $N/c_r = 0.12$. $R_l = 15 \times 10^6$.
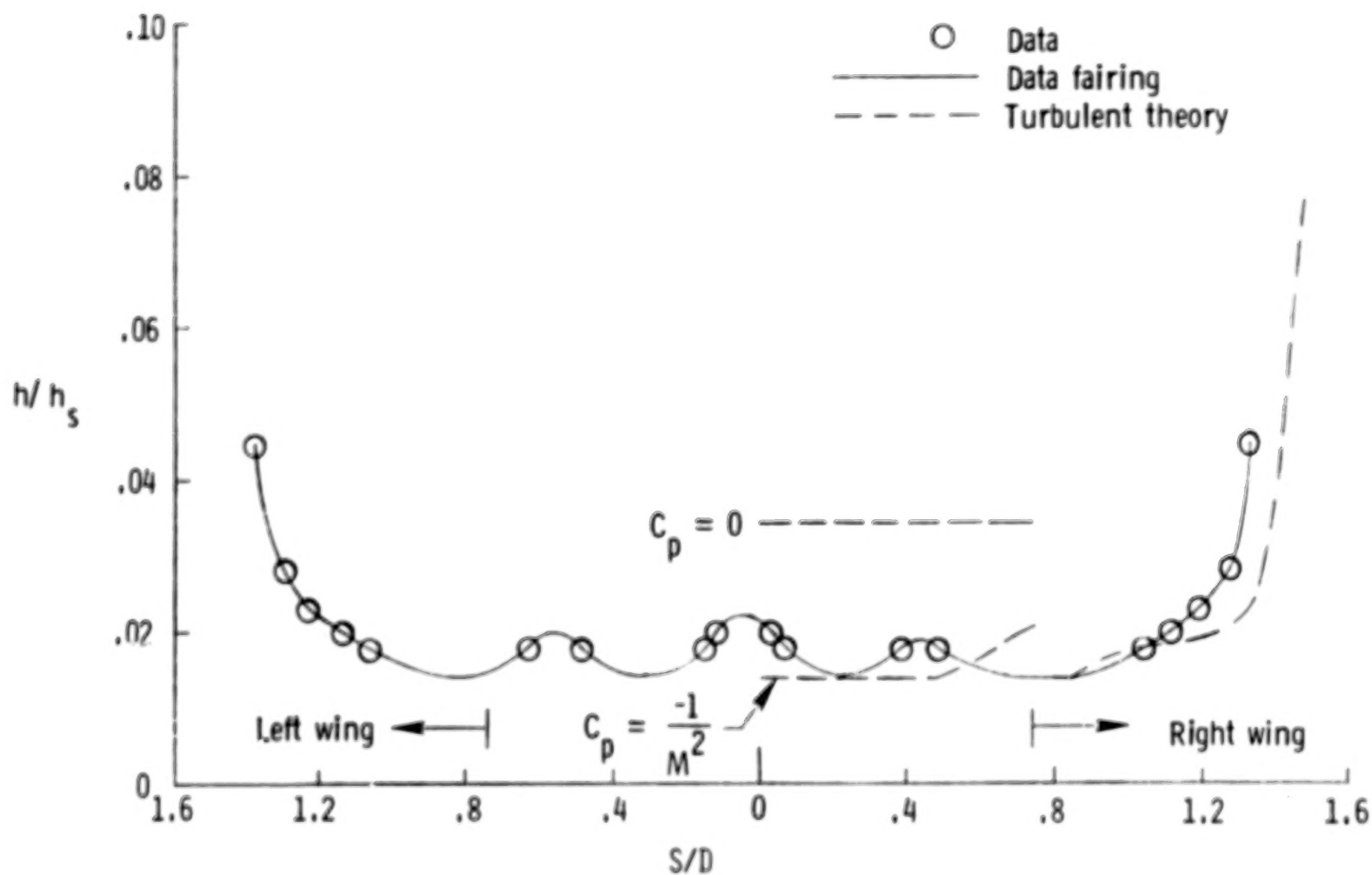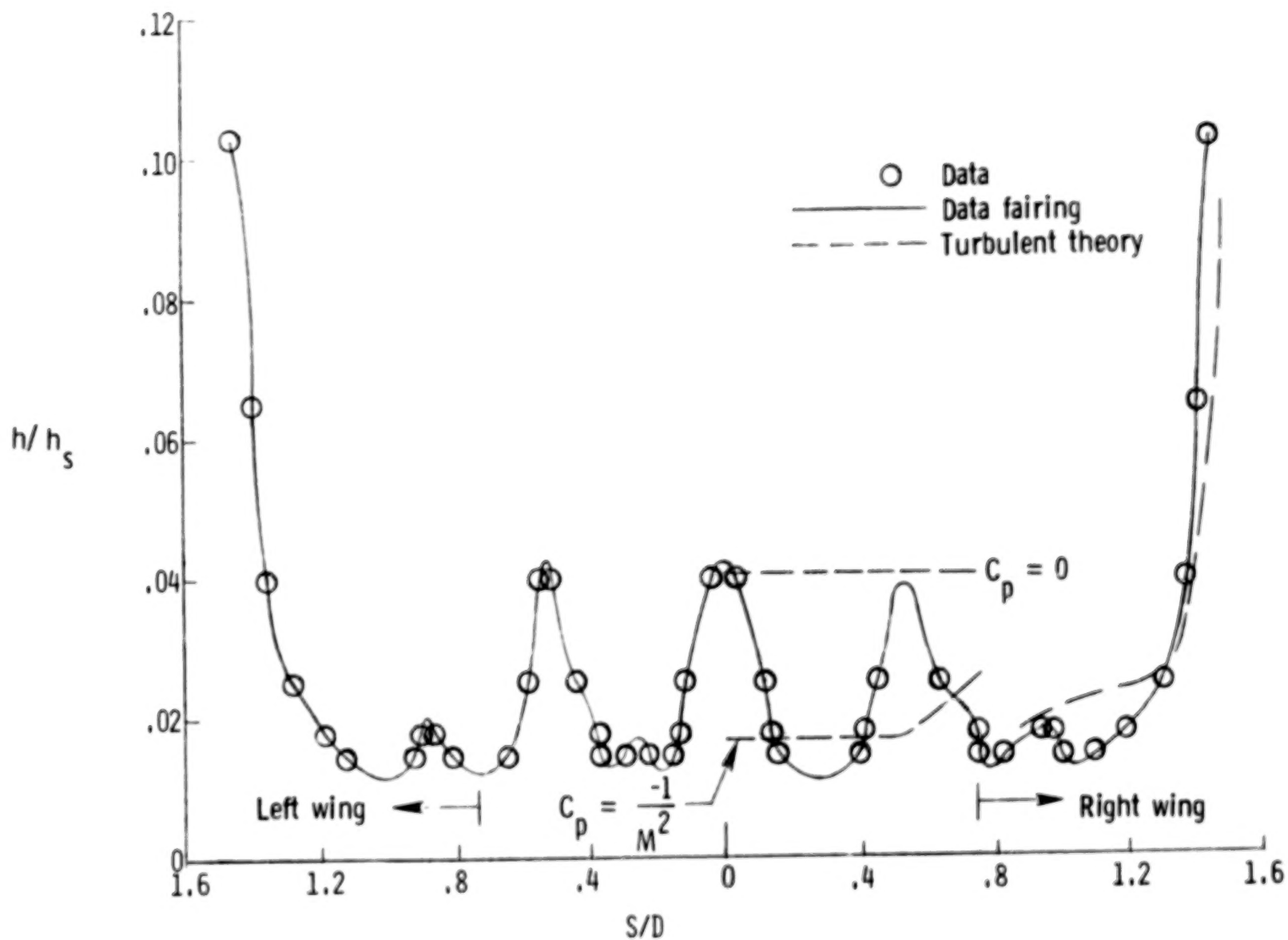
(a) $R_1 = 4.34 \times 10^6$.

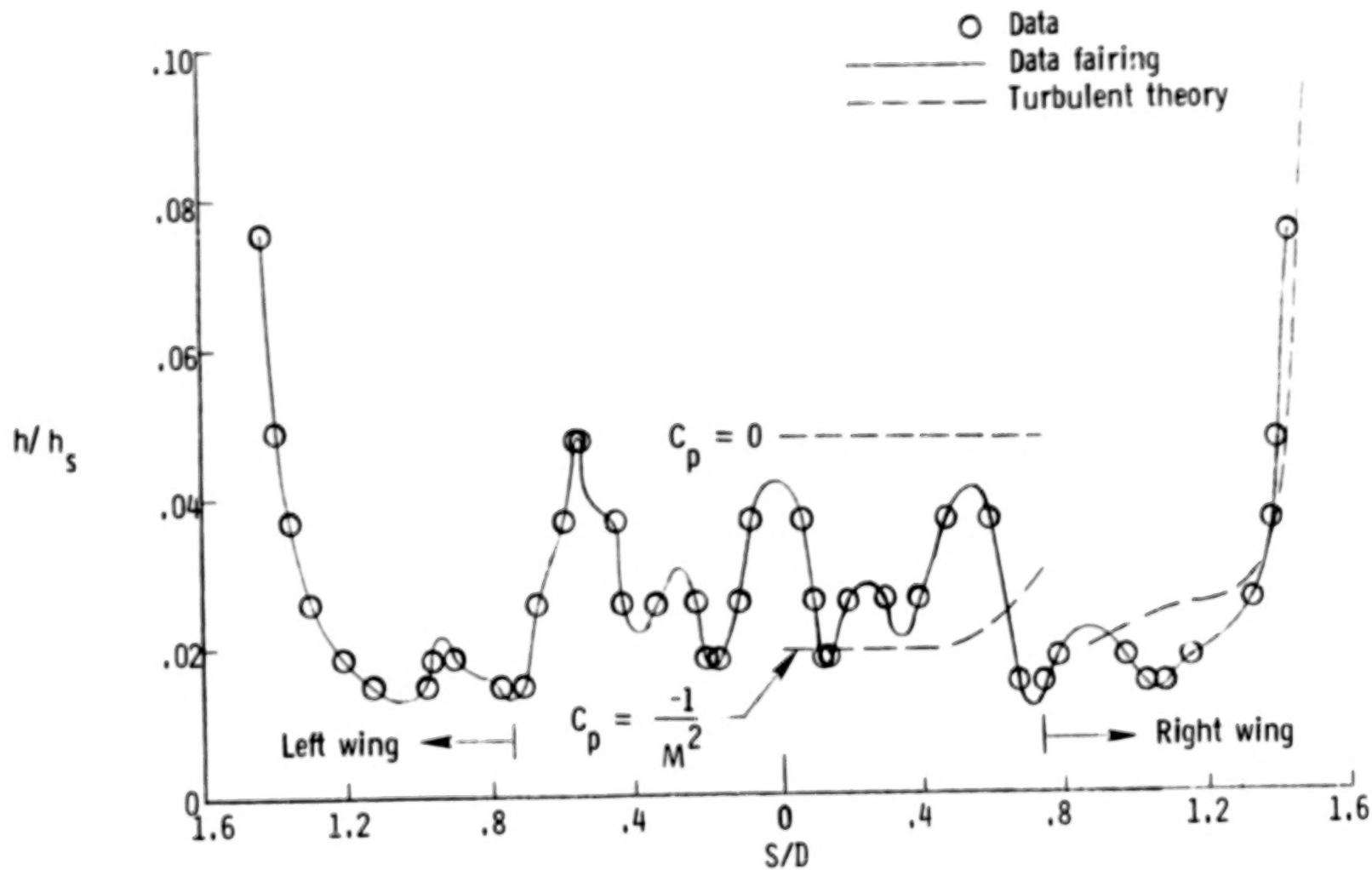Figure 19.- Spanwise heating distribution on model lee side at $\alpha = 11.9°$. $x/l = 0.8$.
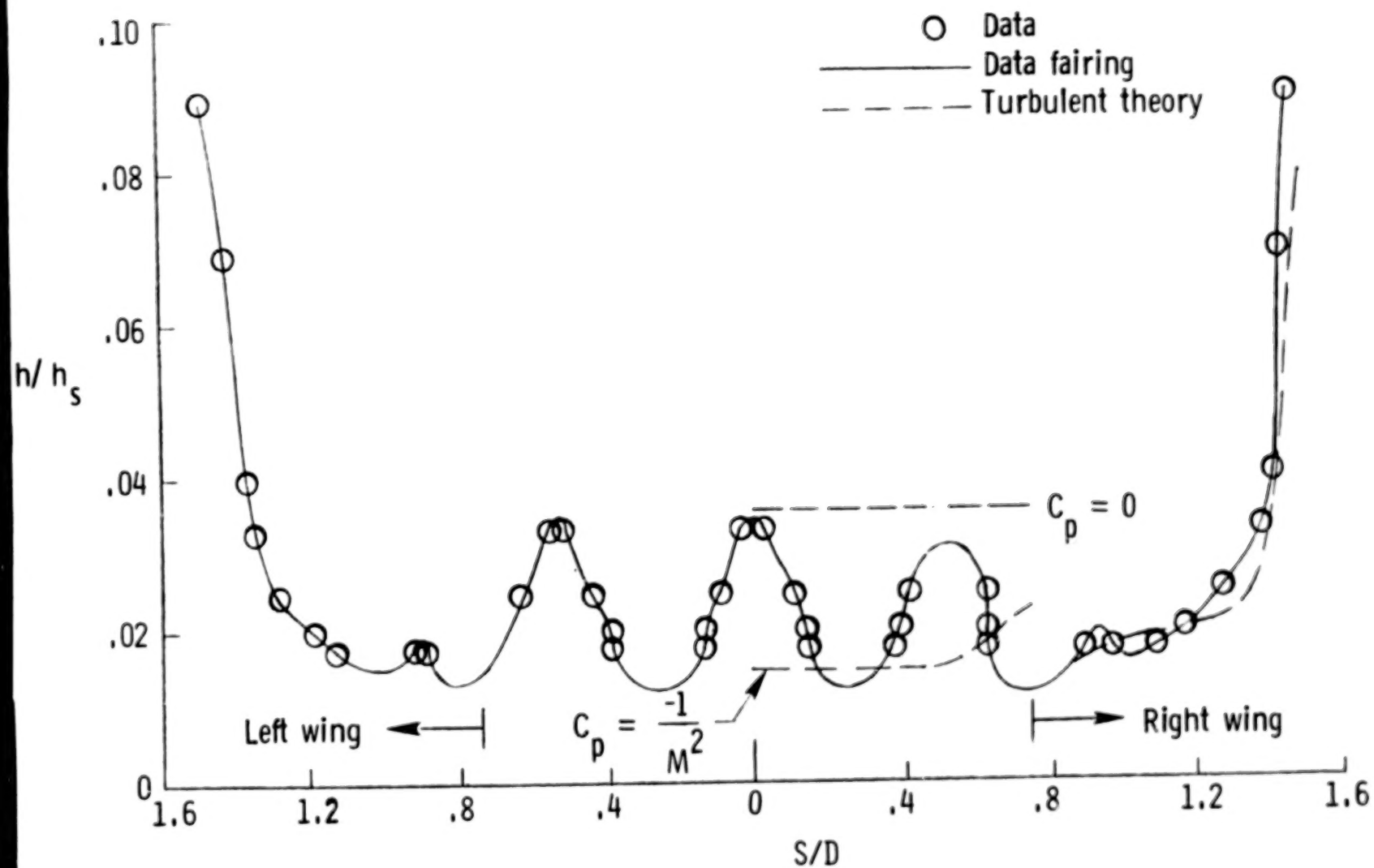
(b) $R_1 = 4.93 \times 10^6$.

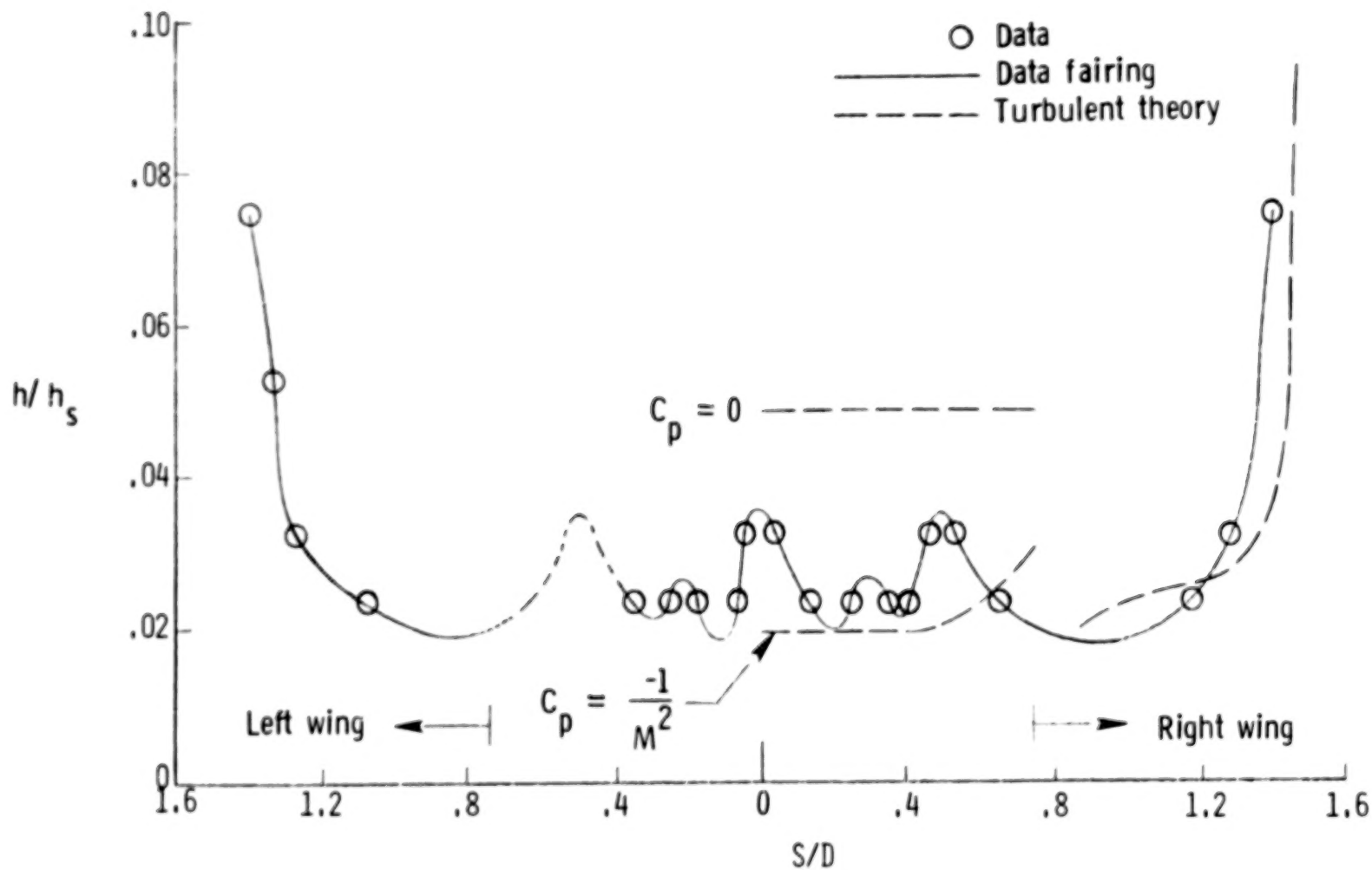Figure 19.- Continued.

(c)  $R_1 = 7.35 \times 10^6$.

Figure 19.- Continued.

(d)  $R_1 = 12.66 \times 10^6$.

Figure 19.- Continued.
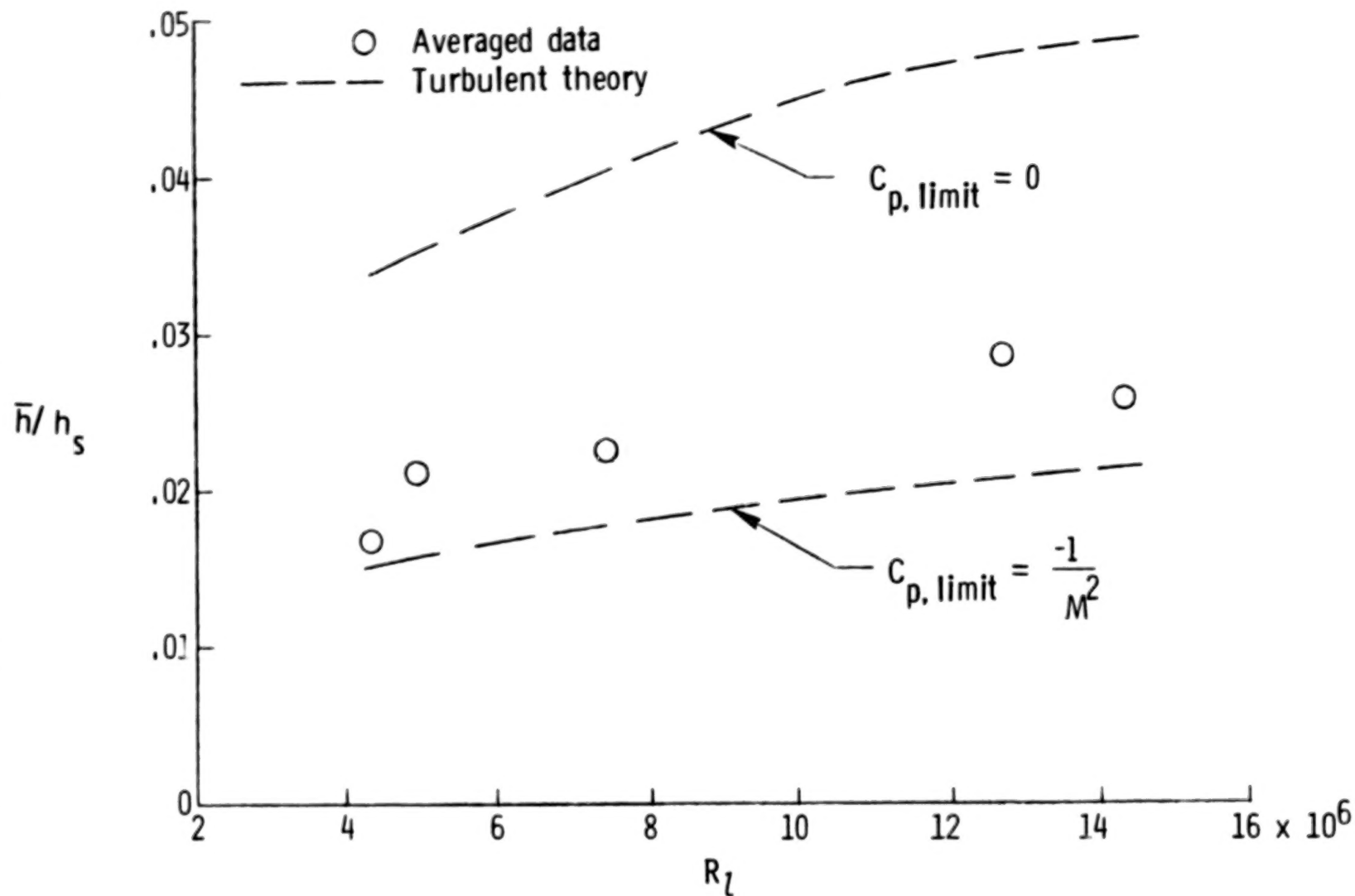
(e)  $R_l = 14.37 \times 10^6$.

Figure 19.- Concluded.

Figure 20.- Summary of model lee-side heating; average heat-transfer coefficient as a function of model length Reynolds number. $\alpha = 11.9°$; $x/l = 0.8$.

73

| 1. Report No. NASA TP-1143 | 2. Government Accession No. | 3. Recipient's Catalog No. |
|---|---|---|

| 4. Title and Subtitle | 5. Report Date |
|---|---|
| CONFIGURATION HEATING FOR A HYPERSONIC RESEARCH AIR-PLANE CONCEPT HAVING A 70° SWEPT DOUBLE-DELTA WING | May 1978 |
| | 6. Performing Organization Code |

| 7. Author(s) | 8. Performing Organization Report No. |
|---|---|
| Pierce L. Lawing | L-11841 |
| 9. Performing Organization Name and Address | 10. Work Unit No. |
| NASA Langley Research Center Hampton, VA 23665 | 505-11-31-02 |
| | 11. Contract or Grant No. |
| 12. Sponsoring Agency Name and Address | 13. Type of Report and Period Covered |
| National Aeronautics and Space Administration Washington, DC 20546 | Technical Paper |
| | 14. Sponsoring Agency Code |

15. Supplementary Notes

16. Abstract

The heating on a candidate hypersonic research airplane configuration has been examined experimentally at Mach 6 by the phase-change-paint technique. The configuration has a double-delta wing with tip fins. Phase-change-paint diagrams give heating data for the model top, side, and bottom, with and without deflected elevons for an angle-of-attack range of 0° to 24°. Nominal Reynolds numbers are on the order of $15 \times 10^6$ with supplementary data at length Reynolds number of $4 \times 10^6$, which moves the model from the predominantly turbulent into the predominantly laminar regime. Also, intermediate Reynolds numbers were investigated on the lee side for one angle of attack.

The approximately 25 phase-change-paint diagrams providing heat-transfer coefficient data are supplemented by limited oil-flow data. The data are compared with theory on the forebody center line and normal to the wing leading edge on the windward side at each angle of attack. The wing and fuselage lee-side data are examined as a function of Reynolds number on a transverse line at 0.8 body length. The data show reasonable agreement with simple theories, and very early transition locations on the wing. Average heating on the lee side is somewhat higher than expected from expanding the flow to a pressure coefficient of $-1/M^2$ (where M denotes Mach number) but much lower than expanding the flow to a pressure coefficient of 0.

| 17. Key Words (Suggested by Author(s)) | 18. Distribution Statement |
|---|---|
| Configuration heating    Transition<br>Hypersonic vehicles    Heat transfer<br>Turbulent heating<br>Research aircraft | Unclassified - Unlimited<br><br>Subject Category 34 |

| 19. Security Classif. (of this report) | 20. Security Classif. (of this page) | 21. No. of Pages | 22. Price* |
|---|---|---|---|
| Unclassified | Unclassified | 73 | $5.25 |